OPTIMIZATION OF PROCESS PARAMETERS, POST PROCESSING TREATMENTS, AND PHASE DIAGRAM FEATURES FOR CONTROLLING THE MICROSTRUCTURE AND PERFORMANCE OF ADDITIVELY MANUFACTURED METALS

A Dissertation

by

RAIYAN ALI SEEDE

Submitted to the Graduate and Professional School of
Texas A&M University
in partial fulfillment of the requirements for the degree of

DOCTOR OF PHILOSOPHY

Chair of Committee, Ibrahim Karaman
Committee Members, Raymundo Arroyave
Alaa Elwany
Ankit Srivastava
Head of Department, Ibrahim Karaman

May 2022

Major Subject: Materials Science and Engineering

ABSTRACT

Additive manufacturing (AM) has gained considerable academic and industrial interest due to its ability to produce parts with complex geometries with the potential for local microstructural control. However, due to the large number of material and process variables associated with AM, optimization of alloying compositions and process parameters is an arduous task. There is a fundamental gap in understanding how changes in process variables and material properties affect additively manufactured parts. An optimization framework to determine process parameter ranges for building porosity-free parts is introduced here and validated for a newly developed ultra-high strength steel alloy. This framework utilizes the computationally inexpensive Eager-Tsai model, calibrated with single track experiments, to predict the melt pool geometry. A geometric criterion for determining maximum allowable hatch spacing is also developed to avoid lack of fusion induced porosity in the as-printed parts. This process optimization framework is then applied to four binary nickel-based alloys, namely, Ni-20at.% Cu, Ni-5at.% Al, Ni-5at.% Zr, and Ni-8.8at.% Zr in order to study the effects of alloying composition and material properties on printability and solidification microstructures in AM. These compositions are selected to represent binary isomorphous, weak solute partitioning, strong solute partitioning, and eutectic alloying conditions respectively. Single track and bulk experiments are conducted to quantify the effects of varying material properties such as solidification temperature ranges, alloy melting temperatures, and other solidification conditions on resultant microstructures across the laser powder bed fusion (L-PBF) parameter space. A second layer is added to the parameter optimization framework to predict microsegregation across the laser power – scan speed parameter space and is validated for each of these alloys to determine how material properties affect printability and microstructure in L-PBF. Finally, the effect of post processing treatments on additively manufactured ultra-high strength

steel are studied to refine and homogenize microstructural features and further improve mechanical properties. This knowledge will be vital in optimizing alloy chemistry, process parameters, and post processing schedules to design alloys specifically for additive manufacturing, as well as to provide a path toward local microstructure control.

CONTRIBUTORS AND FUNDING SOURCES

Contributors

This work was supported by my advisor, Professor Ibrahim Karaman, Professor Raymundo Arroyave of the Materials Science and Engineering Department, and Professor Alaa Elwany of the Industrial and Systems Engineering Department who all supervised and secured resources needed to conduct this work.

Support in operation of the Cameca SXFive Microprobe for wavelength dispersive spectroscopy was provided by Dr. Andrew Mott. Jiahui Ye, Bing Zhang, and David Shoukr contributed to operation of the 3D Systems ProX DMP 200, computational modelling of single-track dimensions, and plotting the printability maps displayed in this paper. Austin Whitt supported the experimental characterization efforts throughout this work. William Trehern contributed to the random forest machine learning model analysis of microsegregation data and feature engineering to develop the empirical microsegregation equation derived in this work. Dr. Sezer Picak contributed to electron backscattered diffraction experiments. Dr. Sean Gibbons and Dr. Philip Flater contributed to experimental planning, Charpy impact testing, and sourcing the raw material used for AF9628 experiments.

Funding Sources

Support for this research came from the Army Research Office (ARO), USA under Contract No. W911NF-18-1-0278 for the work conducted at Texas A&M University. Graduate study in 2019 was supported through the AZZ Incorporated Graduate Fellowship.

TABLE OF CONTENTS

Page

LIST OF FIGURES

LIST OF TABLES

INTRODUCTION*

Laser Powder Bed Fusion

Several additive manufacturing processes have been designed to produce metallic materials. These processes can be categorized based on feedstock and feeding mechanisms. This work focuses on Laser Powder Bed Fusion (L-PBF) processes. Laser powder bed fusion (L-PBF) is an additive manufacturing (AM) process with the ability to manufacture metallic parts with complex geometries that would be challenging or impossible to produce with traditional manufacturing techniques. L-PBF has been used to fabricate a variety of alloy systems originally designed for traditional manufacturing processes such as nickel-based super alloys [1–5], Al-Si-Mg alloys [2,6,7], austenitic steels [2,8], Ti-6Al-4V [2,9–11], as well as many other alloys [12–21].

Powder bed fusion AM is popular due to its ability to produce finely detailed near net-shaped parts with high accuracy. This is due to the small energy source size, fine distribution of powder particles (typically ranging between 10 – 60 μm for L-PBF) used in the process, and thin layering strategy (typically between 20 – 100 μm) [2,22]. During laser powder bed fusion, a thin layer of powder is spread onto a substrate by a roller. This layer is then subjected to laser rastering in a pass-by-pass motion. The roller then deposits a new layer of powder on top of the previous layer,

and the cycle is repeated. L-PBF is typically conducted in an inert environment such as an argon or nitrogen atmosphere.

There are many variable process parameters in L-PBF. Some of these parameters include the following: laser power, scanning speed, hatch spacing, powder layer thickness, scanning strategy (unidirectional, bidirectional, zigzag, island, etc.), hatch angle (the change in rastering angle between each subsequent layer), substrate temperature, and many others. Each of these variables can have significant effects on the microstructural and mechanical properties of as-built parts [2,23–25]. Improper selection or combination of these parameters can lead to an increased amount of porosity or other defects in the build [2,23–25].

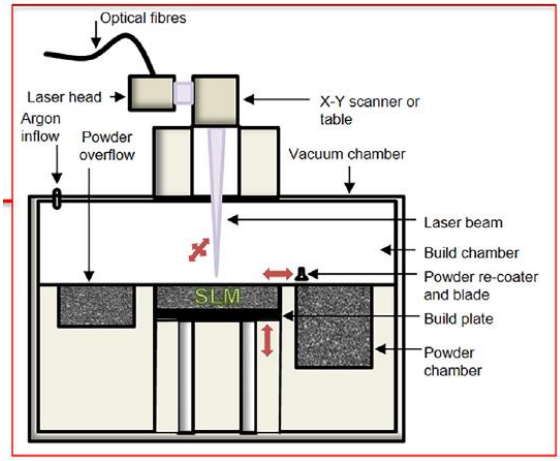

Figure 1. A schematic of the selective laser melting process showing the laser source, powder beds, recoater blade or roller, and build chamber [26].

Defects in AM

The formation of defects in additive manufacturing has significant effects on the mechanical properties of as-built parts. Common defects include porosity, surface roughness, and internal stress. These defects and their formation mechanisms are generalizable to many different alloying systems and AM processes. The formation of porosity in AM can have deleterious consequences

to ductility and fatigue life of as-printed parts [2,25]. Surface roughness can similarly reduce the fatigue life in many alloy systems. High internal stresses can cause parts to warp if subjected to post-processing heat treatments and reduce the ductility of as-printed parts. The following section will discuss porosity formation mechanisms and possible mitigation strategies.

Lack of Fusion

Lack of fusion is a common porosity formation mechanism in all additive manufacturing processes. As the name suggests, lack of fusion is caused by insufficient melting during deposition, creating a void inside the bulk specimen. This is typically due to poor process parameter selection. For L-PBF, proper selection of power, speed, hatch spacing, and layer thickness is required to avoid lack of fusion porosity. High power melts more material and is associated with large melt pools. High scan speed reduces the amount of time the material is exposed to the heat source and is associated with reduction in melt pool size. The morphology of the melt pool depends heavily on the dominant mode of heating. At low power, conduction through the substrate and convection in the melt pool are the dominant modes of heat transfer, and the molten pool will take a semicircular to elliptical shape [2,27,28]. However, at high laser powers melt pool depth will increase exponentially, whereas the width of the melt pool will continue to increase based on conduction mode heating [27,29]. This is because of the effect of vaporization on heat transfer in a process known as keyholing, which will be discussed more in the following section. These changes in melt pool size also effect lack of fusion based porosity. Small melt pool widths require the selection of small hatch spacing values for neighboring tracks to overlap. Melt pools must be deep enough to penetrate the previous layer of material for suitable layer fusion. This means that parameters must be adjusted for different layer thicknesses to avoid lack of fusion.

Several studies attempt to predict melt pool dimensions in various materials to avoid lack of fusion porosity with reasonable success. Mukherjee et al. [30] proposed a dimensionless equation to predict lack of fusion based porosity in parts built using L-PBF. This equation fit reasonably well with literature values for lack of fusion porosity in Ti-6Al-4V. Dimensionless equations in AM are used in an attempt to generalize predictions across material systems. However, some of the thermophysical material properties required to use this equation, such as Marangoni number (this number quantifies the shear stress driving fluid flow in the molten pool) and absorption coefficients for the liquid and solid states of the material, are not readily available for less popular alloys. Other studies have attempted to use conduction based models pulled from welding literature to predict melt pool morphology [2,31]. Although these models do not consider powder on the surface of the substrate or the other modes of heat transfer discussed earlier, they give reasonable predictions of melt pool morphology at low energy densities. Due to the influence of keyhole mode heating at high energy densities, conduction based models are not accurate at high energy densities [2]. Using models to predict lack of fusion based porosity for proper selection of process parameters is currently a hot topic of research [2,10,27,30–32]. Much work is needed to accurately predict melt pool morphology and avoid costly experimentation.

Keyholing and Vaporization

The concept of keyholing is not unique to additive manufacturing, and is well documented in welding literature [33]. This process involves the use of high energy input vaporizing metallic material in the weld pool. The vaporized material then absorbs more energy due to a process called the “Inverse Bremsstrahlung” process [34]. This increase in energy absorbed from the power source then causes the vaporization of more material in a cyclical process. Since power source distributions in laser beam welding and additive manufacturing can typically be represented by a

Gaussian distribution profile, implying the intensity of the power source is concentrated at the center, this keyholing phenomenon results in a deep and narrow melt pool. These keyholing melt pools are unstable and can collapse, entrapping inert gas and creating pores within a build [27,35,36]. An image of a keyhole melt pool and its resultant porosity is displayed in Figure 2b. Keyholing induced porosity is typically larger than 50 µm, and can have globular shapes or sharp edges.

Keyholing typically occurs at high energy densities. This means that keyholing occurs at combinations of high laser powers and low scan speeds. Matin et al. [37] showed that keyhole induced porosity can occur during laser turning points during L-PBF processing of Ti-6Al-4V components. This is due to the reduction in scanning velocity while laser power remains constant as the laser approaches a turning point, resulting in increased energy input and keyhole mode porosity formation [37]. They reported that a linear reduction in laser power during these turning point approaches successfully mitigates the formation of these pores [37].

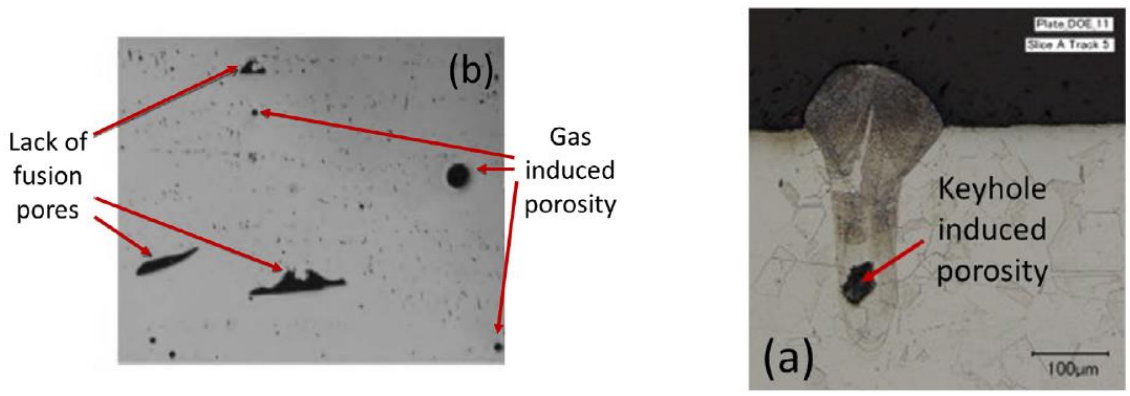

(a) (b)

Figure 2. Optical microscope images of different types of pores characteristic to additive manufacturing [2]: a) Lack of fusion and gas entrapped porosity in AM part [38]. b) Keyholing induced porosity in a single track produced by laser powder bed fusion [27].

Balling

High variance in melt pool width has been observed to occur at high scan speeds in single-track scans for L-PBF manufacturing [2,39]. Single-tracks printed at high scan speeds can form as molten droplets instead of a continuous molten pool. As scanning speed increases, the melt pool elongates and becomes unstable. In order to maintain uniform capillary pressure, the molten pool to breaks up into small droplets [2]. This melt pool instability is known as Plateau-Rayleigh capillary instability and is due to the tendency of liquids to minimize their surface area. The molten droplet effect in AM is known as balling. In order to mitigate this effect, the maximum allowable molten pool length can be defined by the ratio $L/D \geq \pi$, where L is melt pool length and D is melt pool depth [40]. An SEM micrograph showing the effect of scan speed on track morphology is displayed in Figure 3. The balling phenomenon is clearly observable in tracks with scan speed above 300 mm/s. This phenomenon can result in porosity and surface roughness due to the uneven melt pool structure. Limiting scan speed and implementing high enough laser power to maintain the length to depth melt pool dimension ratio can mitigate the balling effect.

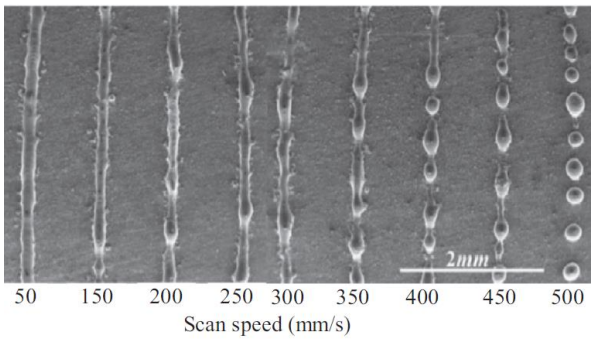

Figure 3. An SEM micrograph showing the effect of scan speed on track morphology. The balling phenomenon is clearly observable in tracks with scan speed above 300 mm/s [2,39].

Parameter Optimization for Porosity

Optimization of process parameters to fabricate porosity-free samples is typically achieved via a broad sweep of experiments at many parameter sets [41–44], which is an arduous and time consuming procedure. Several model-based approaches to predicting melt pool dimensions have been proposed in order to reduce the experimental requirements for determining suitable process parameters [10,31,32,45,46]. These range from computationally intensive and lengthy [45,46] to simple and fast analytical models [31,32]. However, literature on bridging the gap between melt pool dimension predictions and building porosity-free parts is sparse. Some studies have suggested using optimal melt pool dimension ratios to determine variables such as hatch spacing [32,47]. This approach still requires laborious experimentation to determine these optimal ratios and does not account for porosity formation mechanisms such as balling or keyholing. Establishing a framework to implement model-based approaches to building porosity-free parts is therefore essential.

Abrahams recently discovered a relatively inexpensive, low alloy, ultra-high strength martensitic steel called AF9628 [48]. It takes advantage of the formation of an ε-carbide phase resulting in the observed ultra-high strength levels. The material displays tensile strengths in excess of 1.5 GPa with around 10% tensile elongation [49,50]. With proper microstructural refinement, the strength level can exceed 2.0 GPa in AF9628 [51]. Due to the ease of fabrication and low cost of constituent elements, AF9628 has attracted significant industrial interest in the last few years. There is also some interest in producing geometrically complex high strength steel parts. However, currently there is no known work describing process-structure-property relationships for AF9628 in the context of additive manufacturing. This warrants a systematic study focusing on

the effects of additive manufacturing process parameters on the microstructural evolution and resulting mechanical properties of this new martensitic steel.

The present work utilizes the simple analytical Eagar-Tsai [52] model for predicting melt pool geometry, combined with single track experiments, and a geometrical hatch spacing selection criterion developed in this work to investigate the range of process parameters for AF9628, which consistently lead to full densification of SLM parts. The microstructure and mechanical properties are then characterized to determine the overall feasibility of SLM processing for bulk AF9628 samples, and to investigate the role of process parameters in the resulting mechanical properties.

Microstructural Challenges

Alloy Composition and L-PBF Process Parameters

Alloy systems historically used in L-PBF vary widely in both the ranges of manufacturing process parameters required to build fully dense parts as well as their microstructural responses to L-PBF processing. Nickel-based superalloys such as Inconel 718®, for example, can display cellular-dendritic microsegregation that results from the high cooling rates during solidification associated with L-PBF [2,5,53,54]. On the other hand, Ti-6Al-4V does not typically display microsegregation structures in the as-fabricated condition [55]. Differences in microsegregation between alloys have typically been attributed to the solidification ranges and partition coefficients of the alloys being processed [2], though these effects have not been sufficiently quantified for AM. Microsegregation can have an impact on the mechanical properties and performance of fabricated parts. In nickel-based superalloys, microsegregation of niobium can lead to the growth of δ and laves phases which are detrimental to the performance of these alloys [1,2,5,53]. Mitigation of these issues has generally consisted of identifying optimized process parameters that circumvent the formation of microsegregation structures [56,57], or implementing post processing

heat treatments to resolve them [1,2,5,53,58,59]. However, post processing treatments can result in coarse grain structures, and may not be able to resolve the formation of detrimental phases that are stable at high temperatures such as δ phase and MC carbides in nickel-based superalloys [5,53]. Therefore, the ideal strategies for mitigating the formation of such detrimental phases are preventing microsegregation by using optimized process parameters or by tailoring alloy composition.

In addition to differences between alloy systems, the selection of process parameters can have a significant impact on microstructural development [2,56,60]. Using a laser rapid directional solidification model that they developed, Liang et al. [60] predicted an increase in the microsegregation of tungsten at low scan speeds and high laser powers in the single crystal nickel-based super alloy SRR99. Karayagiz et al. [56] developed a framework coupling a finite element thermal model with a non-equilibrium phase field model in order to accurately predict microsegregation in single track scans of an L-PBF fabricated Ni-Nb alloy. They found that cellular-dendritic growth structures varied in both size and solute segregation depending on the linear energy density used for each laser scan [56]. Cellular structures with Nb-rich boundaries were observed at high energy densities, whereas planar growth was shown to dominate the microstructures of low energy density Ni-Nb single tracks [56]. However, these predictions target single laser scans due to the complex thermal histories associated with the layer-by-layer development of L-PBF which can be difficult and computationally expensive to model. Additionally, current literature has focused on predicting microstructural evolution as a function of interface growth velocities (R) and thermal gradients (G), which do not easily translate to usable input parameters for the L-PBF process such as laser power and scan speed [56,61]. The

establishment of a simple approach to evaluate bulk solidification microstructures across the L-PBF parameter space is therefore highly valuable.

There is substantial interest in designing new alloys to address the complex challenges posed by additive manufacturing [62]. To develop new alloys, an understanding of how compositional and material property changes affect additively manufactured parts is critical. This work utilizes the previously established parameter optimization framework [21] combined with experimental single track microsegregation data in order to develop processing maps for both densification and microstructure in L-PBF. Processing maps are then developed for four binary nickel-based alloys, namely, Ni-20at.% Cu, Ni-5at.% Al, Ni-5at.% Zr, and Ni-8.8at.% Zr in order to represent binary isomorphous, weak solute partitioning, strong solute partitioning, and eutectic alloying conditions, respectively. Quantitative wavelength dispersive spectroscopy (WDS) observations of both single track and bulk experiments are used to validate the processing maps as well as to elucidate the effects of material properties and alloying conditions on printability and microstructure in L-PBF. An empirical model is developed by exploiting the dataset generated in this study using materials informatics to accurately predict dendritic microsegregation structures as a function of L-PBF process parameters and easily accessible material property inputs.

Post Processing Heat Treatments for AF9628

Several recent studies have attempted AM of martensitic steels using LPBF. Dilip *et al.* [63] fabricated the martensitic HY100 steel using LPBF, and achieved near-fully dense (99.7% density) parts. However, heterogeneous microstructures with the mixture of tempered and untempered martensite bands were observed in the as-printed parts [63]. These bands were attributed to the thermal cycling effects of layer by layer deposition associated with the LPBF process [63]. As-printed HY100 parts displayed significant tensile anisotropy, showing greater ultimate tensile

strength (UTS) and lower ductility in samples loaded perpendicular to the building direction (BD) compared to those loaded parallel to the BD [63]. Along both of the directions tested, as-printed specimens had greater yield strength (YS) and UTSs but significantly lower ductility in comparison to their wrought counterparts [63]. Jelis *et al.* [64] investigated anisotropy in the microstructure and mechanical properties of LPBF fabricated AISI 4340 steel. As-printed AISI 4340 displayed tensile anisotropy and microstructural tempering bands similar to what was found in HY100 [63,64]. These specimens were found to have lower YSs and UTSs but greater ductility than as-wrought AISI 4340 [64]. Directional dependence of mechanical properties and microstructural inhomogeneity observed in LPBF low alloy steel parts can be detrimental to part performance. Understanding how to mitigate these effects while also targeting traditionally processed material property standards will enhance the feasibility of using these materials and parts in industrial applications.

In order to address the aforementioned issues, both of the studies also performed post-processing heat treatments on HY100 [63] and AISI 4340 [64]. Dilip *et al.* [63] tested several heat treatment schedules on as-fabricated specimens: three direct temper treatments at different temperatures (620 °C, 650 °C, or 670 °C for 2 hours followed by furnace cooling), and three quench and temper treatments with varying tempering temperatures (900 °C for 1 hour followed by water quenching, then tempering at 620 °C, 650 °C, or 670 °C for 2 hours followed by furnace cooling). They were able to replicate the mechanical properties of traditionally processed HY100 as well as homogenize the microstructure of the LPBF specimens with a water quench and temper treatment at 650 °C [63]. With a heat treatment schedule of: stress relief, normalization, austenitization and oil quenching, and double tempering, as-printed AISI 4340 was found to have superior mechanical properties compared to the wrought material [64]. These results indicate that

post processing heat treatments are relatively successful at improving the mechanical properties of LPBF low alloy steels.

Wrought AF9628 exhibits tensile strengths above 1.5 GPa with ~10% elongation [49,50]. Vaughan *et al*. [51] reported that by controlling prior austenite and martensite grain sizes via equal channel angular processing (ECAP), the tensile strength of AF9628 can be controlled and can even exceed 2.0 GPa with a strain to failure levels over 6%. They also reported a quench and temper heat treatment schedule for as-forged AF9628 that resulted in 1.77 GPa UTS and 11.5% elongation [51]. AF9628 is relatively easy and less expensive to fabricate compared to its alloyed steel competitors. These properties have rendered this new steel an attractive alternative for industrial applications. In the interest of producing geometrically complex high strength steel parts, Seede *et al*. [21] explored the potential for AF9628 to be fabricated via LPBF. They reported a range of

parameter sets that resulted in fully dense (> 99% density) parts. Melt pool structures with tempered and untempered martensitic regions were observed in the as-fabricated specimens. Cellular solute segregation structures were observed in both the powder and as-printed specimens, however, it is unknown whether these impacted the mechanical properties of the material [21]. Up to 1.4 GPa UTS with 10% elongation was reported for LPBF AF9628 specimens, and tensile anisotropy was observed [21]. It is therefore possible that the melt pool morphology and chemical segregation found in as-printed AF9628 result in the observed differences in mechanical properties (i.e. lower UTS) compared to the as-forged and heat-treated ingot metallurgy materials. Additionally, no post processing heat treatments and their effects on the mechanical properties have been reported to date for the LPBF AF9628 materials.

To assess the differences in mechanical properties between traditionally processed AF9628 compared to the additively manufactured material and pinpoint the potential reasons, the present

work characterizes the effects of post processing heat treatments on the microstructure and mechanical properties of LPBF AF9628 martensitic steel. This work also presents the impact toughness of additively manufactured AF9628 for the first time, which is an important property for practical applications, and demonstrates the effects of subsequent heat treatments on the toughness.

PROPOSED PARAMETER OPTIMIZATION FRAMEWORK*

Porosity Optimization Framework for AF9628 Ultra-High Strength Steel

Analytical Model to Predict Melt Pool Dimensions

To determine the printability region of AF9628, i.e. the region in the laser power-scan speed parameter space where printing fully dense parts is possible, a broad sweep of the parameter space must be performed, either experimentally or numerically. For this purpose, the low fidelity but simple and computationally inexpensive Eagar-Tsai (E-T) analytical model is used to predict melt pool dimensions. Prediction of melt pool dimensions is the first step in the SLM parameter optimization framework because melt pool size either dictates or is a signature for parts' susceptibility to processing-induced porosity such as keyhole porosity or lack of fusion porosity [2]. The goal of selecting a simple, but fast and reasonably predictive, model to predict melt pool dimensions, instead of using a high fidelity, sophisticated finite element analysis that captures the majority of the governing physics, is to eventually develop a simple process parameter optimization framework that is easily implementable by additive manufacturing practitioners.

The E-T model describes the impact of welding process parameters on the geometry and temperature distribution of weld melt pools [52]. The model represents the welding process as a traveling heat source with a Gaussian profile over a semi-infinite flat plate and then calculates the temperature distribution across the plate [65]. This model has been reported in the literature to be a good representation of the melt pool for the SLM process [35,65,66]. To estimate the temperature distribution, and hence the melt pool dimensions (width and depth), the E-T model takes two

categories of inputs into consideration: heat-source parameters (i.e. laser power ‘P’, scan speed ‘v’, and a Gaussian-distributed laser beam diameter ‘d’ which corresponds to four standard deviations of the Gaussian profile of the beam) and material properties taken as constant (i.e. thermal conductivity ‘k’, specific heat capacity ‘C_p’, density ‘ρ’, melting temperature ‘T_m’, and absorptivity ‘A’). The E-T model is limited by the existence of two sources of uncertainty; parameter uncertainty in the material properties, especially for newly developed materials like AF9628, and structural uncertainty also known as model inadequacy, model bias, or model discrepancy. Structural uncertainty comes from the simplifying assumptions in the model, i.e. the temperature-independent material properties, the neglect of latent heat evolution during melting and/or boiling, and the semi-infinite plate assumptions [67]. These two types of uncertainty can drastically affect the accuracy of melt pool predictions.

To overcome the uncertainty problem, a statistical calibration methodology is used here to construct a surrogate statistical model that accounts for these sources of uncertainty. This methodology consists of two stages: the first is constructing the surrogate model for the E-T model using Gaussian process regression, and the second is combining this model with experimental single-track measurements to perform statistical calibration of the unknown or inaccurate parameters. Model inadequacy in describing the physical behavior of the experimentally characterized melt pools is accounted for using a discrepancy function so that predictions from the calibrated model agree with the experimental measurements. The methodology implemented here is based on the Kennedy and O’Hagan [68] framework for the calibration of computer models which has been successfully applied to the calibration of a finite element thermal model of an SLM melt pool [69,70].

Single Track Sampling

To initialize the model calibration process and eventually accurately predict melt pool dimensions in the laser power 'P' and scan speed 'v' processing space, single-track experiments were designed based on the initial predictions of the E-T model, and the available SLM additive manufacturing system specifications (P_{min}, P_{max} = {29, 260 W} and v_{min}, v_{max} = {50, 2500 mm/s}). P_{max} and v_{max} were taken as the available machine limit, and v_{min} was selected as 50 mm/s in order not to have prohibitively slow printing speeds. P_{min} was selected as the minimum amount of power required to achieve a melt pool depth equal to one layer thickness of material at v_{min}.

The initial material property inputs for the E-T model were selected as follows: thermal conductivity 'k' and specific heat capacity 'C_p' were approximated for AF9628 using the properties of HY-100 steel which is another type of low alloy martensitic steel. These properties were selected at melting temperature in the solid state as an approximate reference point. HY-100 steel has, at melting, a thermal conductivity of 35.73 (W/m*K) and specific heat capacity of 705 (J/kg*K) [71]. The absorptivity of the substrate with a layer of AF9628 powder was approximated using reported experimental measurements of 316L steel powder absorptivity measured with a 1 μm wavelength laser and a powder layer thickness of 100 μm [72]. The value of absorptivity used is 68% [72] which should not differ significantly from one steel type to another.

Figure 4a displays the initial printability criteria which are based on predicted melt pool dimensions using the uncalibrated E-T model, and the process parameter sampling distribution for single-track experiments. These criteria were chosen based on literature-defined optimal melt pool dimension relationships: $D/t = 1$ and $D/t = 1.5$ were chosen as the lack of fusion and optimal track specifications [32,73], respectively, where D is the depth of the melt pool and t is the powder layer thickness (37 μm). The first criterion is selected so that the laser beam melts, at minimum, a

material layer as thick as the powder layer to guarantee no lack of fusion between two successive printed layers. Roehling *et al.* [74] reported that keyholing occurs at an aspect ratio of $D/W > 1.5$, where W is the melt pool width. However, this aspect ratio was too small to appear in the selected processing space for the uncalibrated E-T model. Therefore, the keyholing condition $D/W = 2.2$ was plotted as a reference.

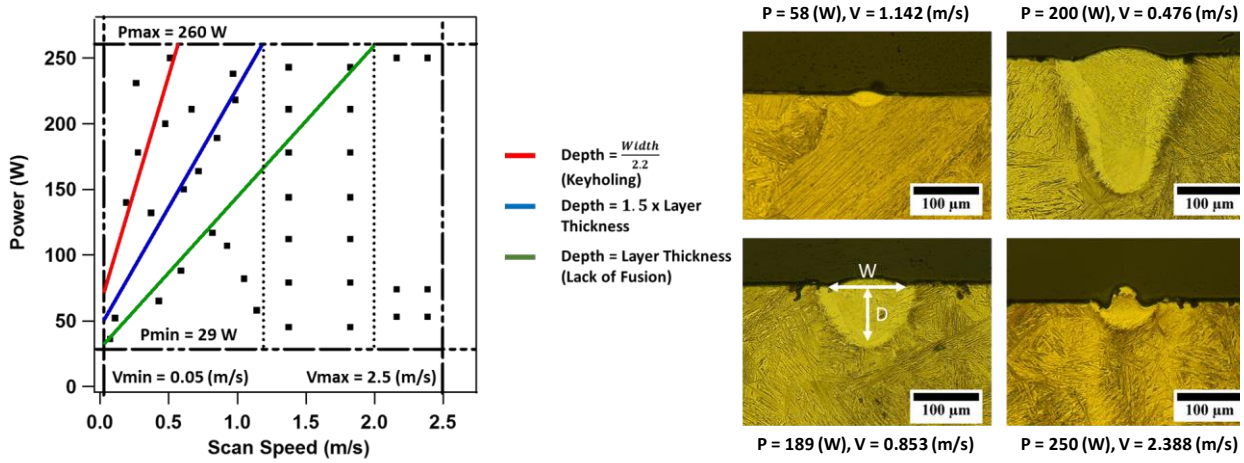

(a) (b)

Figure 4. (a) A plot of the selective laser melting parameter space, for our commercial AM system, with the predictions of the uncalibrated E-T model and the selected single-track sampling points for the experiments. b) Selected AF9628 single-track cross-sectional images demonstrating different types of melt pool characteristics that can be considered as signatures for different defect structures. Top Left: melt pool that will lead to lack of fusion, Top Right: melt pool that is likely to lead to keyholing porosity, Bottom Left: an ideal melt pool that may result in porosity-free parts with white arrows signifying width (W) and depth (D) measurements, Bottom Right: melt pool showing balling.

Three regions were chosen for separate sampling strategies for the single-track experiments in the predicted processing space (separated by the dashed lines in Figure 4a. The first region was selected based on the laser scan speeds that contained v_{min} = 50 mm/s and the calculated scan speed at P_{max} (v = 1145 mm/s, shown by vertical dashed line) to satisfy $D/t \geq 1.5$. This region is expected to contain the majority of the final optimal printabilty region (provided that the E-T model predictions are reasonably accurate). The second region was limited to scan speeds between v = 1145 mm/s and v = 2050 mm/s, the later of which is the speed at which $D/t \geq 1.0$ at P_{max}. The third region contained the rest of the parameter space (v = {2050, 2500 mm/s}), which is unlikely to result in porosity-free prints, but included to validate and better calibrate the model. Forty single tracks were sampled over the entire parameter space: 20 in the first region, 14 in the second, and 6 in the third. More single tracks could be selected for sampling but the total was limited to 40 to minimize the time to characterize all the tracks. Latin hypercube sampling was implemented in the first region of the parameter space in order to maximize the representation of this region [75]. Grid-based parametric sampling was selected for the second and third regions. Examples of a few selected single-track cases are presented in Figure 4b.

Statistical Calibration of the Model

The first stage of the Kennedy and O'Hagan framework for the calibration of computer simulation models is to construct a multivariate Gaussian process surrogate model to the E-T model that is computationally less expensive than the E-T model. To develop this surrogate model, 500 samples were generated from the E-T model according to a Latin hypercube sampling strategy. In this strategy, the inputs are split into three groups based on their measurability: control parameters, calibration parameters, and fixed parameters. Control parameters, i.e. laser power 'P' and scanning speed 'v', are varied according to the SLM system specifications and minimum P

and v values selected (P_{min}, P_{max} = {29, 260 W} and v_{min}, v_{max} = {50, 2500 mm/s}). Unobservable calibration parameters, i.e. thermal conductivity 'k', specific heat capacity 'C_p' and absorptivity 'A', are varied as follows: k_{min}, k_{max} = {20, 120 W/m*K}, $C_{p,min}$, $C_{p,max}$ = {450, 880 J/kg*K}, and A_{min}, A_{max} = {0, 100%}. Since the E-T model assumes conduction mode heat transfer and does not take melt pool convection into account, the optimal effective thermal conductivity value for the E-T model is inflated compared to the initial value. For this reason, a large upper bound (120 W/m*K, in order to accommodate the convective heat transfer) and a lower bound (20 W/m*K) close to the initial value from the literature [71] were selected for calibration purposes. The range for specific heat capacity was selected based on a lower bound representing the specific heat capacity at melting temperature for the solid material (approximated from HY-100), and an upper bound representing an effective specific heat capacity of melting. The effective C_p of melting is simply calculated as the slope of a linear fit to enthalpy vs temperature bounded between room temperature in the solid state and melting temperature in the liquid. Beam size 'd', density 'ρ', and melting temperature 'T_m' were kept constant at 80 μm, 7800 kg/m^3, and 1773 K, respectively. Density and melting temperature values were reported by the powder manufacturer.

In the second stage, the surrogate model is calibrated using a Bayesian framework with the single-track measurements of the melt pool dimensions (width and depth) so that the model predictions agree with the experimental data. Calibration consists of a search for hyperparameters of the surrogate model that result in minimized prediction error. Due to the limitations of the thermal model, the error between the calibrated model predictions and the experimental measurements is still large in some regions of the processing space. A discrepancy function is then added to further reduce the prediction error of the model. To assess the performance of the calibrated model, a detailed representation of the error over the search space is plotted in the form

of two contour-maps of the absolute prediction error, displayed in Figures 5a and 5b. The mean absolute prediction error (MAPE) for width is 2.77%±2.54% and for depth is 11.95%±14.83%. The minimum and maximum prediction error for width is 0.12% and 13.67%, and for depth is 1.46% and 75.55% respectively. Although the original E-T model predicts all three melt pool dimensions (width, depth and length), only width and depth are experimentally measured (due to the difficulty in measuring the melt pool length experimentally in single tracks). Therefore, the surrogate model is calibrated using only the width and depth experimental measurements and can only be used to accurately predict these two melt pool dimensions. The predicted melt pool dimensions are then used to build the keyholing, lack of fusion, and hatch spacing criteria, and associated boundaries in the printability map, as described above.

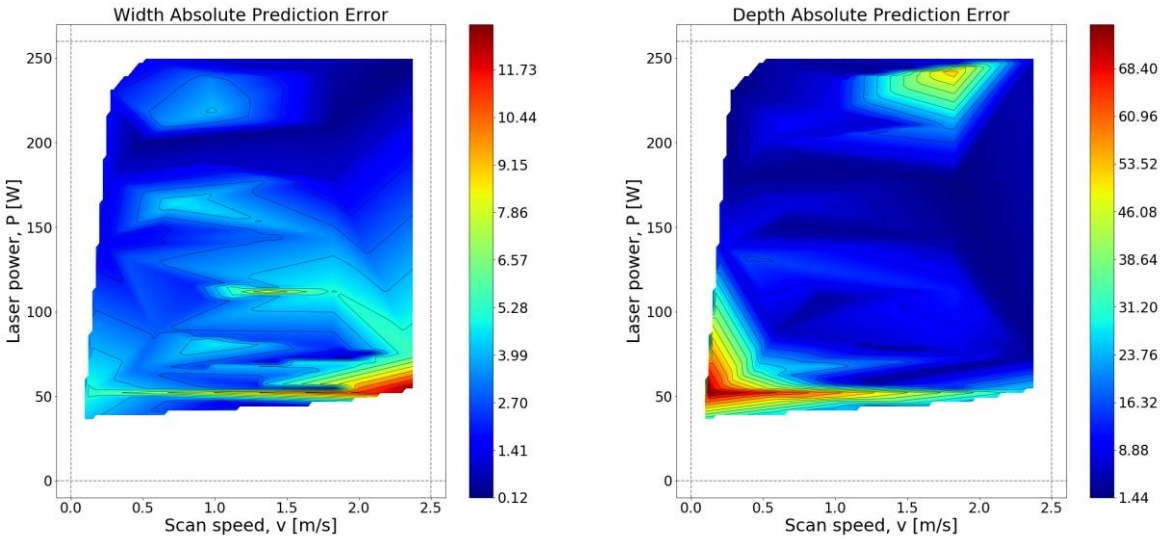

(a) (b)

Figure 5. Absolute prediction error contour maps of the E-T model after statistical calibration as compared to the experimental measurements for (a) melt pool width and (b) melt pool depth.

The mean absolute prediction errors (MAPE) for width and depth are 2.77% and 11.95%, respectively.

Geometric Hatch Spacing Criteria

The calibrated Eagar-Tsai model allows for reasonably accurate predictions of melt pool dimensions across the defined parameter space. This data can be utilized to determine hatch spacing values that promote full interlayer fusion for a given parameter set. Some studies have suggested that hatch spacing can be selected using an optimal ratio of width/hatch spacing [32,47]. The present study takes a different approach: we propose and test a geometrically derived hatch spacing criterion to calculate the maximum allowable hatch spacing to promote full fusion for a given melt pool width, melt pool depth, and layer thickness. Then we determine the maximum hatch spacing for all laser power and speed combinations in the printability/processing maps using the E-T model predictions of melt pool width and depth.

In the interest of promoting fusion between melt pools with a conservative approach to selecting hatch spacing, the transverse shape of each melt pool is assumed to be a parabola with width (*W*) and depth (*D*), as is illustrated in Figure 6a. This initial assumption only takes account of the section of the melt pool that has penetrated the substrate. The parabola intersects the substrate surface at x = W/2, therefore, the melt pool can be characterized as a function of *W*, *D*, and *x* as:

$$y(x) = \frac{4D}{W^2}x^2 \quad (1)$$

The initial melt pool is situated at the origin of our reference frame with a neighboring melt pool having a vertex at a distance equal to the hatch spacing (*h*) along the x direction. These melt pools

intersect at $x = h/2$, and their overlap depth (OD) with respect to the substrate can be calculated as $OD = D - y\ (h / 2)$. A formula for overlap depth can now be derived as:

$$OD = D(1 - \frac{h^2}{W^2}) \tag{2}$$

A full melt pool, the top and bottom of which are both parabolas with equal widths, is then taken into consideration, as illustrated in Figure 6b. This melt pool is similarly situated at a distance h from a neighboring melt pool. The overlap height (OH) of these melt pools can be calculated in a similar fashion to the overlap depth, and a relationship between OD and OH is established:

$$\frac{OD}{D} = \frac{OH}{H} \tag{3}$$

In order to have full melting during deposition of the second layer, the melt pool overlap depth of the second layer and overlap height of the first must be equivalent to at least the 2nd layer's effective substrate height, also equal to H. In other words, $OD + OH = H$. The overlap depth can then be calculated as:

$$OD = \frac{H * D}{H + D} \tag{4}$$

Since the melt pool height is not a convenient variable to predict or measure, the conservative assumption is made that the melt pool height is equal to the layer thickness (t):

$$OD = \frac{t * D}{t + D} \tag{5}$$

Plugging this result into eqn. 2, a relationship between maximum hatch spacing (h_{max}), melt pool width, melt pool depth, and layer thickness can be obtained:

$$h_{max} = W\sqrt{1 - \frac{t}{(t+D)}} \tag{6}$$

Thus, a maximum value for hatch spacing can be calculated at any given point in the process parameter space.

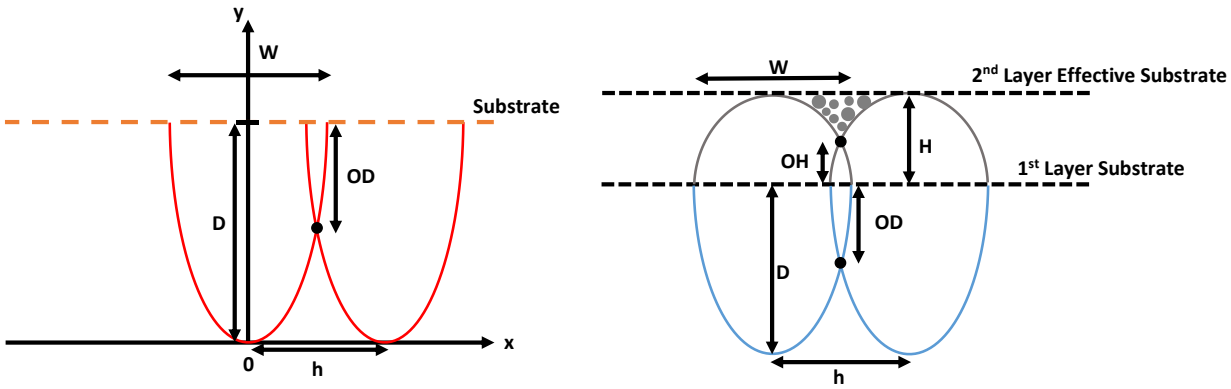

(a) (b)

Figure 6. An illustration of (a) the transverse cross section of the bottom half of two melt pools approximated to be parabolas with a reference axis, and (b) the transverse cross section of two melt pools with both their top and bottom halves approximated by parabolas. *W*: Width of the melt pool, *D*: Depth of the melt pool, *H*: Height of the melt pool, *h*: Hatch spacing – the distance between the centers of two successive laser passes, *OH*: Overlap height of two melt pools, *OD*: Overlap depth of two melt pools.

Experimental Methods

Custom gas atomized AF9628 powder was acquired from Nanoval GmbH & Co. KG. The composition of AF9628 was determined by inductively coupled plasma atomic emission spectroscopy (ICP-AES) in both the bulk and powder samples, displayed in Table 2. Single tracks, cubes, and tension samples were printed using a 3D Systems ProX DMP 200 Laser Type (fiber laser with a Gausian profile, λ = 1070 nm, and beam diameter = 80 μm) additive manufacturing system purged with high purity argon. Both the cubes and tensile specimens were printed using a

bi-directional scan strategy with a hatch angle of 45°. A constant layer thickness of 37 µm was used which is equal to the D80 of the as-received powder, where D_{xx} is the size of the cumulative distribution of the powder at XX percent. Single tracks were printed on a forged AF9628 base plate normalized at 1010 °C for two hours, then air cooled. The single tracks were 10 mm in length with 1 mm spacing between each track. Three cross sections were cut from each track using wire electrical discharge machining (EDM), and then polished down to 0.25 µm with water-based diamond suspension polishing solutions. A 4% Nital (4 ml HNO_3, 96 ml ethyl alcohol) etchant was used to reveal microstructural features in the single tracks for optical microscopy. Cubes and tension specimens were printed on forged and machine annealed AF9628 base plates. The cubes were polished and etched using the same method as the single tracks for microstructural evaluation.

Optical microscopy (OM) was carried out using a Keyence VH-X digital microscope equipped with a VH-Z100 wide range zoom lens. Scanning electron microscopy (SEM) was carried out using a FEI Quanta 600 Field Emission SEM. Wavelength dispersive spectroscopy (WDS) was performed with a CAMECA SXFive electron probe microanalyzer equipped with a LaB6 electron source. A quantitative WDS composition map of AF9628 powder was obtained at settings of 15 kV, 100 nA, and 110 µs pixel dwell time with a 0.1 µm step size. WDS maps are displayed in atomic %.

Cubes with dimensions 8×8×8 mm were printed using a range of process parameters for microstructural analysis. Cube density was measured according to the ASTM B962-15 Archimedes method using ethanol to attain submerged weight. Three OM images of the vertical cross section of each cube (with respect to the building direction) were taken for area percent porosity measurements. The measured values were averaged from these three images. Optical micrographs were processed with the ImageJ® software [76] in order to calculate the area percent

porosity in each image. X-ray Diffraction (XRD) patterns of the polished cubes were obtained using a Bruker D8 Discover X-ray Diffractometer with a Vantec 500 detector and Cu K-α X-ray source.

Electron backscattered diffraction (EBSD) imaging was performed using a FEI Quanta 200 Field Emission SEM equipped with an EDAX Team® EBSD detector. EBSD images were retrieved at 20 kV, 500x magnification, and a step size of 400 nm. Post processing of the crystallographic data was conducted in EDAX's Orientation Imaging Microscopy (OIM) Analysis software with the steps listed as follows: grain confidence index standardization (angle: 5°, size: 2); neighbor confidence index correlation (≥0.1); neighbor orientation correlation; and a single iteration of grain dilation.

Wire electric discharge machining (EDM) was used to cut flat tensile specimens with 26 mm overall length, 7 mm grip width, 3 mm gauge width, 8 mm gauge length, and 0.7 mm gauge thickness from rectangular prisms (10×10×30 mm) printed in the horizontal and vertical directions with respect to the building direction, where horizontal and vertical orientations are perpendicular and parallel to the building direction respectively. Tensile testing was conducted using an MTS 810 servohydraulic test frame at room temperature, and an extensometer with ceramic extension rods in direct contact with the gauge section of the specimens recording axial strain. Specimens were loaded at a strain rate of $5x10^{-4}$ s^{-1} until fracture. Process parameters for the specimens were selected from the optimal cube parameters.

Microstructure and Phase Diagram Feature Framework

Alloy Selection

There are currently no generally recognized criteria for the development or selection of alloy systems tailored to AM. However, insight can be gained from welding literature and studies on rapid solidification [77]. A key challenge is posed by microsegregation from dendritic solidification which can cause solidification cracking and undesirable phase formation in AM. This phenomenon depends on the speed of the solidification front and the equilibrium partition coefficient (k_e). The equilibrium partition coefficient is the ratio of solid and liquid solute concentrations in an alloy system ($k_e = C_s/C_l$). Under non-equilibrium rapid solidification conditions, such as those typical in L-PBF, the partition coefficient is velocity dependent [78]. This indicates that an increase of solidification speed through the increase in laser scan speed is expected to reduce microsegregation, as has been demonstrated in the literature [56]. However, it may not be feasible to process certain alloys at high enough speeds to completely resolve dendritic solidification. When designing alloys for AM, the equilibrium partition coefficient can be utilized to control microsegregation. An alloy with a $k_e \approx 1$ may not require high printing speeds as microsegregation is not expected to occur. It may therefore be possible to use simple equilibrium phase diagram features to select potential alloy systems that would not exhibit solute trapping. Similarly, eutectic alloys solidify into two solid phases without passing through a liquid plus solid region which would circumvent microsegregation. The coupled phases that grow during eutectic solidification become more refined with increasing cooling rate, and often display excellent mechanical properties [79,80]. The microstructural complexity and the differences in alloy compositions of multicomponent commercial alloys can make generalized analysis of printability across alloy systems difficult. For these reasons, the following four binary alloys are selected as

simple model alloy systems for L-PBF processing to assess the role of alloy composition, various phase diagram features and material physical properties on the printability and microstructure evolution during AM. Binary phase diagrams for these alloys are displayed in Figure 7 [81–83], and relevant material properties calculated using CALPHAD Thermo-Calc software [84] can be found in Table 1.

- **Ni-20at.% Cu:** A Ni-Cu alloy is selected due to its fully isomorphous system. This alloy is expected to exhibit microsegregation due to its non-unity partition coefficient (k_e = 0.74) and moderate solidification range (20 K). The lack of secondary phase formation during solidification in this alloy will serve to contrast with microstructural development in the multi-phase alloy systems selected below.
- **Ni-5at.% Al and Ni-5at.% Zr:** In order to investigate the effect of an alloy's partition coefficient on the homogeneity of AM microstructures**,** two nickel-based alloys with equivalent binary composition $Ni_{95}X_5$ (at.%), where X is the solute element, are selected. The Ni-Al and Ni-Zr systems are ideal for testing partition coefficient effects due to the significant difference in solute partitioning. Ni-5at.% Al is expected to display little to no microsegregation as its liquidus and solidus are nearly identical for all temperatures and its k_e = 0.96. However, significant microsegregation is expected in the Ni-5at.% Zr alloy due to the large freezing range (172 K) and low partition coefficient (k_e = 0.11).
- **Ni-8.8at.% Zr:** This composition of the Ni-Zr system is selected in order to study and contrast the effects of L-PBF processing conditions on a eutectic alloy in comparison with the previously selected alloys. Eutectic alloys exhibit coupled growth between two phases that exchange mass ahead of the solidification front. Under very rapid

solidification conditions, microstructural formation can become dominated by nucleation of the uncoupled solid phases. This effect is termed anomalous growth and is due to solidification time scales becoming too short for effective diffusion to occur ahead of the solidification front [85,86]. If this does not occur, microsegregation is not expected to be observed in the eutectic alloy. Instead, a fine lamellar structure may be expected due to the high cooling rates characteristic of the L-PBF process [2].

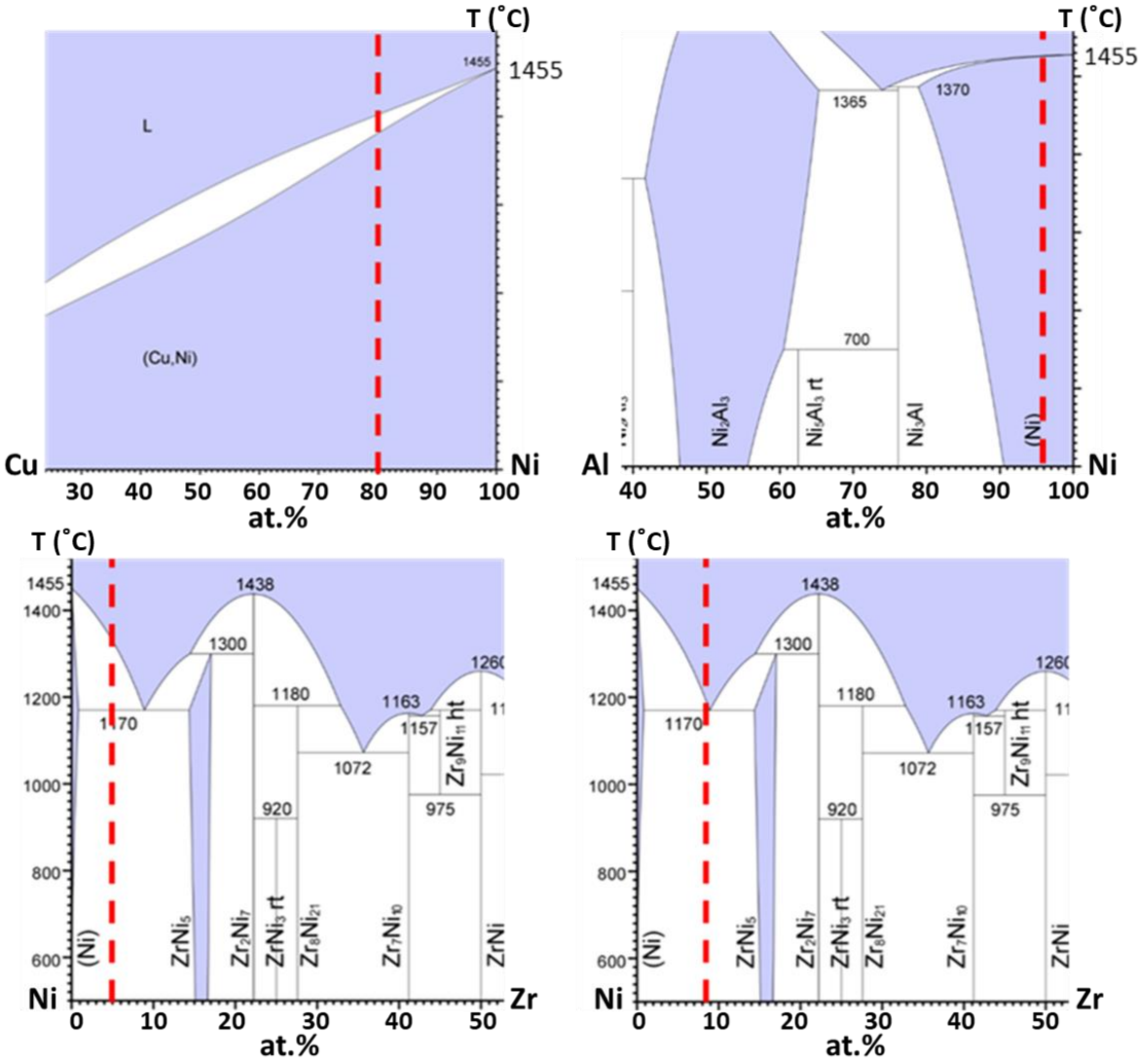

Figure 7. Binary phase diagrams of the four alloys used in this study: Ni-20at.% Cu, Ni-5at.% Al, Ni-5at.% Zr, and Ni-8.8at.% Zr [81–83]. The dashed red lines indicate the alloy composition within each of the phase diagrams.

Table 1. Material properties of the four alloys used in this study: Ni-20at.% Cu, Ni-5at.% Al, Ni-5at.% Zr, and Ni-8.8at.% Zr. The values in this table were calculated using CALPHAD Thermo-Calc software [84].

Alloys (at.%)	**Solidification Range (ΔT)**	**Partition Coefficient (k_e)**	**Melting Temperature (°C)**
Ni-20at.% Cu	20	0.74	1377
Ni-5at.% Al	0.2	0.96	1417
Ni-5at.% Zr	172	0.11	1327
Ni-8.8at.% Zr	0	1	1167

Microsegregation Processing Maps

The calibration framework outlined in Section 2.2.2. provides processing maps detailing porosity formation regions in the L-PBF parameter space. However, these maps do not provide information detailing changes in microstructural features across the parameter space. One difficulty in characterizing microstructural feature differences is the quantification of these features. Microsegregation of solute elements can be measured using energy dispersive (EDS) or wavelength dispersive spectroscopy (WDS), however, generating this data for a large number of samples is preventatively costly and time consuming. Primary dendrite arm spacing (PDAS) in microsegregation structures has been demonstrated to be dependent on both laser power and scan speed in L-PBF [56]. However, PDAS can vary significantly at different locations within a single melt pool [56]. It is therefore crucial to note that PDAS is used as a convenient quantifiable value

with the intent of qualitatively mapping microsegregation across the parameter space. PDAS values measured in single tracks will likely not be representative of PDAS values in bulk parts. However, a decreasing trend in PDAS values within the parameter space is expected to indicate a decrease in overall microsegregation within a part. In order to map microsegregation in each alloy across the laser power-scan speed parameter space, PDAS is measured in each of the 46 single tracks printed for all four alloy systems. Interpolation over the laser power-scan speed parameter space is then conducted on the PDAS dataset via multilevel B-splines approximation using the R function *mba.surf* in the *MBA* package [87] in order to generate heat maps based PDAS values in the laser power-scan speed parameter space. Observations of planar growth instead of cellular-dendritic growth structures are indicated by zero values in the heat map. These maps are validated by WDS composition maps of the single tracks and cubes. Lastly, the heat maps are combined with the porosity-free processing maps to detail a processing region that will result in full density parts with desired microstructural outcomes.

Materials Fabrication and Characterization

Gas atomized Ni-5at.% Al, Ni-20at.% Cu, Ni-5at.% Zr, and Ni-8.8at.% Zr powder provided by Nanoval GmbH & Co. KG were used to manufacture L-PBF single tracks and cubes. These specimens were printed using a 3D Systems ProX DMP 200 commercial L-PBF system (fiber laser with a Gaussian profile λ = 1070 nm, and nominal beam diameter = 80 μm).

Single tracks were printed on a base plate of the same composition as each respective alloy. Base plates were all procured in the as-cast condition. The Ni-5 at.% Al as-cast base plate was subjected to homogenization at 1100 ˚C for 1 hour, 50% cold rolling, and recrystallization at 700 ˚C for 1 hour. The Ni-20 at.% Cu as-cast base plate was subjected to homogenization at 1100 ˚C

for 1 hour, 50% cold rolling, and recrystallization at 800 ˚C for 1 hour. The Ni-5 at.% Zr as-cast base plate was subjected to homogenization at 1000 ˚C for 1 hour and 38% hot rolling at 850 ˚C. The Ni-8.8 at.% Zr as-cast base plate was subjected to homogenization at 850 ˚C for 1 hour and 12.6% hot rolling at 800 ˚C. Single tracks were 10 mm in length with 1 mm spacing between tracks, and each material was printed at the same 46 combinations of laser power and scan speed with a constant powder layer thickness of 49 µm, which roughly corresponds to the d80 of the powders (the 80th percentile of the powder size distribution). Cross sections of the single tracks were cut using wire electrical discharge machining (EDM), and these specimens were polished down to 0.25 µm with water-based diamond suspension polishing solutions, and vibratory polished with 0.04 µm colloidal silica for 2 hours. Kalling's Solution No. 2 (5 g CuCl2, 100 mL HCl, and 100 mL ethanol) was used to etch the single tracks to obtain optical and backscattered electron micrographs. Melt pool dimensions were taken from the average values measured in cross sectional images of each single track at three locations. Primary dendrite arm spacing (PDAS) was imaged using backscattered electron micrographs of the single track cross sections in the as-etched condition. At least 20 PDAS measurements were made at the melt pool edge of each single track. Three cross sections of each single track were used for analysis of PDAS to ensure that the observations were representative of the entire melt pool. Single tracks displaying planar growth were marked as having a PDAS of 0 µm. Square cubes (8×8×8 mm) were printed using the process parameters listed in Table 4 for microstructural analysis.

Optical microscopy (OM) was carried out using a Keyence VH-X digital microscope equipped with a VH-Z100 wide range zoom lens. Wavelength dispersive spectroscopy (WDS) was performed with a CAMECA SXFive electron probe microanalyzer equipped with a LaB_6 electron source. Quantitative WDS composition maps were obtained at settings of 15 kV, 50 nA, and 110

µs pixel dwell time with a 0.1 µm step size. WDS was carried out on specimens in the as-polished condition, and WDS maps are displayed in atomic% (at.%). Backscattered electron images were taken using a FEI Quanta 600 SEM equipped with a field emission electron source.

POST-PROCESSING TREATMENT FOR AF9628 ULTRA-HIGH STRENGTH STEEL*

Experimental Methodology

Laser Powder Bed Fusion of AF9628

AF9628 powder was gas atomized by Nanoval GmbH & Co. KG. The manufacturer reported the cumulative size distribution of the powder at 50% (i.e. D50) and 80% (i.e. D80) as 25.8 μm and 37 μm respectively. Inductively coupled plasma atomic emission spectroscopy (ICP-AES) was conducted to measure the composition of both the powder and as-printed LPBF samples and is displayed in Table 2. A 3D Systems ProX DMP 200 commercial LPBF system with a Gaussian profile fiber laser, nominal beam diameter of 80 μm, and a wavelength λ of 1070 nm was used for printing in a high purity argon atmosphere to prevent oxygen contamination. Cubes for microstructural analysis and rods for tension samples and Charpy impact blocks were printed using this instrument. A bi-directional scan strategy with a layer rotation of 90° was used for all specimens. The specimens were printed based on one of the optimal parameter sets previously reported by Seede et al. [21], namely, the laser power of 175 W, scan speed of 1 m/s, hatch spacing of 70 μm, and 37 μm layer thickness (which is the D80 of the powder). The material of the base plate was forged and machine annealed AF9628 steel and all specimens were printed on these base plates. An illustration of the orientation, sample dimensions, and distribution within the platform for the laser powder bed fusion manufactured tension and Charpy blocks is displayed in Figure 8a.

Table 2. AF9628 martensitic steel composition in the powder and as-printed conditions determined using Inductively Coupled Plasma – Atomic Emission Spectroscopy (ICP-AES) analysis and combustion-infrared absorbance.

Elements (wt.%)	**Standards** [48]	**Powder**	**As-Printed**
Fe[1]	Balance	93.29	93.53
Ni	<3.00	1.03	0.97
Cr	2.00-3.00	2.69	2.61
Mo	0.50-1.50	0.92	0.92
Si	<1.25	1.01	0.90
Mn	<1.00	0.55	0.65
C[2]	0.24-0.32	0.26	0.23
V	0.05-0.35	0.07	0.09
Cu	<0.15	0.14	0.08
Al	<0.025	0.02	0.01
Co	-	0.02	0.01

1: Determined by difference

2: Determined using combustion-infrared absorbance

Post-Processing Treatments

As discussed in the introduction, Vaughan et al. [51] reported a successful quench and temper treatment schedule for as-forged AF9628 bulk material. These findings formed the basis for the heat treatment schedules selected for this work. Additionally, the LPBF process often results in significant residual stress accumulation in as-printed parts and may lead to warping or cracking during heat treatment [2]. As such, three heat treatment schedules were selected for testing; two include an initial stress relief heat treatment while one does not, following the schedule reported

in the literature [51]. The following heat treatments were applied to the printed cubes and tensile test specimens in the as-printed condition, and are labeled HT1, HT2, and HT3 for the remainder of this study. To determine whether a normalization step is necessary prior to austenitization and quenching in the as-printed samples, the heat treatment schedule labeled HT1 includes a normalization heat treatment while HT2 does not. HT1 and HT2 heat treatment schedules also include a stress relief step before the normalization step while HT3 begins directly with normalization to determine whether the step is required to mitigate heat treatment induced cracking. These heat treatments are listed below and illustrated in Figure 8b for visual clarity.

- **HT1**: Stress relief (680 °C for 2 hours then air cooled), normalization (1010 °C for 2 hours then air cooled), austenitization (1010 °C for 1.5 hours then water quenched), and tempering (200 °C for 4 hours then air cooled).
- **HT2**: Stress relief (680 °C for 2 hours then air cooled), austenitization (1010 °C for 1.5 hours then water quenched), and tempering (200 °C for 4 hours then air cooled).
- **HT3**: Normalization (1010 °C for 2 hours then air cooled), subcritical annealing (680 °C for 4 hours then air cooled), austenitization (1010 °C for 1.5 hours then water quenched), and tempering (200 °C for 4 hours then air cooled). This treatment follows exactly what was reported by Vaughan et al. [51] for as-forged AF9628 steel and termed a “baseline” treatment in the study.

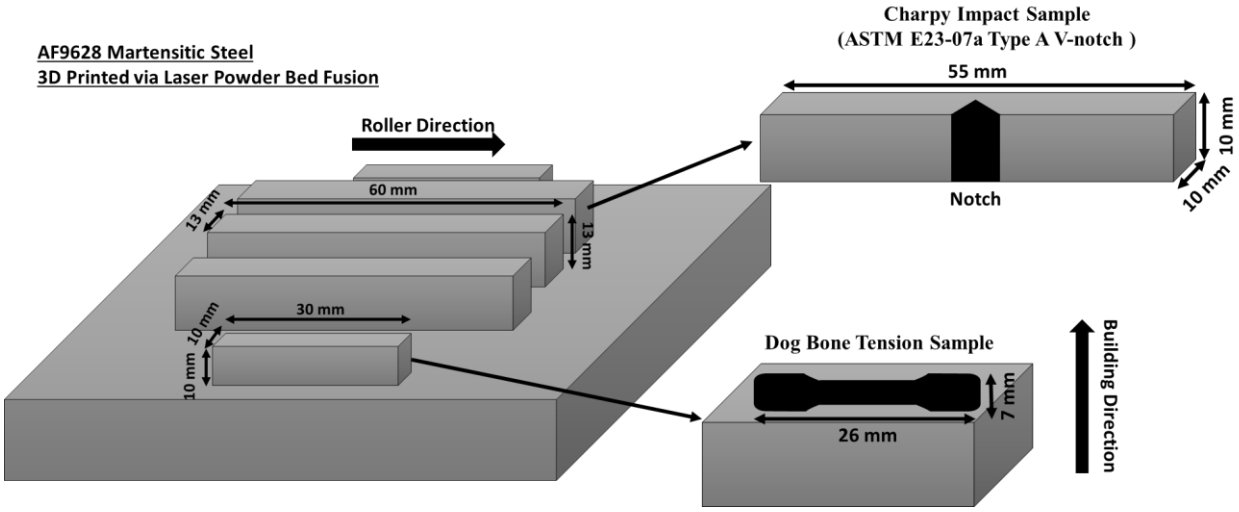

(a)

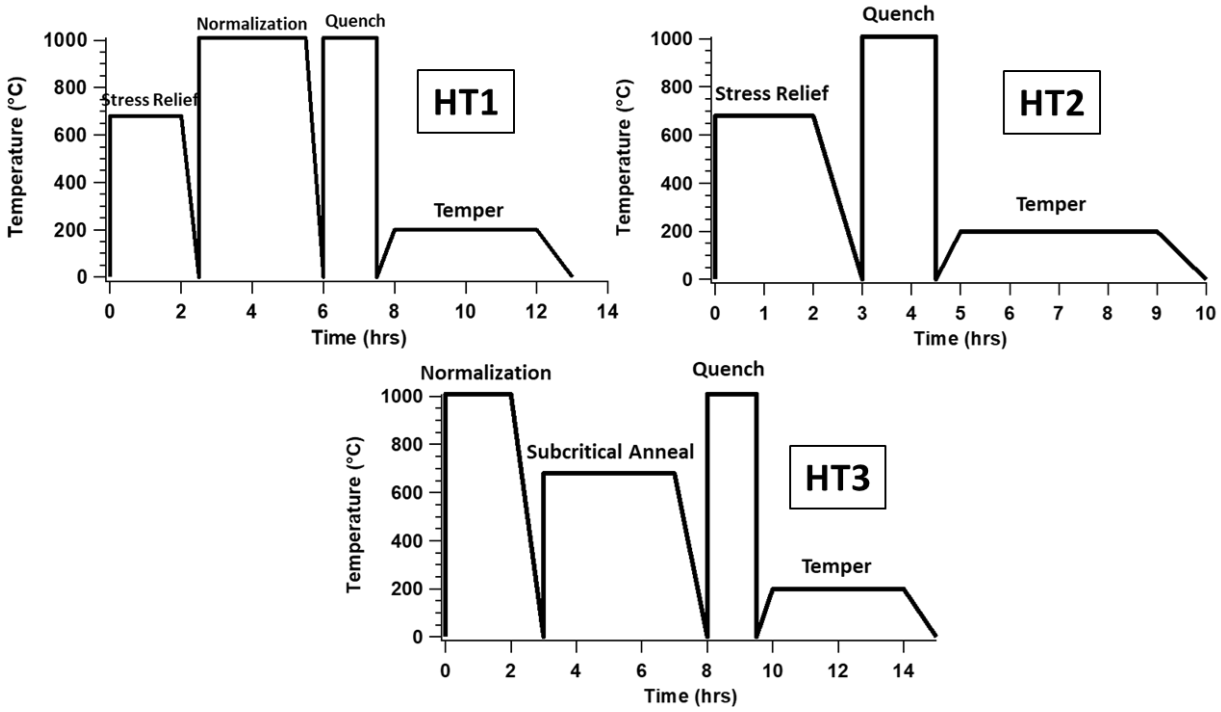

(b)

Figure 8. a) An illustration of the orientation, sample dimensions, and distribution within the platform for the laser powder bed fusion manufactured tension and Charpy blocks printed in this study. b) An illustration of the three heat treatments applied to laser powder bed fusion

manufactured samples of AF9628 martensitic steel. These heat treatments are labeled HT1, HT2, and HT3.

Microstructural Characterization

8×8×8 mm^3 square cubes were printed using the process parameters described in Section 2.1 to perform microstructural analysis. Density of these cubes was measured in the as-printed condition using the Archimedes method (ASTM B962-15) with ethanol as the displacement liquid. As-printed specimens were observed to have greater than 99% density, with an average density of 99.4%. Wire electrical discharge machining (EDM) was used to cut cross sections of the cubes in each condition (as-printed, HT1, HT2, and HT3). These cross sections were polished using diamond suspension solutions down to 0.25 µm. Vilella's reagent (1 g picric acid, 5 ml HCl, 100 ml ethyl alcohol) was used to reveal melt pool boundaries and prior austenite grains for OM. A 4% Nital (4 ml HNO_3, 96 ml ethyl alcohol) etchant revealed martensitic laths for SEM analysis. A Keyence VH-X digital microscope equipped with a VH-Z100 wide range zoom lens was used to acquire optical micrographs of the material. A FEI Quanta 600 Field Emission SEM was used to obtain SEM micrographs. Quantitative WDS composition maps of AF9628 were obtained using a CAMECA SXFive electron probe microanalyzer equipped with a LaB6 electron source, operated at 15 kV, 50 nA, and 110 µs pixel dwell time with a 0.1 µm step size. XRD patterns for each condition were measured using a Bruker D8 Discover X-ray Diffractometer equipped with a Cu K-α X-ray source and a Vantec 500 area detector. The measurements were conducted with a step size of 0.01˚, a scanning rate of 1.5˚ per minute, and a maximum power of 40 kV. EBSD maps were collected from the as-printed materials with an FEI Quanta 200 Field Emission SEM using an EDAX Team® detector. These data were post-processed using EDAX's Orientation Imaging Microscopy (OIM) Analysis software. EBSD maps of the heat-treated material were taken with a

Tescan FERA-3 SEM and post processed using the Oxford® software AZtecCrystal. EBSD images of the materials in all conditions were obtained at settings of 500x magnification, 20 kV, and 400 nm step size. Prior austenite grain (PAG) maps were extracted from EBSD data according to a grain boundary thresholding criteria reported to accurately characterize PAG size [51,88,89]. This criterion, selected for its simplicity, isolates martensite misorientation angles between 15-48˚ to reconstruct parent PAG boundaries [51]. The grain boundary maps constructed by this method are used to determine PAG sizes in each condition of AF9628 using the ASTM E112-13 Heyn lineal intercept procedure. Martensite lath sizes were calculated at misorientation angles below 15˚ using the Oxford® software AZtecCrystal.

Mechanical Property Characterization

Vickers microhardness measurements were conducted using a LECO® LM300AT microhardness tester. Microhardness indentations were performed at $\frac{1}{13}$ kg/s at 0.4 mm intervals along the building direction in the 8×8×8 mm cubes used for microstructural analysis. Rectangular prisms were printed with the following dimensions for tensile and Charpy impact samples, respectively: 10×10×30 mm, and 12×12×58 mm. Flat dog bone shaped tensile specimens were EDM cut in the following dimensions: 26 mm overall length and 8 mm x 3 mm x 0.7 mm gauge dimensions. Charpy impact samples were wire EDM cut according to ASTM E23-07a Type A V-notch standards. An MTS 810 servohydraulic test frame was used to test the samples to failure under tension at room temperature. The axial strain was recorded using an MTS extensometer directly attached to the gauge section of each specimen. Three specimens in each condition were loaded at an effective strain rate of $5x10^{-4}$ s^{-1} until fracture. Charpy impact testing was conducted at -40 °C for 3 samples in each condition using a Tinius Olsen Model 74 Charpy impact tester with a Model 892 display.

RESULTS AND DISCUSSION*

AF9628 Parameter Optimization

Powder Characterization

Gas atomized AF9628 powder size distribution and morphology can be seen in Figures 9a and 9b. Microdendritic features, grain boundaries, and satellite particles can be observed in the high magnification SEM image presented in Figure 9b. The manufacturer reported that the powder had a D50 of 22.6 µm and a D80 of 37 µm. Etched cross sections of the powder revealed a martensitic lath dominated microstructure and light regions running through these laths, as can be seen in Figure 10. WDS maps of unetched cross sections of the powder are displayed in Figure 10 and reveal that these regions contain segregated amounts of Cr, Ni, Si, Mo, Mn, and V, and a corresponding depletion of Fe.

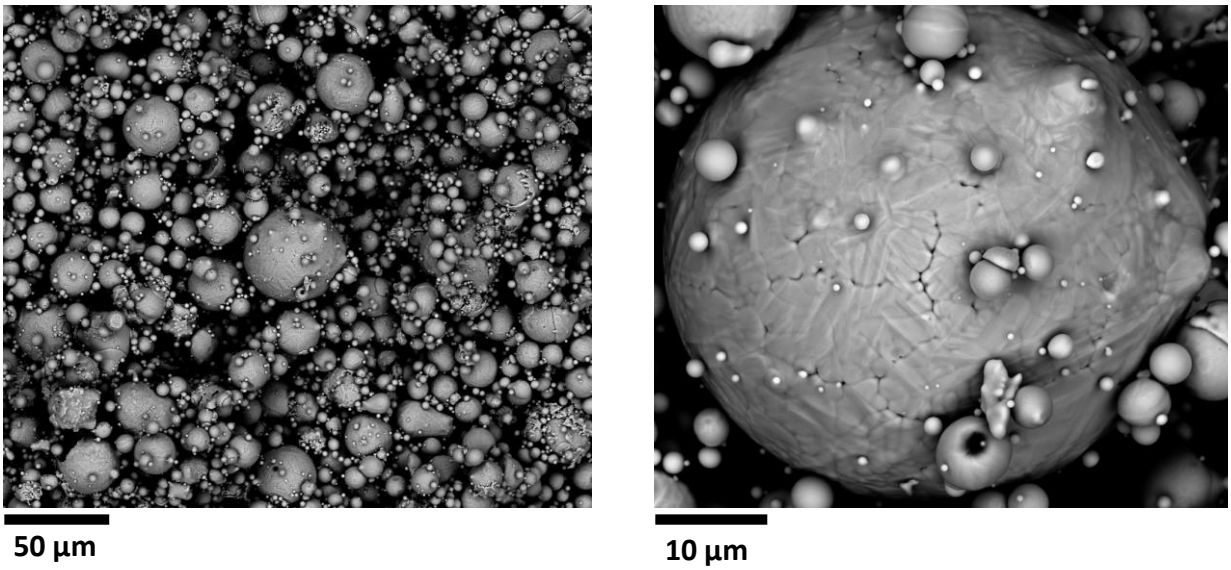

(a) (b)

Figure 9. Back-scattered electron images of gas atomized AF9628 powder particles. (a) A low magnification image showing the powder size distribution. (b) A high magnification image showing the surface morphology of a characteristic powder particle.

Segregation of constituent elements occurs during solidification, and is typically observed as a cellular structure due to the rejection of solute elements to the liquid phase [59]. After solidification, these regions of segregation are likely to reside within larger austenite grains. Due to rapid cooling in the gas atomization process [60], martensite begins forming within prior austenite grains [23,61]. These martensitic laths appear to cross through light regions of segregation as displayed in Figure 10.

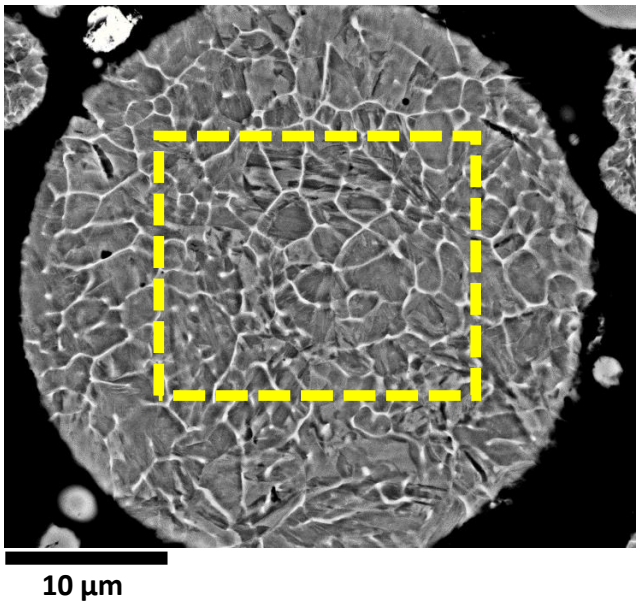
10 µm

(a)

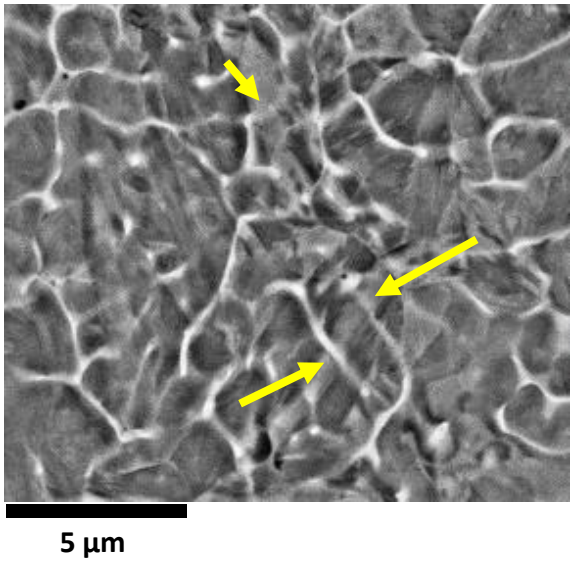
5 µm

(b)

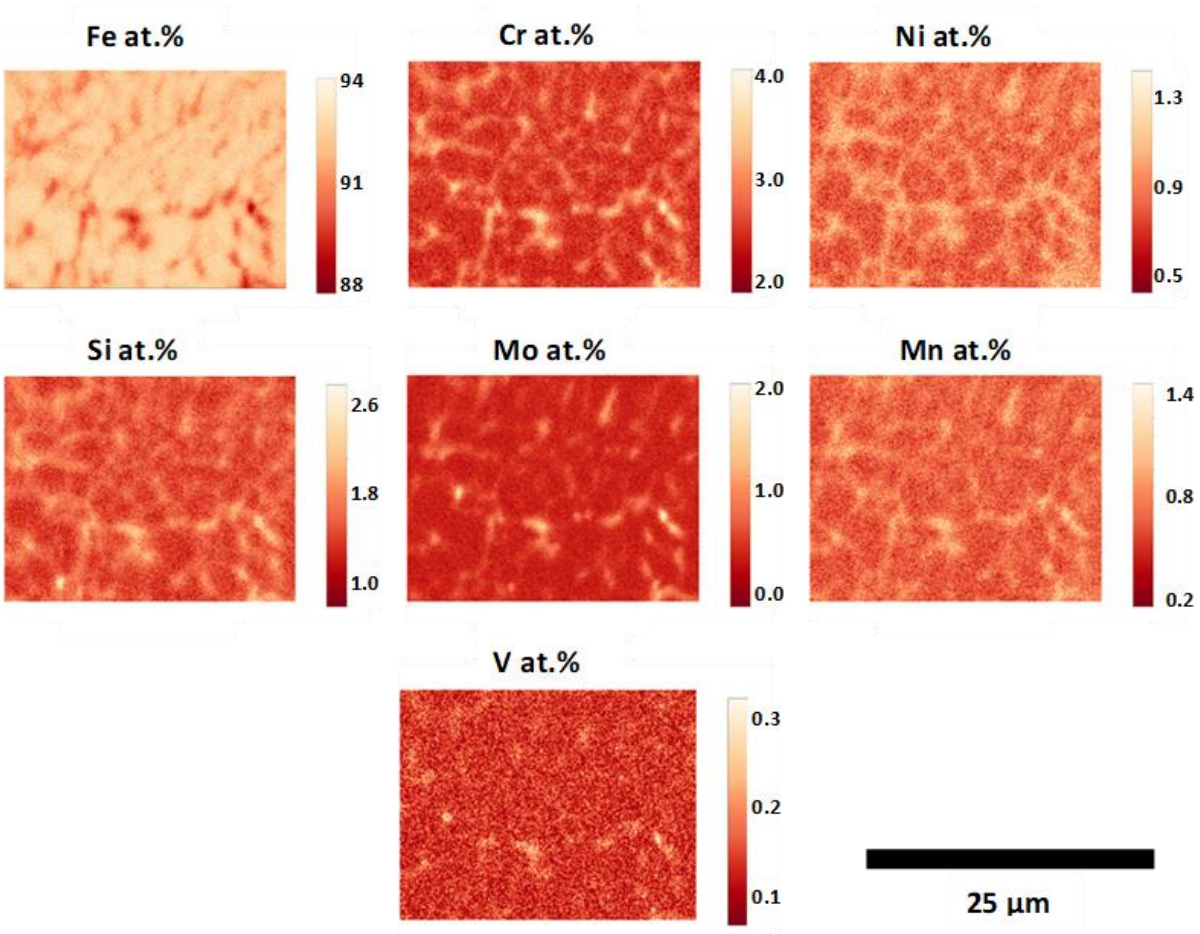
Fe at.%
94
91
88
Cr at.%
4.0
3.0
2.0
Ni at.%
1.3
0.9
0.5
Si at.%
2.6
1.8
1.0
Mo at.%
2.0
1.0
0.0
Mn at.%
1.4
0.8
0.2
V at.%
0.3
0.2
0.1
25 µm

(c)

Figure 10. Back-scattered electron images of an etched, gas atomized AF9628 powder particle are displayed in (a) and (b) revealing martensitic laths and white segregation. The yellow dotted box overlaid in (a) is a visual reference for the WDS maps in (c). The yellow arrows indicate white segregation regions crossing over martensitic laths. Each map in (c) has a scale bar to its right representing the chemical composition in at.%.

Process Parameter Optimization

In order to validate the boundaries of the printability region predicted by the calibrated E-T model, experimental single tracks were classified as tracks likely to feature either keyholing, balling, lack of fusion or as good tracks, and plotted in the laser power – laser scan speed processing space in Figure 11a. Representative images of single tracks in each condition (lack of fusion, keyholing, good track, and balling) are displayed in Figure 4b. Balling and keyholing single-tracks were identified qualitatively based on their characteristic melt pool shapes, as shown in Figure 4b and previously described in detail [2,29,39,90,91]. Lack of fusion tracks were classified based on the criterion of experimentally measured $D \leq$ t.

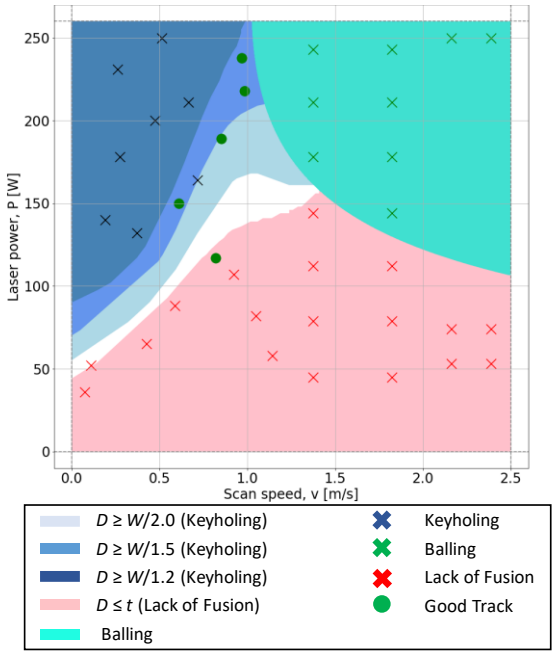
Laser power, P [W]
Scan speed, v [m/s]
D ≥ W/2.0 (Keyholing)
D ≥ W/1.5 (Keyholing)
D ≥ W/1.2 (Keyholing)
D ≤ t (Lack of Fusion)
Balling
Keyholing
Balling
Lack of Fusion
Good Track

(a)

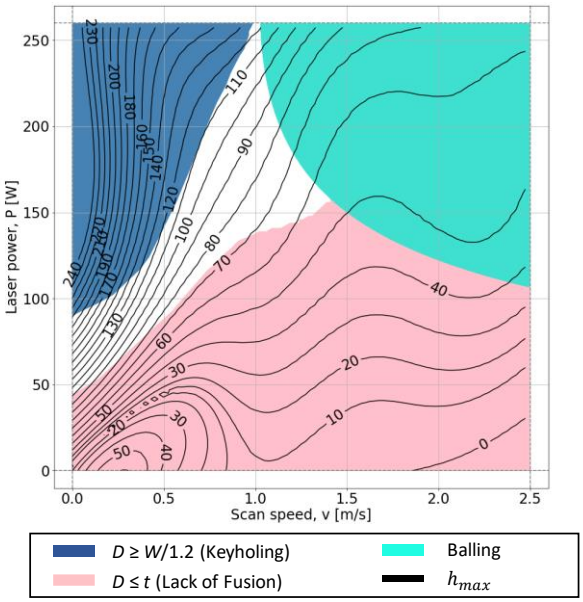
Laser power, P [W]
Scan speed, v [m/s]
D ≥ W/1.2 (Keyholing)
D ≤ t (Lack of Fusion)
Balling
h_{max}

(b)

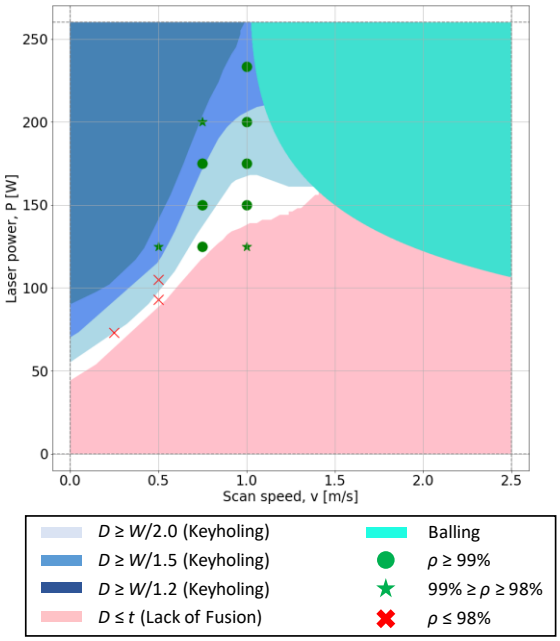
Laser power, P [W]
Scan speed, v [m/s]
D ≥ W/2.0 (Keyholing)
D ≥ W/1.5 (Keyholing)
D ≥ W/1.2 (Keyholing)
D ≤ t (Lack of Fusion)
Balling
ρ ≥ 99%
99% ≥ ρ ≥ 98%
ρ ≤ 98%

(c)

Figure 11. Process parameter maps with different keyholing criteria (W/D ≤ 1.2, 1.5, 2.0) and a lack of fusion criterion (D ≤ t) predicted by the calibrated Eager - Tsai model, and a balling region fit to single track experiments using a Support Vector Machine (SVM) classifier. (a) Experimentally characterized and classified single-track experiments for keyholing, lack of fusion, balling, and good tracks, marked with different symbols and colors in the process parameter map. (b) Maximum hatch spacing contours to achieve porosity-free printed parts calculated using the geometric hatch spacing criterion introduced in section 2.1.4. (c) Laser power and scan speed combinations selected in the good track region for printing cubes (and corresponding maximum hatch spacing in (b)), and their densities measured using Archimedes method plotted in the process parameter map. *D*: Melt pool depth, *W*: Melt pool width, *t*: powder layer thickness, h_{max}: Maximum hatch spacing to achieve porosity-free parts, ρ: Density.

Figure 11a also displays the process parameter map (shaded regions) constructed with different keyholing criteria ($W/D \leq 1.2, 1.5, 2.0$) and a lack of fusion criterion ($D \leq t$), using the D and W values predicted by the calibrated E-T model. The balling region displayed in Figure 11a is fit to single track experiments using the SVM mentioned in section 2.1. The keyholing criterion $W/D < 1.2$ fits all of the experimentally identified keyholing tracks except for one and did not misclassify any tracks as having undergone keyholing. The criteria $W/D < 1.5$ and $W/D < 2.0$ misclassified 3 and 4 single tracks, respectively, as having undergone keyholing. Based on its successful single-track characterization, the W/D criterion of 1.2 was chosen to be the upper boundary for the printability region.

The process parameter map introduced in Figure 11a is presented in Figure 11b with maximum hatch spacing contours calculated using the geometric hatch spacing criterion discussed in Section

2.1.4. Based on the good track regions identified in Figure 11a and the calculated maximum hatch spacing for a given laser power and scan speed set, the parameters to print cubes were selected within the good print region (white colored region in Figure 11b), the regions of each keyholing criteria, and one selection below the lack of fusion line as illustrated in Figure 11c. These selections were made in order to determine the effect of varying regions of process parameters on part porosity. The maximum hatch spacing for each cube parameter set was calculated based on the calibrated E-T predictions of melt pool dimensions. The calculated maximum hatch spacing was rounded down to the nearest multiple of 5 μm for each cube in order to test the feasibility of this criteria. The parameter set and measured Archimedes density of each cube are listed in Table 3.

Table 3. A list of the processing parameters (laser power, scan speed, hatch spacing (*h*), and layer thickness (*t*)) selected to print cubes with the dimensions of 8 mm x 8 mm x 8 mm for AF9628 ultra-high strength steel in and near the good track region in Figure 11. These parameters were determined by the proposed optimization framework. A list of calculated linear energy density (LED) and volumetric energy density (VED) for each parameter set, and the density of the printed cubes measured using the Archimedes method are also displayed.

Cube	Power (W)	Speed (mm/s)	*h* (μm)	Layer Thickness, t (μm)	LED (J/m)	VED (J/mm^3)	Archimedes Density (%)
1	73	250	90	37	292.00	87.7	74.47
2	93	500	65	37	186.00	77.3	87.89
3	105	500	80	37	210.00	70.9	94.82
4	125	500	100	37	250.00	67.6	98.64
5	125	750	75	37	166.67	60.1	99.43

6	150	750	90	37	200.00	60.1	99.39
7	175	750	100	37	233.33	63.1	99.38
8	200	750	115	37	266.67	62.7	98.94
9	125	1000	55	37	125.00	61.4	98.87
10	150	1000	60	37	150.00	67.6	99.12
11	175	1000	70	37	175.00	67.6	99.40
12	200	1000	80	37	200.00	67.6	99.16
13	233.3	1000	105	37	233.30	60.1	99.29

Density Analysis

Cubes printed between the lack of fusion criterion and the keyholing criterion of $W/D = 1.2$ had densities above 98% at speeds > 500 mm/s, as can be seen in Figure 11c. The cube printed below the lack of fusion line also displayed a density > 98%. At low speeds (≤ 500 mm/s) and laser power (≤ 115 W), however, cube density dropped below 95%. This drop in density may be explained by potentially inaccurate melt pool predictions of the calibrated E-T model. The region surrounding cubes 1 – 3 (Figure 11c) in the process parameter map did not contain any single tracks to calibrate the E-T model to (Figure 4a), increasing the possibility of error in the E-T melt pool predictions. The error associated with this region can be seen in the contour maps in Figures 5a and 5b, where the absolute prediction error for D in the region surrounding cube 1 is up to 50%.

Based on the Archimedes density measurements performed on the cubes, the process parameters for printing porosity-free tension specimens were selected. The parameters for cubes 5, 7, 11, and 13 were selected for printing tensile specimens and tensile testing, due to their high

relative densities (all selected parameter sets showed an Archimedes density > 99.25%), and to represent different regions of the parameter space.

Figure 12 shows SEM images of the AF9628 cubes' top surfaces. Cubes 1 – 3 (Figures 12a – 12c) exhibit poor surface quality with large spatter particles distributed along the surface. This is due to the relatively high volumetric energy density (VED = $\frac{P}{v*h*t}$) for these parameter sets causing particles to spatter out of the molten pool on to the part surface [92]. Cubes 4 – 13 (Figures 12d – 12m) show improved melt pool overlap with some unmelted spherical particles along the surface. Cubes 4, 6, and 8 (Figures 12d, 12f, 12h) appear to have small gaps between tracks with powder particles inside. These gaps indicate lack of fusion porosity within the builds in agreement with the relatively lower density observed in Archimedes density measurements for cubes 4 and 8. Ten width measurements were taken and averaged from the tracks on top surface of the cube 8 (Figure 12h) in order to compare it with the width predicted by the calibrated E-T model. The measured width of these tracks was 115.5 ± 11.6 μm, whereas the predicted width from the calibrated E-T model was 133.5 μm. This 15.6% difference between the predicted and actual widths, the unknown prediction error for the depth, and the 11.6 μm experimental variance are likely to be the main factors responsible for the observed lack of fusion. However, this error also indicates the robustness of the hatch spacing criteria developed in this study. A relatively significant prediction error of 15.6% for the width and 10.0% experimental variance still result in 98.94% density measured by Archimedes method, and only 0.78% porosity measured by optical microscopy displayed in Figure 13.

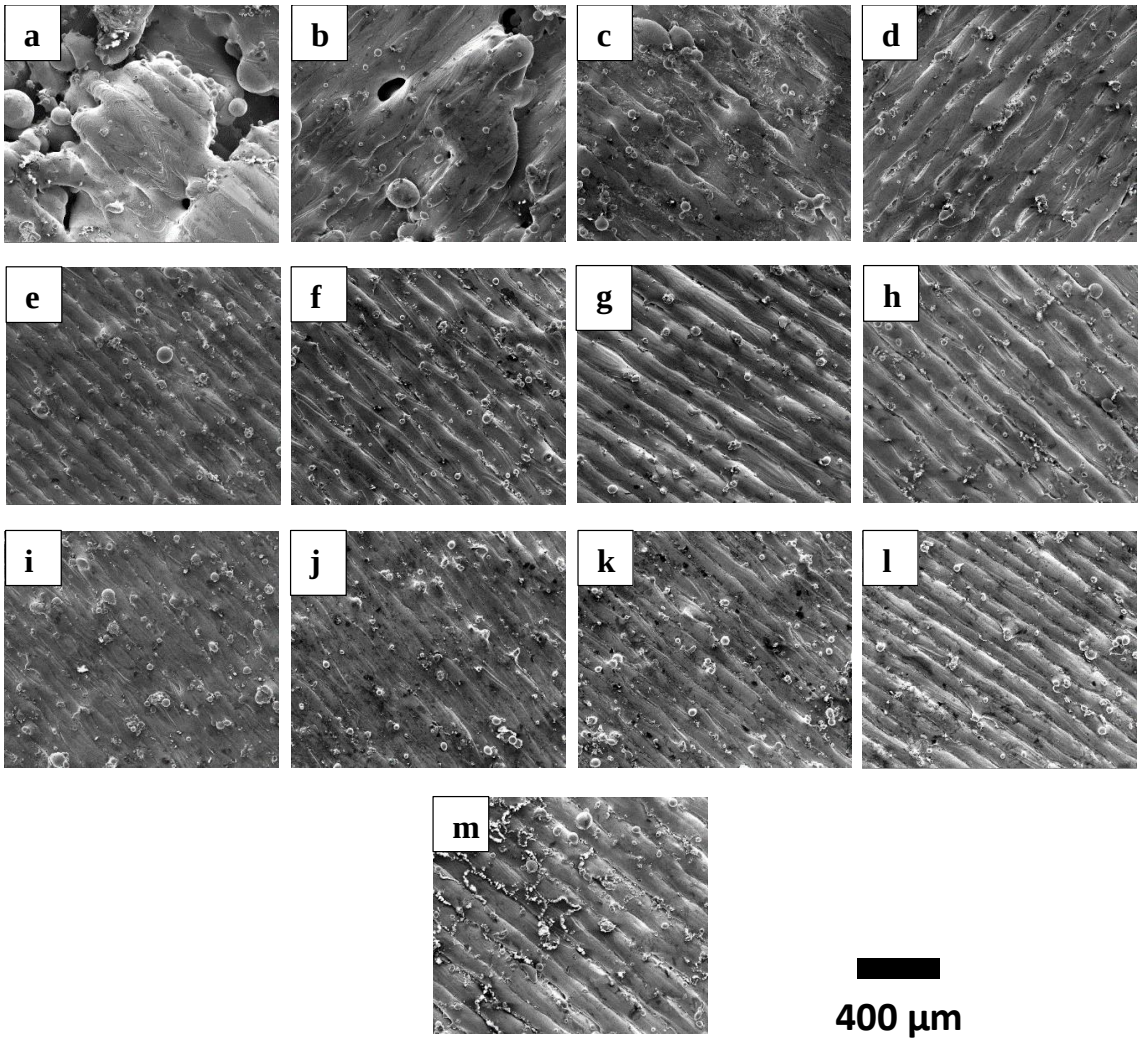

Figure 12. Scanning electron microscopy micrographs of the top surfaces of the AF9628 ultra-high strength martensitic steel cubes printed in and around the good tracks region of the laser power - scan speed printability map shown in Figure 11c. (a) through (m) Cubes 1 through 13 listed in Table 3, respectively.

Optical micrographs of the polished cube cross sections, displayed in Figure 13, are consistent with the Archimedes density measurements and top surface images. Large (> 200 µm) elongated pores with sharp edges are observed in cubes 1-3 (Figures 13a – 13c). These pores are caused by

large spattered particles disrupting the build [92]. All other cubes (Figures 13d – 13m) contained less than 1% porosity, as determined by OM image analysis. Cubes 4, 7, 8, and 13 (Figures 13d, 13g, 13h, and 13m) contained small (< 50 µm) pores with sharp edges stemming from lack of fusion between laser tracks. All of the cubes (Figure 13a – 13m) contained small (< 20 µm) spherical pores characteristic of parts printed with gas atomized powder [2].

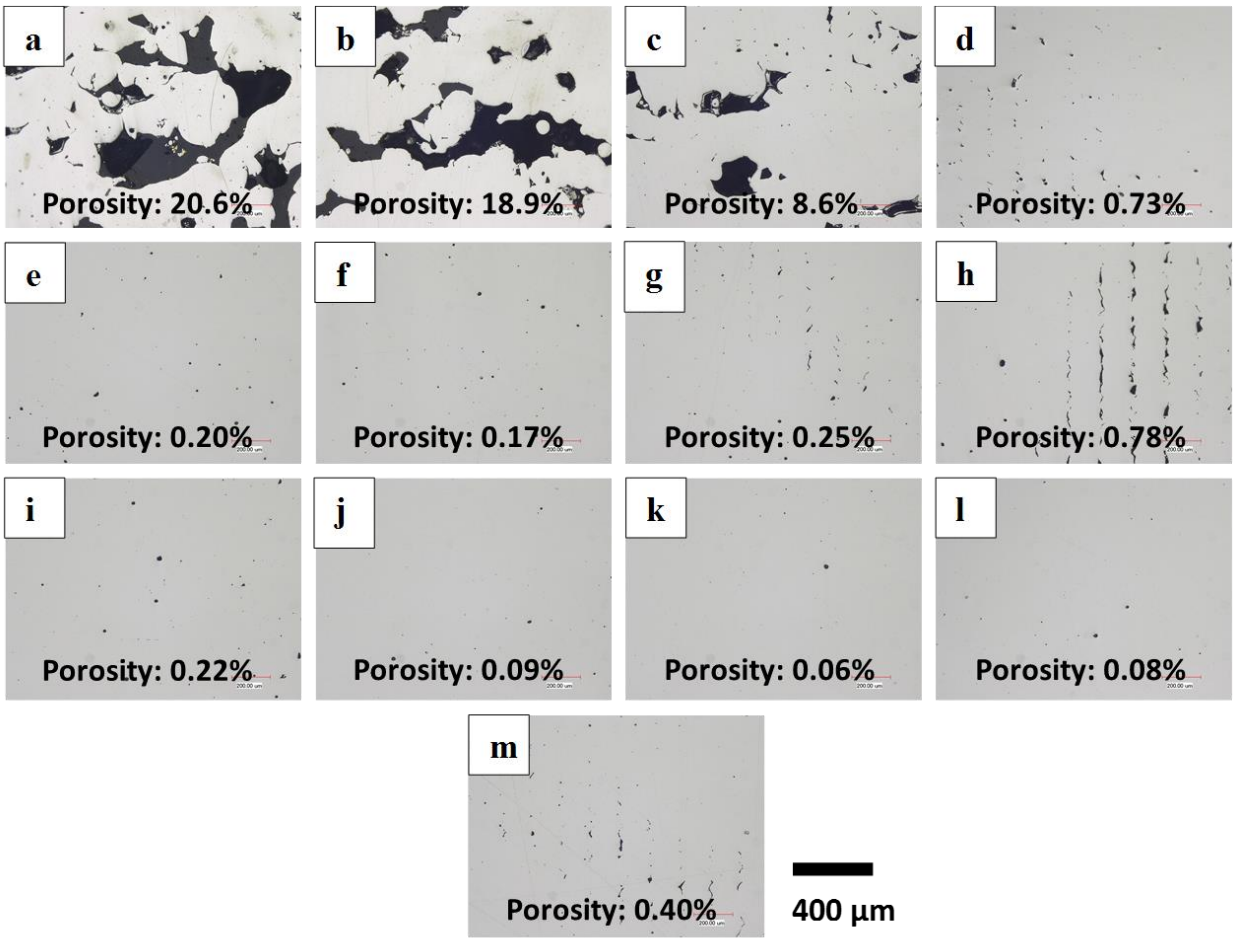

Figure 13. Optical micrographs of the polished cross sections of the AF9628 ultra-high strength martensitic steel as-printed cubes displaying the porosity values measured using area analysis of the images. (a) through (m) are optical micrographs from the as printed Cubes 1 through 13 listed in Table 3, respectively.

Considering the above observations and process parameters listed in Table 3, it is clearly apparent that AF9628 is sensitive to high volumetric energy density (VED). Successfully printed cubes had VEDs between 60.1 and 67.6 (J/mm^3). However, spatter particles were observed on the surfaces of cubes 1 – 3 at VEDs above 70.8 (J/mm^3). Since spatter occurs due to recoil pressure from metallic vapor overcoming the surface tension of a molten pool [2,92], it is possible that the sensitivity to high VED in AF9628 is due to the relatively low surface tension of molten low alloy steels compared to other alloying systems common to additive manufacturing [93,94]. For example, the surface tension at melting temperature of Inconel 718LC is 1.85 (N/m) [94], tooling steel is 1.73 (N/m) [94], and AISI 304 stainless steel is 1.40 (N/m) [93] as compared to 1.29 (N/m) for AISI 4142 low alloy steel [93]. This puts a minimum limitation on the range of hatch spacing values that can be chosen for a specific parameter set.

Microstructural Evolution

During SLM, a high intensity laser scans the AF9628 powder, melting the powder and penetrating the surface beneath. During solidification, grains tend to grow epitaxially and towards the steepest temperature gradient (typically towards the center of the molten pool) [5]. As the laser travels along the substrate, layers below the molten pool can be affected by the heating and cooling. This affected area is called the heat affected zone (HAZ) [59], similar to classical welding literature, and is clearly visible in the single track experiments shown in Figure 2b. Across the HAZ, a variety of stable and metastable phases exist in low alloy steels [67]. There are sections of the heat affected zone that undergo different microstructural changes. The zone closest to the melt pool will reach temperatures near the melting point of AF9628 and be above the austenitization temperature. In this region, the material can undergo solid state phase transformations during the

laser pass to and from austenite during heating and cooling. Further away from the melt pool, the material can experience high temperatures below the critical temperature. In these regions, any existing martensite will undergo auto-tempering, or softening due to carbon diffusion out of the supersaturated martensite causing carbides to form [23].

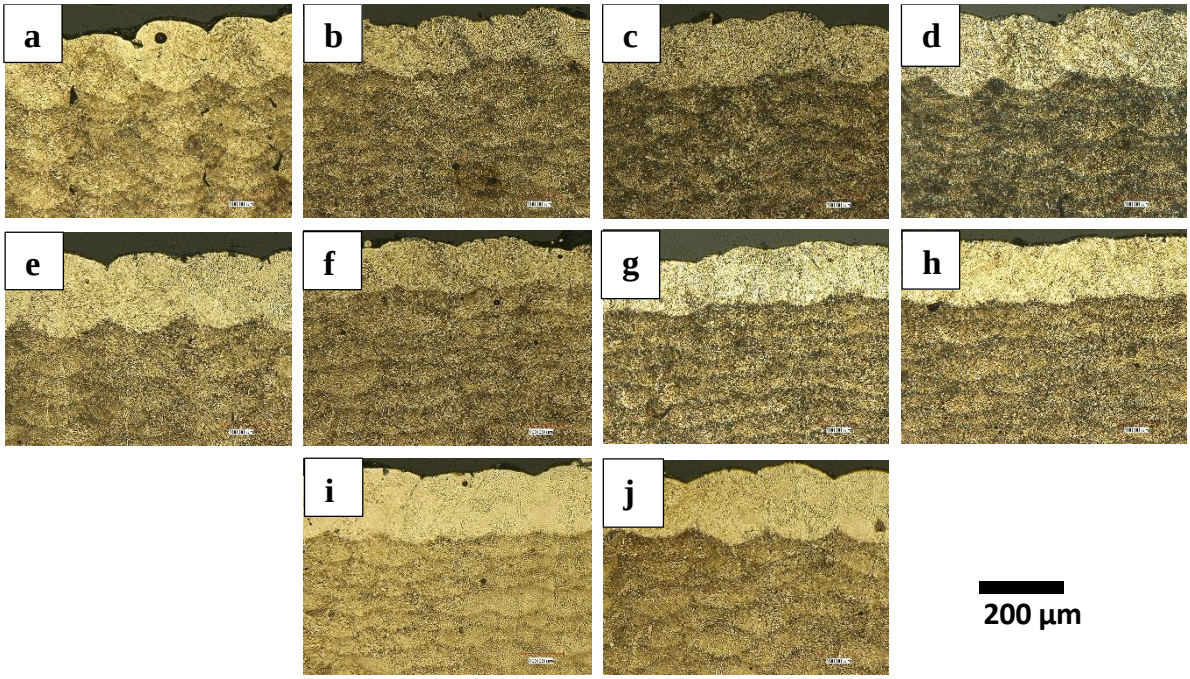

Figure 14. Etched optical micrographs of the cross-sections of AF9628 ultra-high strength martensitic steel as-printed cubes. (a) through (j) are the images from the Cubes 4 through 13 listed in Table 2, respectively.

Figures 14a – 14j display etched optical micrographs of cubes 4 – 13. A stark contrast is clearly observable between the top most layer of each cube and the layers below. This is a direct consequence of the heating cycles that temper the preceding layers of the part. The top most layer has not undergone heat treatment from above layers, and is therefore tempered to a lesser extent. Dilip et al. [23] reported higher hardness values in untempered regions of SLM HY100 steel

compared to auto-tempered regions. Similarly, bright and dark regions can be observed within a single layer, representing the different areas of the HAZ: the austenitization and auto-tempering zones from top to bottom, respectively. The auto-tempered regions within a single layer appear thin and dark whereas austenitized zones appear larger and bright, similarly to what was previously reported [23]. The optical micrographs reveal that the cubes have different melt pool morphologies. Cubes 9-12 (Figures 14f – 14i) appear to have a layered melt pool morphology. In contrast, cubes 4 – 8 and 13 (Figures 14a – 14e and 14j) have more clearly defined circular melt pool – HAZ regions.

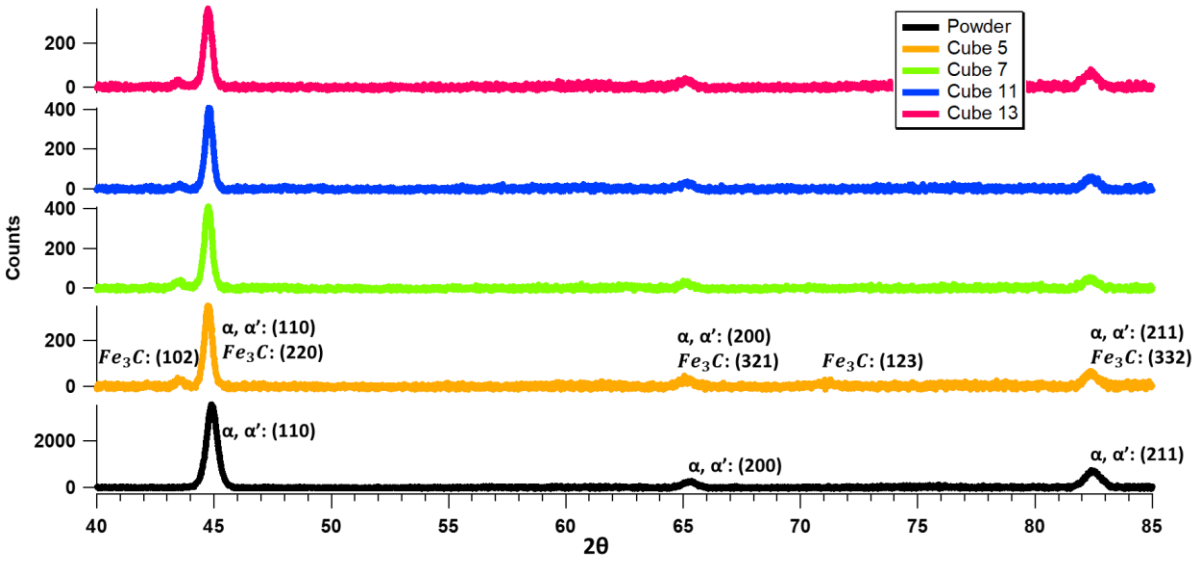

Figure 15. X-Ray Diffraction spectra of AF9628 ultra-high strength martensitic steel powder and as-printed cubes 5, 7, 11, and 13 listed in Table 2.

Phase analysis of the powder and as-printed AF9628 cubes was conducted using X-ray Diffraction (XRD). XRD was conducted on cubes 4-13, however, only the cubes selected for tensile testing (cubes 5, 7, 11, and 13) and the powder are displayed in Figure 15. AF9628 in the

powder condition displayed peaks at 44.9°, 65.3°, and 82.5° which closely match the characteristic spectra of martensite and α-ferrite. Since these peaks also overlap with cementite (Fe_3C), further phase analysis is required to determine the existence and relative amounts of these three phases. However, a martensitic lath dominated structure was observed in SEM micrographs of the AF9628 powder (Figure 10), as discussed in section 3.1. As-printed cubes displayed the same peaks as the powder, as well as an additional peak at 43.5°. Cube 5 was the only specimen that displayed a small peak at 71.1°, in addition to the aforementioned peaks. Both the peaks at 43.5° and 71.1° match closely to cementite (Fe_3C). Since typical cooling rates in the SLM process are $10^4 – 10^6$ (K/s) [5], well above the critical cooling rate for martensite in low carbon steels, these results indicate that reheating and auto-tempering cycles cause the formation of cementite in as-printed AF9628. Figure 16 presents SEM micrographs of the etched cross sections of the AF9628 in the as-printed condition, and show complex microstructural features. Melt pools are outlined in yellow dotted lines, and martensitic laths are observed to cross over the melt pool boundaries. Regions outside the martensite laths show cellular structures which are possible artifacts of the solidification process. White nano-scale precipitates are also observed within the laths of martensite. Dilip et al. [23] suggested that these fine white precipitates were carbides, however, this was not verified in their study. Further phase analysis is needed in order to conclusively determine the phases that are observed in this study, utilizing transmission electron microscopy.

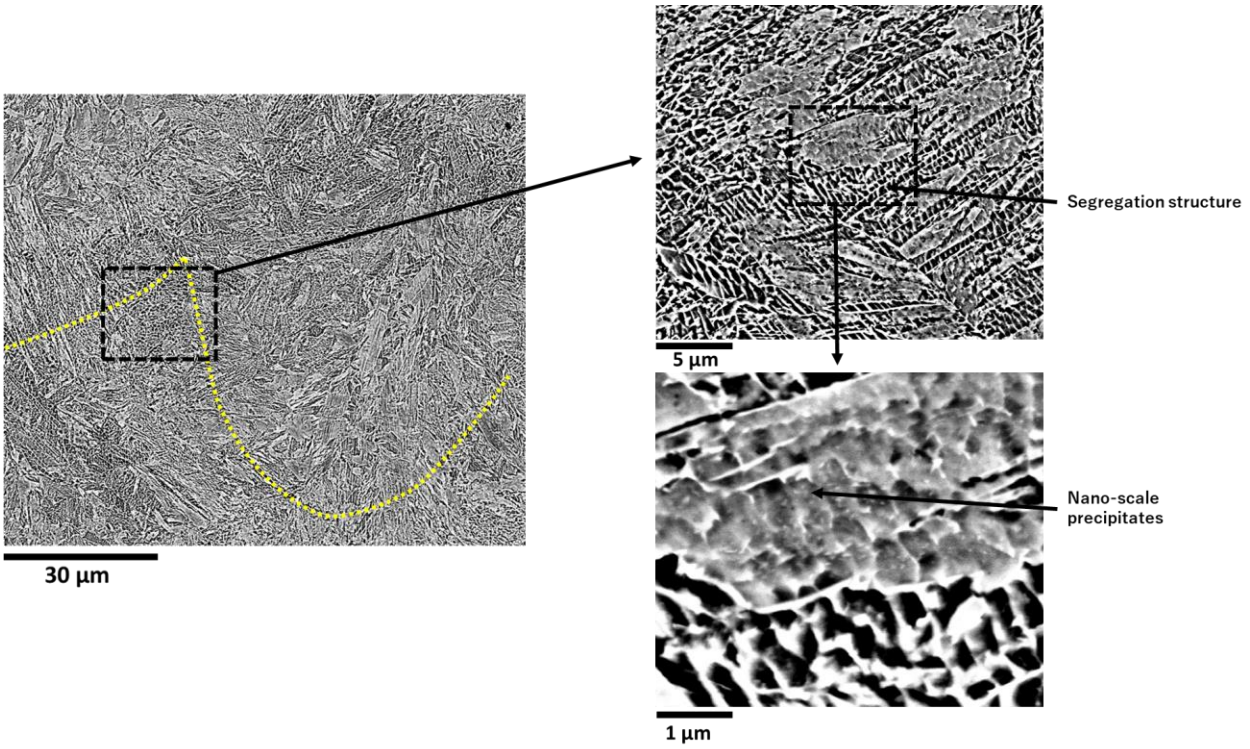

Figure 16. Scanning electron microscopy, backscattered electron images of the etched cross-sections of AF9628 ultra-high strength martensitic steel as-printed cubes. The yellow dotted lines indicate melt pool boundaries.

Electron backscattered diffraction imaging was conducted on cubes 4 – 13, all of which exhibited similar microstructural features. Figure 17a displays a representative EBSD inverse pole figure (IPF) map taken from the middle of the vertical cross section of cube 11. The IPF map reveals the martensitic microstructure in the as-printed specimen. Thin and dark auto-tempered regions (indicated by yellow dotted lines and yellow arrows) are observable under large austenitization zones (indicated by white dotted arrows), consistent with the etched microstructures in Figure 14. The auto-tempered regions appear to contain smaller grains than the austenitization zones. The IPF in Figure 17b reveals that the martensitic microstructure is weakly

textured and oriented along the [001] direction. Grain size distribution in cube 11 is presented in Figure 17c. Martensitic laths have an average equivalent diameter of 6.3 ± 1.5 µm. Average lath size between cubes 4 – 13 is similar, ranging between 4.0 – 6.3 µm.

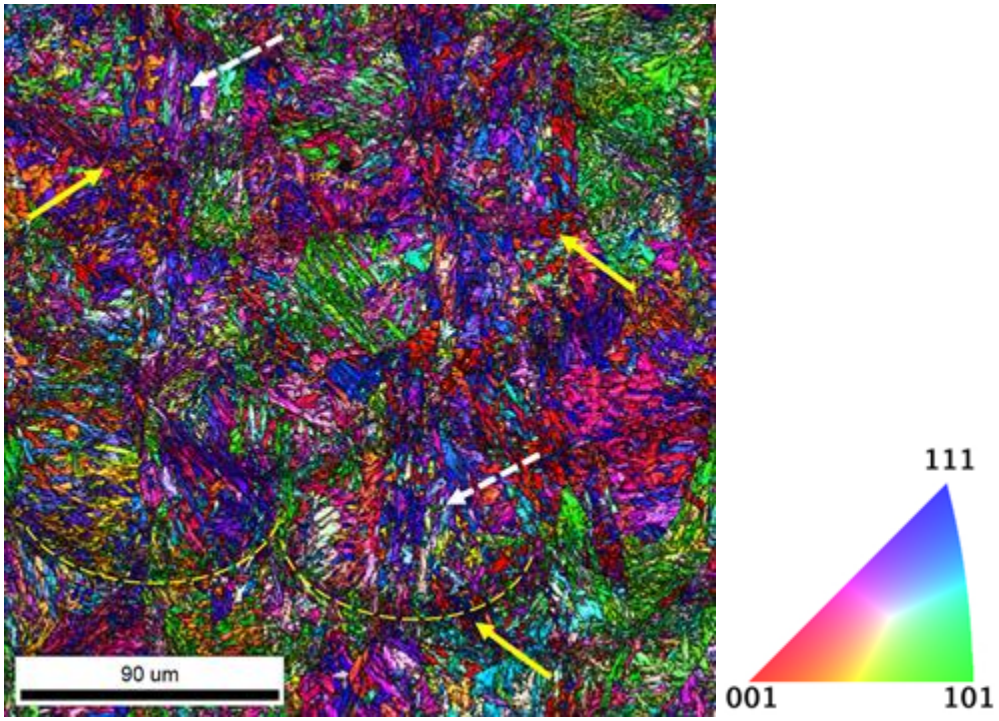

(a)

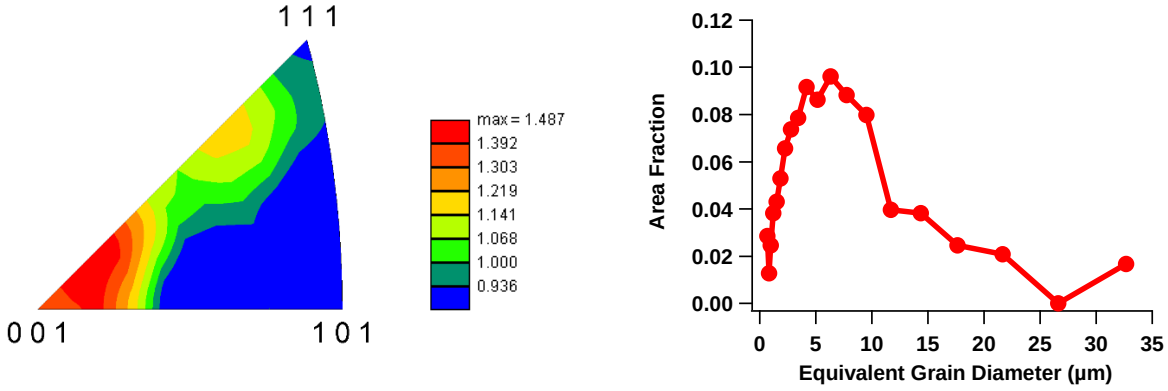

(b) (c)

Figure 17. A representative electron backscattered diffraction image of an AF9628 ultra-high strength martensitic steel as-printed cube and the corresponding data collected from the middle of

the vertical cross section of cube 11 (see Table 2). (a) An inverse pole figure map revealing the martensitic microstructure in the as-printed specimen. Thin and dark auto-tempered regions (indicated by yellow dotted lines and yellow arrows) are observable under large austenitization zones (indicated by white dotted lines). (b) An inverse pole figure revealing a weakly textured microstructure in the scanned area of the specimen. (c) Equivalent martensite grain diameter area fraction distribution in the scanned area of the IPF map.

Mechanical Properties Under Tension

Four parameter sets were selected for tension testing based on the cubes with density > 99% (cubes 5, 7, 11, and 13) to represent the different regions of the processing map. Tensile testing was performed on as-printed AF9628 specimens built in the horizontal and vertical directions with respect to the building direction. Two to three companion specimens were tested in each case and the average mechanical property values are listed in Table 3. Representative stress-strain curves of the as-printed specimens are displayed in Figures 18a and 18b, along vertical and horizontal directions, respectively. Interestingly, yield strengths (YS) are relatively consistent (1.04 – 1.11 GPa) for all specimens regardless of processing parameters and orientations in the selected set. Ultimate tensile strength (UTS) is also consistent (1.31 – 1.43 GPa) between different process parameter sets (P, V, and h) in the same build orientation. However, the specimens printed in the horizontal direction showed greater UTSs than those printed in the vertical direction. Reasonable tensile ductility levels are observed in the as-printed specimens (7.4 – 10.9% elongation). The observation of consistent mechanical property data with small variance, for samples printed with different laser power and speed combinations in the optimized processing region, points to the possibility that with the proper selection of hatch spacing, it might be possible to reduce the

variability of mechanical properties of 3-D printed metallic materials and achieve consistent mechanical properties for a given alloy system.

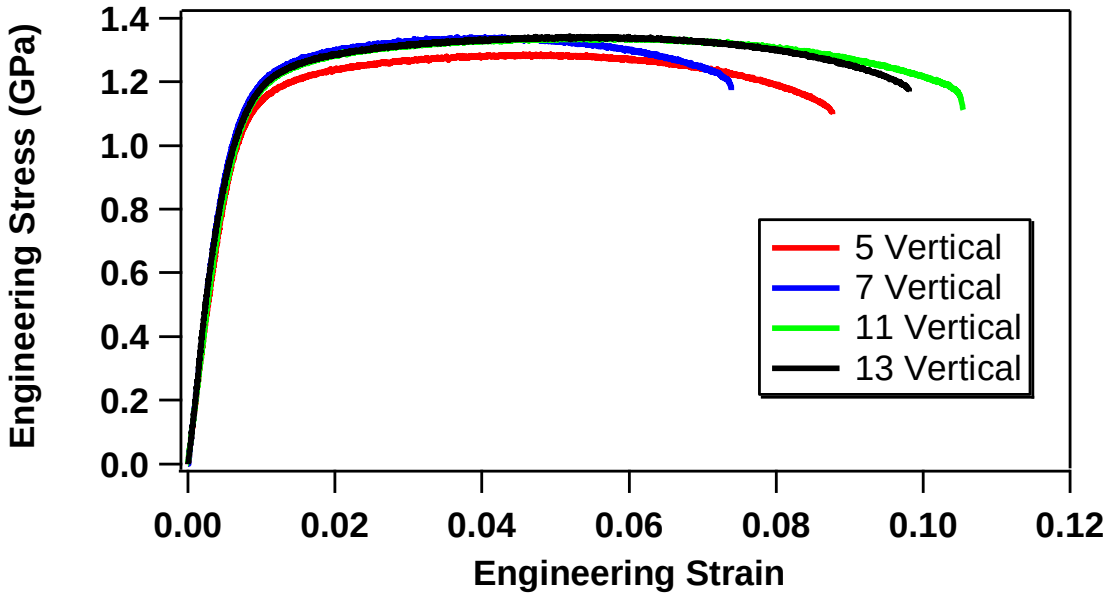

(a)

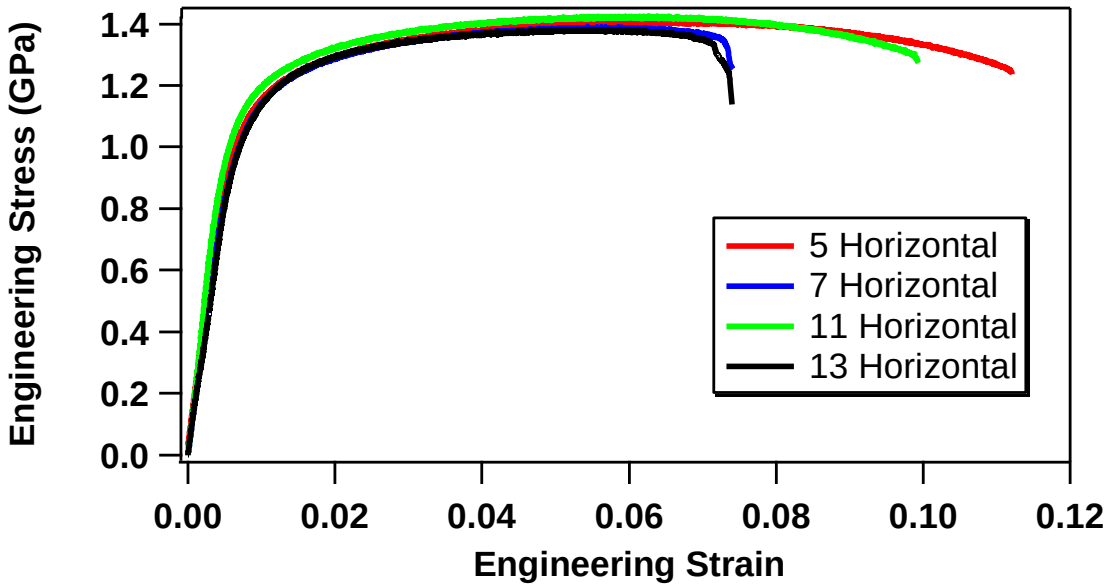

(b)

Figure 18. Representative stress-strain curves of the as-printed AF9628 ultra-high strength martensitic steel specimens 5, 7, 11, and 13. (a) Tested in the vertical direction with respect to

the building direction. (b) Tested in the horizontal direction with respect to the building direction. Refer to Table 2 for the corresponding processing parameters.

Of all the specimens, parameter set 11 showed the best tensile ductility in the vertical direction (10.9% elongation), and excellent ductility in the horizontal direction (9.8% elongation). Improved elongation in parameter set 11 can be correlated with the porosity values measured in Figure 13. Cube 11 was measured to have the lowest porosity (0.06%) of all parameter sets. Cubes 7 and 13 showed the highest porosity (0.25% and 0.40% respectively) of the tension specimens in OM images. This can explain the relatively early fracture of tensile specimens printed horizontally with these parameters. As discussed earlier, cube microstructures display alternating layers of tempered and untempered regions. These regions contribute to the improved elongation in vertically printed specimens compared to those printed horizontally [23], as observed in parameter set 11.

Microstructure and Phase Diagram Feature Effects in Ni-based Alloys

Powder Characterization

Surface morphology and cross sectional microstructure of the gas atomized Ni-5at.% Al (NiAl), Ni-20at.% Cu (NiCu), Ni-5at.% Zr (Ni-5Zr), and Ni-8.8at.% Zr (Ni-8.8Zr) powders are displayed in Figure 19. Microdendritic features are directly observable on the surfaces of the NiCu and Ni-5Zr powder particles. Grain boundaries are similarly observed on the surfaces of the NiCu and NiAl powder. Cross sections of the Ni-5Zr powder revealed white segregation structures, whereas grain structures are observed in the NiCu and NiAl cross sections. NiCu powder particles may contain Cu segregation, however, the similarity in atomic number between Ni and Cu may result in poor contrast in the backscattered electron micrograph between regions of Cu segregation

and the matrix. The Ni-8.8Zr eutectic powder displays a fine lamellar microstructure characteristic of eutectic alloys subjected to high solidification rates [79,80]. These results indicate the dependence of solidification microstructures on the solidification range of each alloy. The clear microsegregation observed in Ni-5Zr is likely due to the large solidification range and low k_e of the alloy (172 K and 0.11, respectively). On the other hand, no segregation of Al is present in the NiAl alloy due to its small freezing range and k_e value (0.2 K and 0.96, respectively). The larger freezing range allows time for solute rejection from the matrix phase during solidification. This results in the observed cellular-dendritic structures in the powder particles.

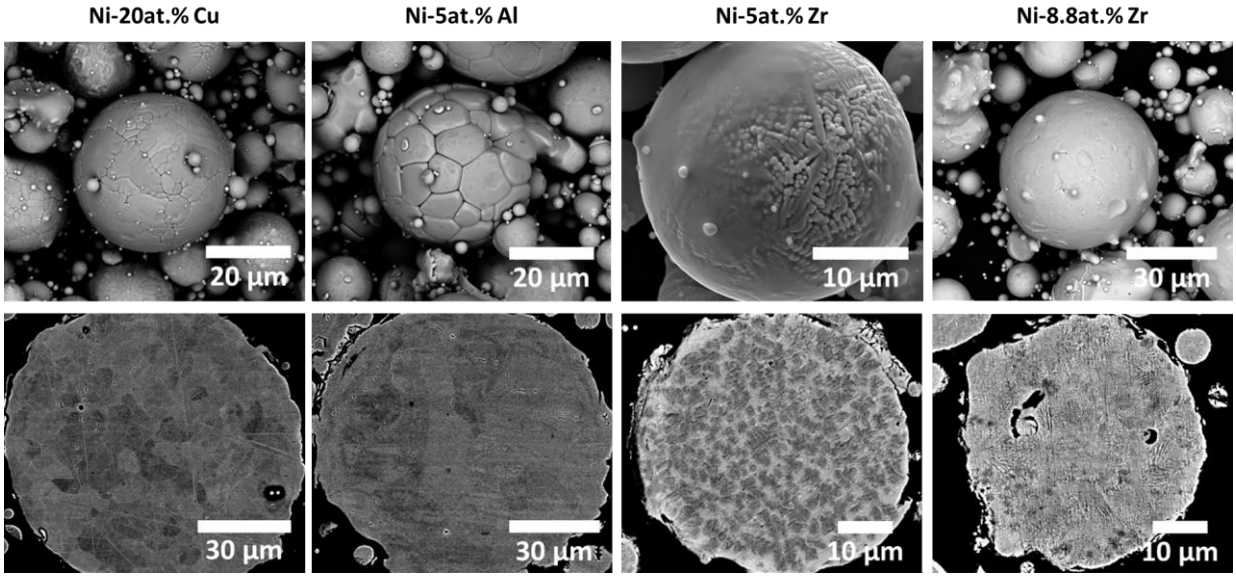

Figure 19. Scanning electron microscope images of gas atomized Ni-20at.% Cu, Ni-5at.% Al, Ni-5at.% Zr, and Ni-8.8at.% Zr powder particle morphology is displayed in the first row of micrographs and cross sections of these particles are displayed in the second row of micrographs.

Process Parameter Optimization for Ni-based Alloys

Single tracks were selected based on the process parameter optimization framework discussed in Section 2.1. Forty-six single track experiments were sampled with a grid-based sampling

strategy throughout the parameter space and are displayed as markers on the plots in Figure 20. Boundaries of the laser power (P) – scan speed (v) sampling space were selected as (P_{min}, P_{max}) = {71, 260 W} and (v_{min}, v_{max}) = {0.05, 2.5 m/s}. Values for P_{max} and v_{max} were set to the machine limitations, and v_{min} was selected to avoid prohibitively slow scan speeds. P_{min} was selected as the lowest power necessary to attain a melt pool depth equal to one layer thickness at v_{min} in the alloy with the largest melting temperature (Ni-5at.% Al) as predicted by the E-T model. The parameter space was then split into two regions for grid-based single track sampling. Thirty single tracks were sampled between v_{min} = 0.05 m/s and v = 1.3 m/s, and the remaining 16 single tracks were sampled between v = 1.3 m/s and v_{max} = 2.5 m/s. The first region was sampled more densely as it is expected to contain most of the optimal printability regions for all alloy systems. Keyholing and balling single tracks were classified qualitatively based on top-view and cross sectional micrographs based on the characteristic features of these defect mechanisms [2,21,29,46,90]. Previous studies have classified lack of fusion single tracks using a melt pool depth = layer thickness criteria [21,46,95]. However, Zhang et al. [95] reported that high density prints can still be achieved within this lack of fusion region, demonstrating the need to relax this constraint. Since a single track lack of fusion criterion is somewhat arbitrary due to the necessity of printing multiple single tracks and at least few layers to form lack of fusion porosity, a less conservative value is selected to expand the functional printability region. Lack of fusion single tracks were classified based on the experimental measurements and a criterion of melt pool depth $\leq$ 0.667 × layer thickness ($D \leq 0.667t$). This value is selected as the minimum single track depth required to penetrate the solid printed substrate after 10 layers, based on the assumptions that the effective height of a layer printed on the substrate is equal to the powder packing density × the layer thickness and that the relative powder packing density is ~60%.

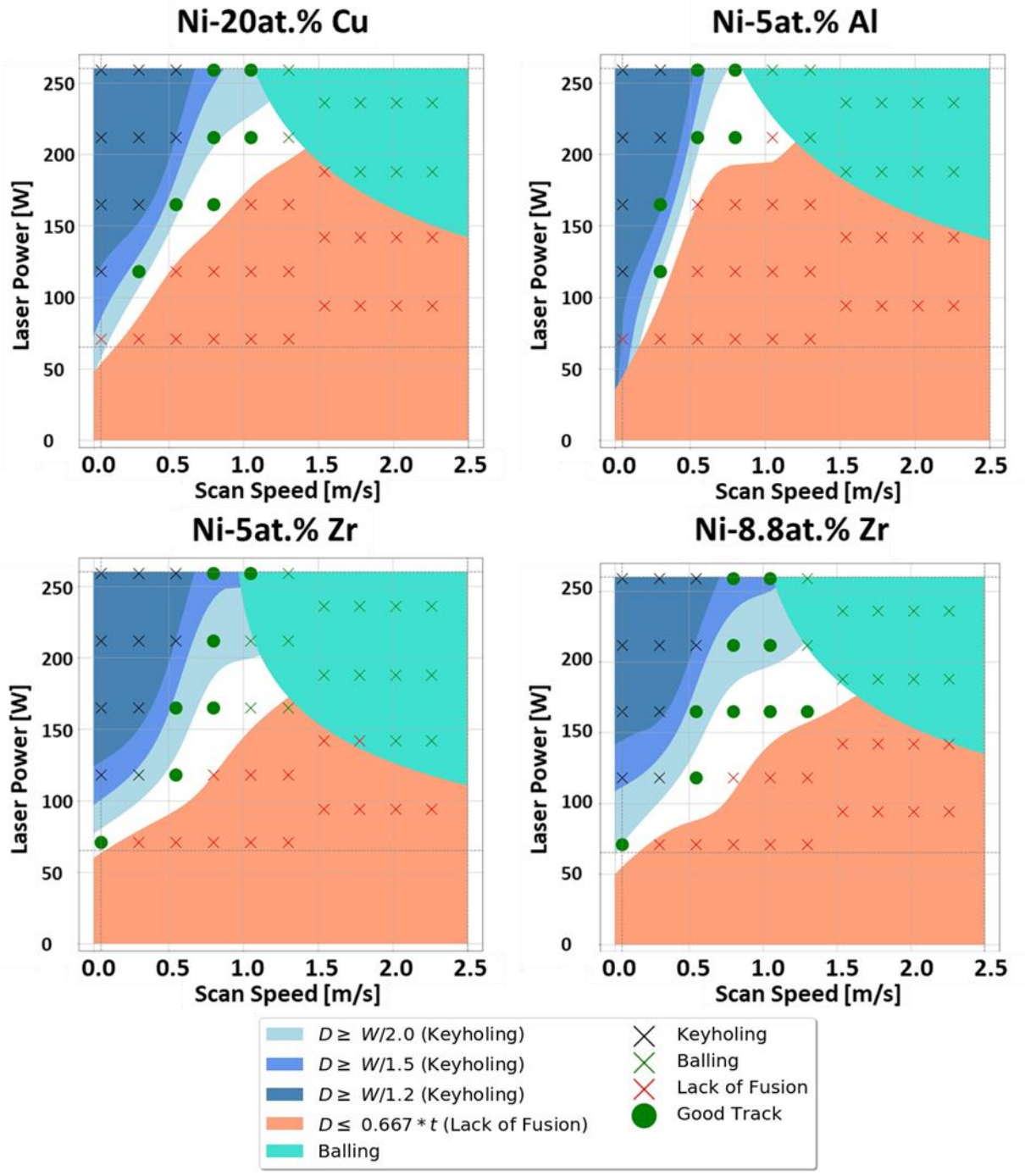

Figure 20. L-PBF process parameter maps are displayed for Ni-20at.% Cu, Ni-5at.% Al, Ni-5at.% Zr, and Ni-8.8at.% Zr. These maps contain various keyholing criteria ($W/D \leq 1.2$, 1.5, 2.0) to determine which criterion fits best, and a lack of fusion criterion ($D \leq 0.667$t), predicted by the calibrated Eagar – Tsai (ET) model. A balling region fit to single track experiments using

a Support Vector Machine (SVM) classifier is also plotted. Experimentally classified single-tracks exhibiting keyholing, lack of fusion, balling, and good track characteristics are marked with different symbols and colors in these maps demonstrating good match with ET model predictions. *D*: Melt Pool Depth, *W*: Melt Pool Width, *t*: Powder Layer Thickness.

The statistical methodology described in Section 2.1.3. was used to calibrate the Eagar-Tsai model to single track experiments. Melt pool dimension predictions from the fully calibrated model are then used to establish the lack of fusion and keyholing boundaries displayed in Figure 20. Potential defect boundaries are selected based on melt pool dimension relationships that have been observed to correspond well with defect formation, namely, a melt pool width/depth relationship (W/D) to determine keyholing and a melt pool depth/layer thickness (D/t) relationship to determine lack of fusion boundaries [21,32,46,47,74]. Several keyhole criteria are plotted and compared to experimentally characterized single tracks in Figure 20 to visualize which boundary best fits each material based on the experimental observations. The keyholing criteria selected for comparison were chosen based on values established in the literature ($W/D \leq 1.2$, 1.5, 2.0) [21], and the lack of fusion criterion was selected as $D/t \leq 0.667$. A defect boundary for balling was established using a support vector machine classifier (SVM) [96] that uses experimental single track classifications to divide the processing map into balling and non-balling regions. A 3rd degree polynomial kernel SVM classifier [97] was used to determine the balling region of each material. Once these defect criteria are established, finalized processing maps can be created for each alloy. It should be noted that the methodology described for building processing maps in this work is intended to be AM machine specific, as single tracks built in different machines may display differences in melt pool morphologies.

To ensure proper fusion between melt pools, the geometrically-based hatch spacing criterion described in Section 2.1.4. is implemented [21]. This equation was used to plot maximum hatch spacing contours on finalized processing maps for each alloy, as displayed in Figure 21. Three parameter sets were selected from each alloy at different locations in the parameter space to print 8×8×8 mm cubes based on the processing maps in Figure 21. Hatch spacing values selected to print the cubes were rounded down to the nearest multiple of five. The parameters chosen for each of these cubes is listed in Table 4.

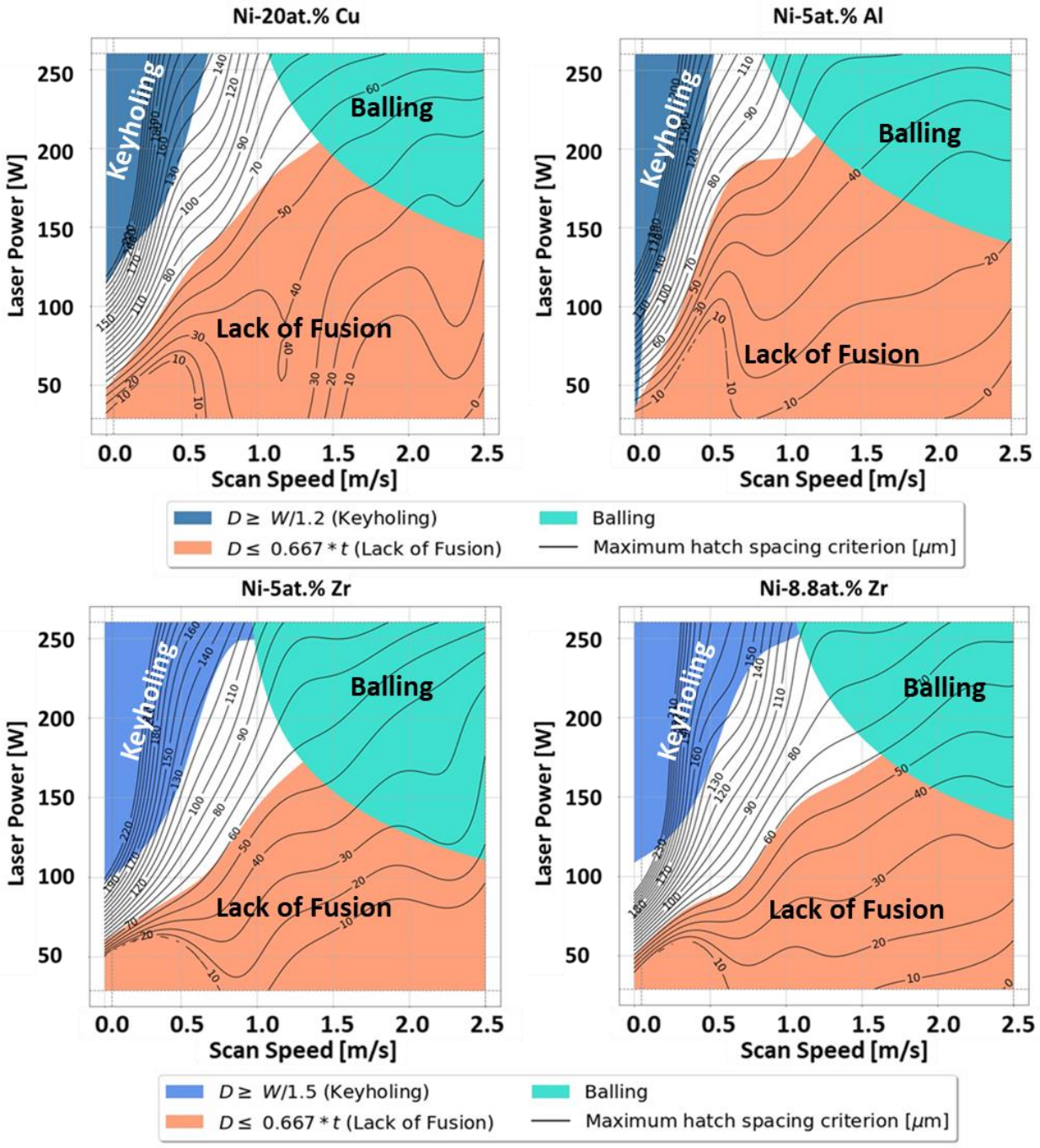

Figure 21. L-PBF process parameter maps with finalized selections of keyholing criteria and maximum hatch spacing contours. The keyholing criterion selected for Ni-20at.% Cu and Ni-5at.% Al is $W/D \leq 1.2$, and $W/D \leq 1.5$ for Ni-5at.% Zr and Ni-8.8at.% Zr. Lack of fusion criteria is kept at $D \leq 0.667t$ for all maps, and the balling region was fit to single track experimental data

using a Support Vector Machine (SVM) classifier. *D*: Melt Pool Depth, *W*: Melt Pool Width, *t*: Powder Layer Thickness, h_{max}: Maximum Hatch Spacing

Table 4. A list of the processing parameters selected to print 8 × 8 × 8 mm cubes for the Ni-based alloys selected for microstructural analysis within the optimal process parameter regions of the processing maps in Figure 21.

Alloy Composition	Laser Power (W)	Scan Speed (m/s)	Hatch Spacing (µm)	Layer Thickness (µm)
Ni-20at.% Cu	115	0.05	200	49
	120	0.30	110	
	225	0.90	100	
Ni-5at.% Al	100	0.05	130	
	125	0.30	85	
	240	0.90	85	
Ni-5at.% Zr	75	0.05	120	
	110	0.30	125	
	140	0.90	60	
Ni-8.8at.% Zr	80	0.05	165	
	120	0.30	160	
	130	0.90	60	

Comparing Single Track Dimensions and Printability Across Alloy Systems

Two laser heating modes influence melt pool geometry: conduction mode and keyhole mode heating. Conduction mode melting occurs at low energy densities and is characterized by a wide and shallow melt pool, whereas keyholing occurs at high energy densities and is characterized by deep melt pools. The optical micrographs in Figure 22 reveal a clear trend from conduction to keyhole mode heating as the linear energy density (LED = $\frac{P}{v}$) increases from left to right in each alloy (147.5 J/m, 300 J/m, 5180 J/m respectively). The contrast between single tracks printed at the same parameters is easily observed in Figure 22, and a correlation between alloy liquidus temperature and melt pool dimensions can be seen. NiAl has the highest melting temperature (1417 ˚C) of the four alloys and appears to have the smallest melt pools at each parameter set. In comparison, Ni-8.8Zr displays the largest observable melt pools and has the lowest melting temperature (1167 ˚C). At the LED of 300 J/m, NiCu, Ni-5Zr, and Ni-8.8Zr show mixed conduction – keyhole mode melting whereas NiAl displays a melt pool morphology indicative of conduction mode melting. This relationship between melt pool dimensions and alloy melting temperature is more clearly demonstrated in Figure 23, which displays distinct trends in melt pool width (Figure 23a) and depth (Figure 23b) for each material. Both the width and depth of the single tracks appear to be dependent on the melting temperature of each alloy. For both width and depth, the order of materials from smallest to largest melt pools and highest to lowest melting temperatures is: NiAl (1417 ˚C), NiCu (1377 ˚C), Ni-5Zr (1327 ˚C), and Ni-8.8Zr (1167 ˚C). These results are intuitive, as alloys that require less energy to melt would be expected to undergo more melting when exposed to the same level of energy. However, it is interesting to note that despite the large difference in melting temperature (up to 285 K for NiAl and Ni-8.8Zr), many of the single

tracks are within one standard deviation of each other in both width and depth at each parameter set. The largest differences in melt pool dimensions between alloys occur at LEDs above 1000 J/m.

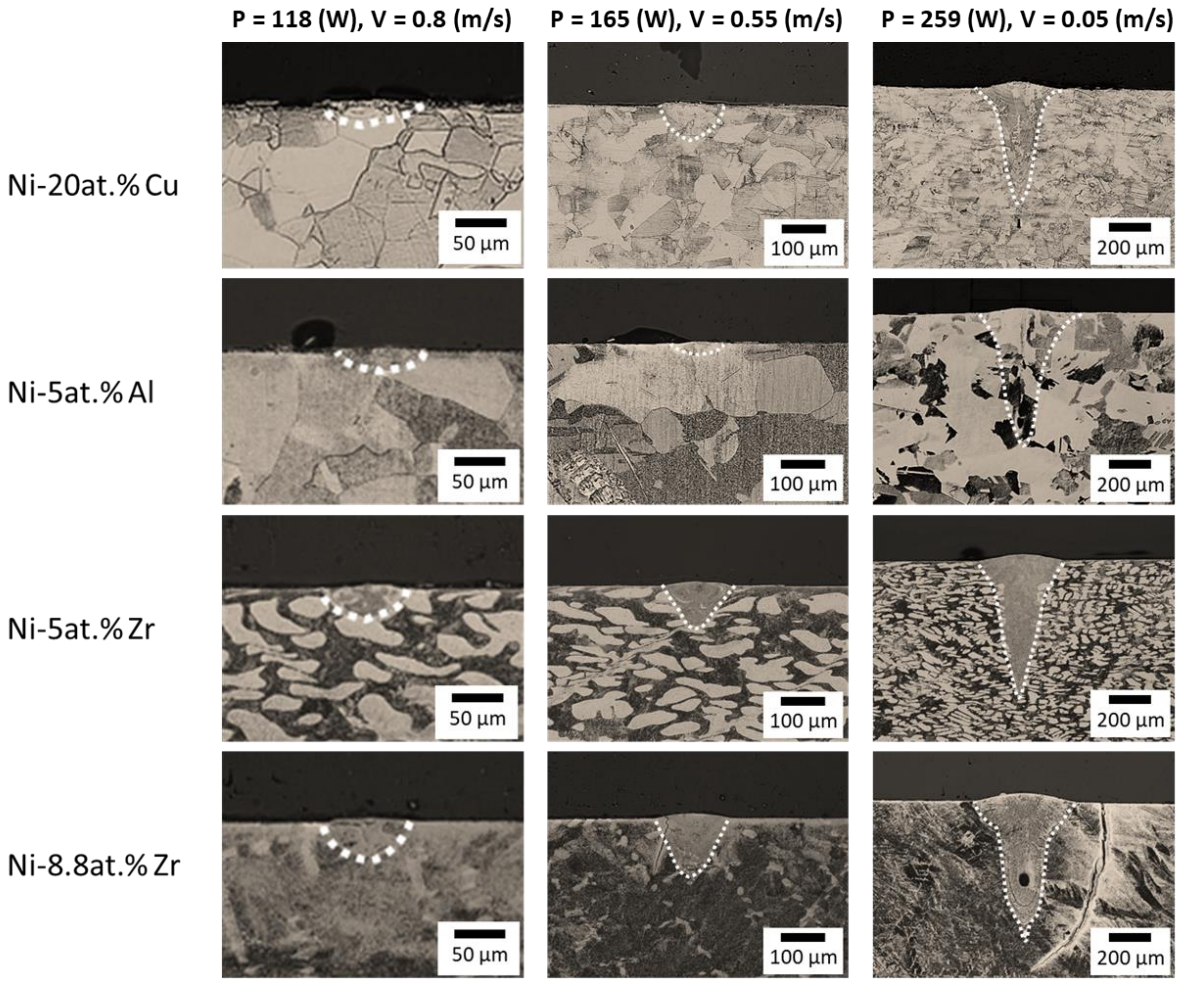

Figure 22. Optical micrographs of cross sections of single tracks printed at three different parameter sets for each of the alloys printed in this study: *P*: 118 W, *v*: 0.8 m/s; *P*: 165 W, *v*: 0.55 m/s; and *P*: 259 W, *v*: 0.05 m/s. White dotted lines indicate the boundaries of single tracks that are difficult to distinguish in these images. These single tracks demonstrate a transition between conduction mode heating and keyholing in L-PBF.

These melt pool dimension variations can explain the differences in the identified optimal printing region between each alloy's processing map displayed in Figure 21. NiAl is observed to have the smallest printable region out of the four alloys due to the large lack of fusion region. Since the lack of fusion region criterion is based on predicted melt pool depth, NiAl's higher melting temperature and shallower melt pools result in a larger lack of fusion region compared to the other alloys. The lack of fusion boundaries for all four alloys follow a similar trend as the melt pool dimensions. Alloys with larger melting temperatures display larger lack of fusion regions. However, the opposite appears to be true of keyholing boundaries in these alloys. Ni-5Zr and Ni-8.8Zr display larger keyholing regions compared to the NiCu and NiAl alloys. This is in part due to the difference in keyholing criteria selected for these maps; NiCu and NiAl have a keyholing criterion of $W/D \leq 1.2$, whereas Ni-5Zr and Ni-8.8Zr have a keyholing criterion of $W/D \leq 1.5$. However, these criteria were selected based on experimental observations of single tracks in these regions. Single tracks in the two Ni-Zr alloys were observed to display keyholing at lower laser powers than those in NiCu and NiAl. This is also likely to be attributable to melting temperature. Lower melting temperatures reduce the energy barrier for melting resulting in deeper melt pools, as is observed in Figure 23b. It appears that the lack of fusion boundary is more sensitive to this effect than the keyholing boundary, since the printable region for each of the alloys gets larger at lower melting temperatures.

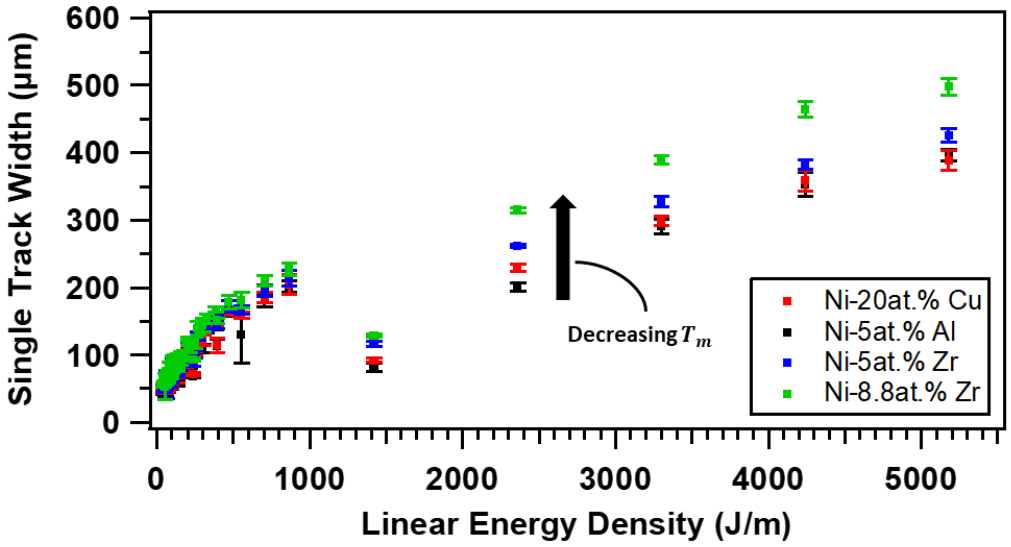

(a)

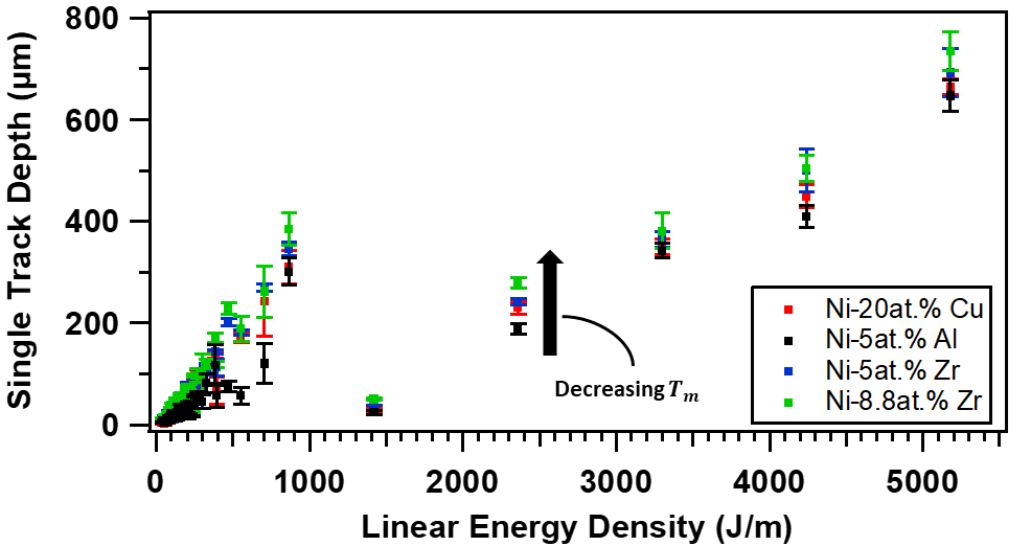

(b)

Figure 23. Plots of measured single-track melt pool dimensions against linear energy density: a) is a plot of the observed single-track widths for each material and b) is a plot of the observed single-track depths for each material. Error bars display 1 standard deviation away from the mean in each direction. The black arrows indicate that alloys displaying larger melt pool dimensions have lower melting temperatures (T_m).

Comparing Single Track Microstructure Across Alloy Systems

Composition analysis of the single tracks at several parameter sets was conducted using quantitative WDS measurements. Figure 24 displays optical micrographs and WDS maps taken from the largest energy density parameter set (P= 259 W, v = 0.05 m/s, and LED = 5180 J/m) used to print single tracks for each alloy. Figure 24 displays optical micrographs of the single tracks in the left column with red and blue boxes indicating WDS map locations. The middle column of Figure 24 shows WDS maps taken from the top of each melt pool, and the right column shows maps taken from the edges of each melt pool. Differences in segregation structure are easily observable in WDS maps at the top of each melt pool. NiCu displays notable cellular structures in both the top and the edge of the melt pool. Up to 5 at.% additional segregation of Cu is observed in the WDS map at the top location of the melt pool. NiAl and Ni-8.8Zr display completely homogenous microstructures, showing no compositional segregation at the top of the melt pools. This is likely due to the small solidification ranges in NiAl and Ni-8.8Zr (0.2 K and 0 K respectively). Even lamellar structures are not observable in WDS maps of the eutectic Ni-8.8Zr alloy. This may be due to the extremely high cooling rates associated with the additive manufacturing process, which may result in nanoscale lamellar solidification too fine to be detected by the instrument. Ni-5Zr displays large dendrite structures at the top of the melt pool. These structures appear to have primary and secondary dendrite arms with up to 6 at.% additional segregation of Zr. Large dendrite structures have time to form during solidification of the Ni-5Zr alloy due to the large solidification range of the material (172 K).

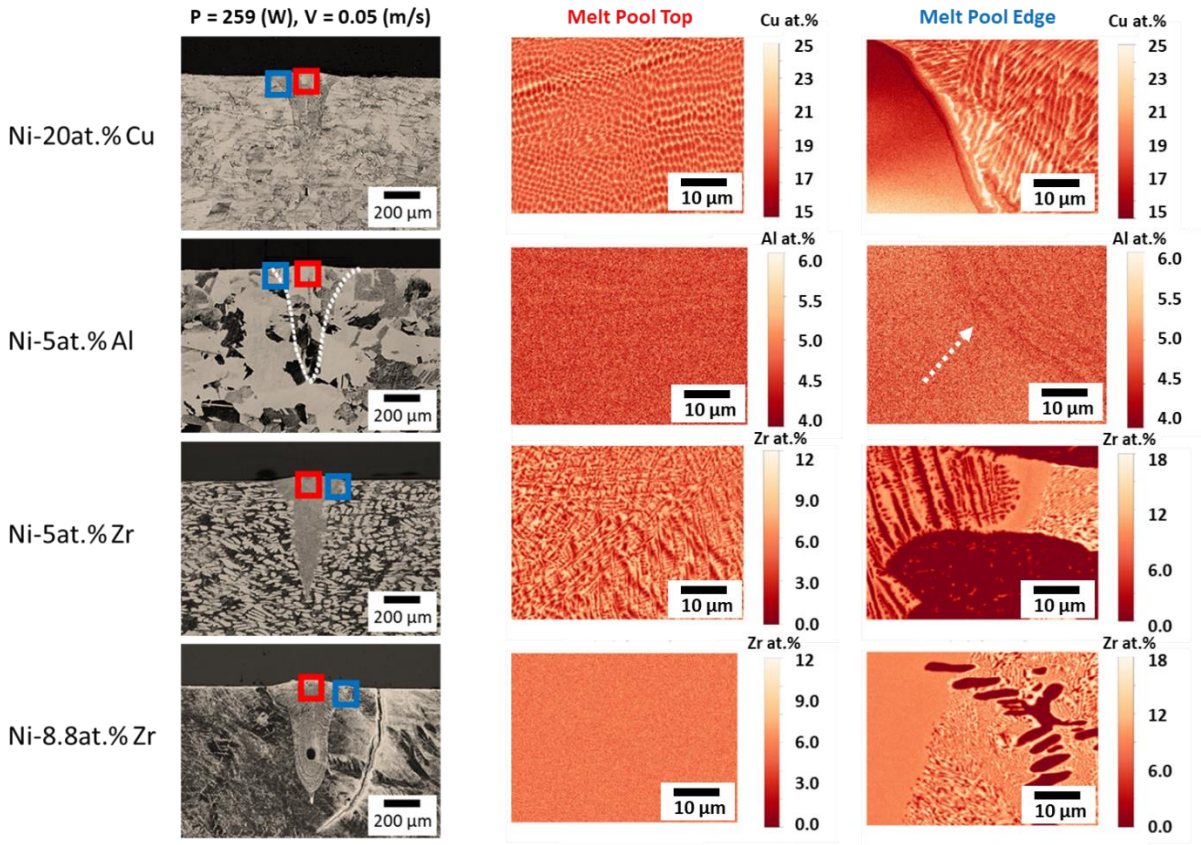

Figure 24. Optical micrographs of single tracks for each alloying composition printed at 259 W and 0.05 m/s are displayed in the left column with red and blue boxes indicating where WDS maps were conducted. The middle column shows WDS maps taken from the top of each melt pool, and the right column shows maps taken from the edges of each melt pool as color coded in the optical micrographs. White dotted lines indicate the boundaries of single tracks that are difficult to distinguish in these images. The white dotted arrow indicates the edge of the NiAl single track.

Single-track fusion boundaries are observable in the WDS maps taken at the edges of each melt pool (Figure 24). Around 4 at.% Cu depletion is observed at the fusion boundary of the NiCu single track, along with columnar segregation structures inside the melt pool. This Cu depletion is

indicative of a transient at the fusion boundary as the solidification grows by accelerating from zero velocity. Low growth rates during solidification can explain the appearance of planar structures near the fusion boundary. Solidification starts at the fusion boundary once the material drops below the liquidus temperature. The planar structure at the fusion boundary transitions to a columnar segregation structure as the temperature drops below the liquidus and the growth rate surpasses the constitutional supercooling limit. The microstructure differs greatly at each location of the melt pool in NiCu, showing cellular segregation at the top and columnar segregation at the edge. This is due to variation in thermal conditions and growth velocities at different locations along the solidification front. However, the cell structures at the top of the NiCu melt pool display similar sizes, which suggests that the cells are in a steady-state condition at that location. NiAl similarly displays Al depletion at the melt pool boundary. However, the solute Al atoms have far less time to segregate out of the matrix due to the lower solidification range ($\Delta \boldsymbol{T}$) and the effect is much smaller than in NiCu (< 1 at.% depletion). Ni-5Zr displays a large homogenous region along the melt pool boundary and Zr depleted dendrite structures inside the melt pool at the edge location. This may indicate the opposite effect of those observed in NiCu and NiAl, where Zr segregates at the melt pool boundary enough to solidify as a eutectic. It is also possible that mixing between the molten pool and the observed local Ni_5Zr phases in the base plate caused a local increase of Zr during the laser scan. This would explain the compositional homogeneity observed along the melt pool boundary in Ni-5Zr, which is very similar to what is observed at the top of the eutectic Ni-8.8Zr single track. The Ni-8.8Zr alloy displays an immediate transition between the molten pool and the eutectic base plate, with no Zr depletion observed. The complete homogeneity within the Ni-8.8Zr melt pool indicates how critical the freezing range of an alloy is to microstructure in additively manufactured materials.

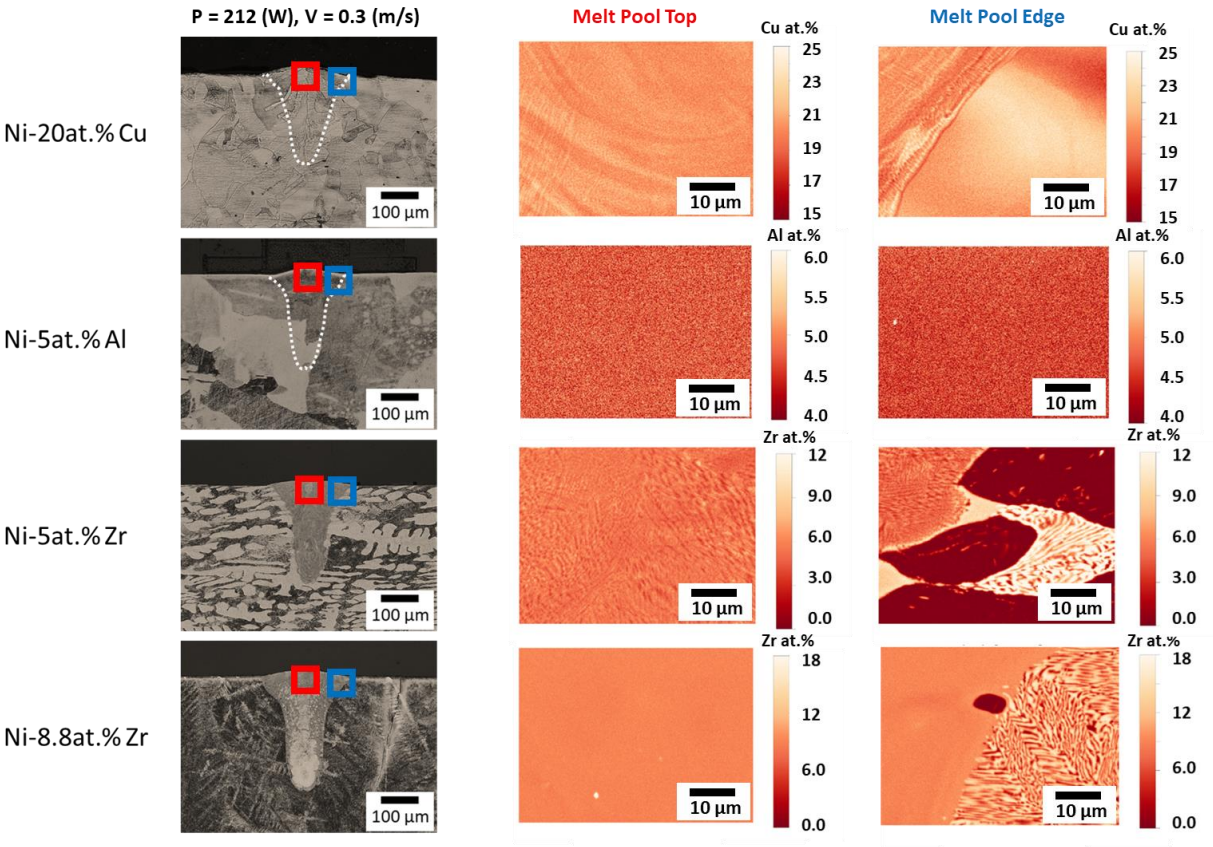

Figure 25. Optical micrographs of single tracks for each alloying composition printed at 212 W and 0.30 m/s are displayed in the left column with red and blue boxes indicating where WDS maps were conducted. The middle column shows WDS maps taken from the top of each melt pool, and the right column shows maps taken from the edges of each melt pool as color coded in the optical micrographs. White dotted lines indicate the boundaries of single tracks that are difficult to distinguish in these images.

Figures 25 and 26 display optical micrographs and WDS maps of single tracks at several parameter sets with lower energy densities than Figure 24. Cellular microsegregation structures are faintly observable in both the top and edge locations of NiCu printed at P = 212 W, v = 0.3 m/s, and LED = 706.7 J/m. At these parameters, less Cu segregation is observed (up to 3.5 at.%)

compared to single tracks printed at 5180 J/m (up to 5 at.%). No significant features are observed in the NiAl WDS maps in Figure 25, indicating that solidification speeds at these parameters are too high for even solute depletion at the melt pool boundary. Similarly to NiCu, Ni-5Zr displays lower relative amounts of segregation (up to 4at.% Zr) compared to tracks printed at 5180 J/m (up to 6 at.%). Ni-8.8Zr does not show significant differences in microstructure between the tracks printed at 706.7 J/m and 5180 J/m, displaying complete compositional homogeneity at both parameter sets. Figure 26 shows single tracks printed at two parameter sets ({P = 165 W, v = 0.55 m/s, LED = 300 J/m}, and {P = 118 W, v = 0.8 m/s, LED = 147.5 J/m}). NiCu, NiAl, and Ni-8.8Zr display planar microstructures at both parameter sets. Compositional fluctuation is observed in the WDS maps of NiCu, which may be due to local compositional differences in the baseplate and mixing between the base plate and the deposited powder. Ni-5Zr displays faint dendrite structures in the single track printed at 300 J/m, however, a planar structure is observed at 147.5 J/m. Variations in composition for Ni-5Zr printed at 147.5 J/m can be similarly attributed to local compositional differences between the powder and baseplate.

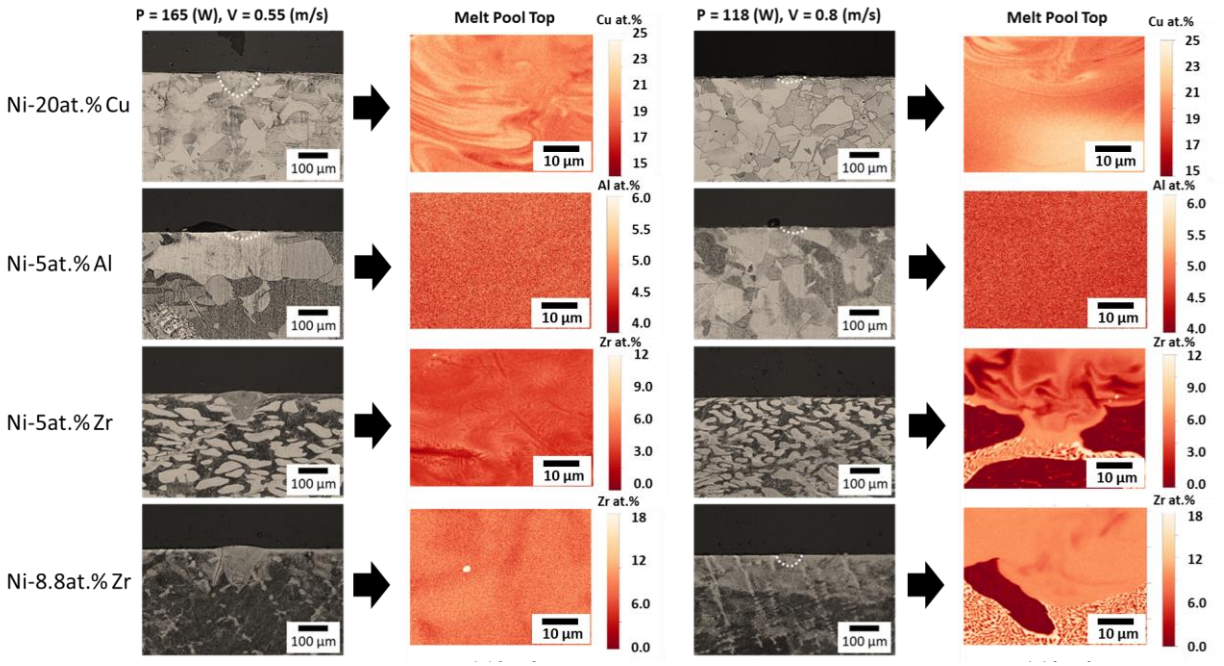

Figure 26. Optical micrographs of single tracks for each alloying composition printed at {165 W and 0.55 m/s} and {118 W and 0.80 m/s} are displayed to the left of their associated WDS maps. All WDS maps were taken from the top of each melt pool. White dotted lines indicate the boundaries of single tracks that are difficult to distinguish in these images.

Printability-Microstructure Processing Maps and Cube Sample Validation

PDAS is measured for each of the 46 single tracks across the four alloy systems to map the evolution of microsegregation across the laser power – scan speed parameter space. Figure 27 displays backscattered electron micrographs of etched NiCu single track cross sections that exemplify changes in PDAS at four different parameter sets. These micrographs demonstrate significant increases in dendrite size with increasing energy density. This is due to the changes in temperature gradient (G) and growth rate (R) with changing process parameters. Decreasing heat input results in smaller molten pools and a higher cooling rate ($G \times R$), whereas increasing heat input results in larger molten pools and lower cooling rates [98]. Lower relative cooling rates in

the LPBF process promote the growth of larger dendritic structures and vice versa. The heat maps plotted in Figure 28 show dendrite arm spacing quantified across the parameter space for each material. NiCu is observed to have dendritic structures between laser powers of 70 – 260 W and scan speed between 0 – 0.7 m/s, whereas dendrites are observed between 70 – 260 W and 0 – 1.3 m/s in Ni-5Zr. This larger range of dendritic growth in Ni-5Zr can be attributed to the larger solidification range and lower partition coefficient (172 K and 0.11 respectively) compared to NiCu (20 K and 0.74 respectively). However, the differences in scale bars for the two alloys in Figure 28 indicate that larger PDAS is observed in NiCu compared to Ni-5Zr. The heat maps also indicate that planar growth is observed throughout the parameter space for both NiAl and Ni-8.8Zr. These maps give a qualitative indication of expected dendritic growth throughout the parameter space for each of the alloys.

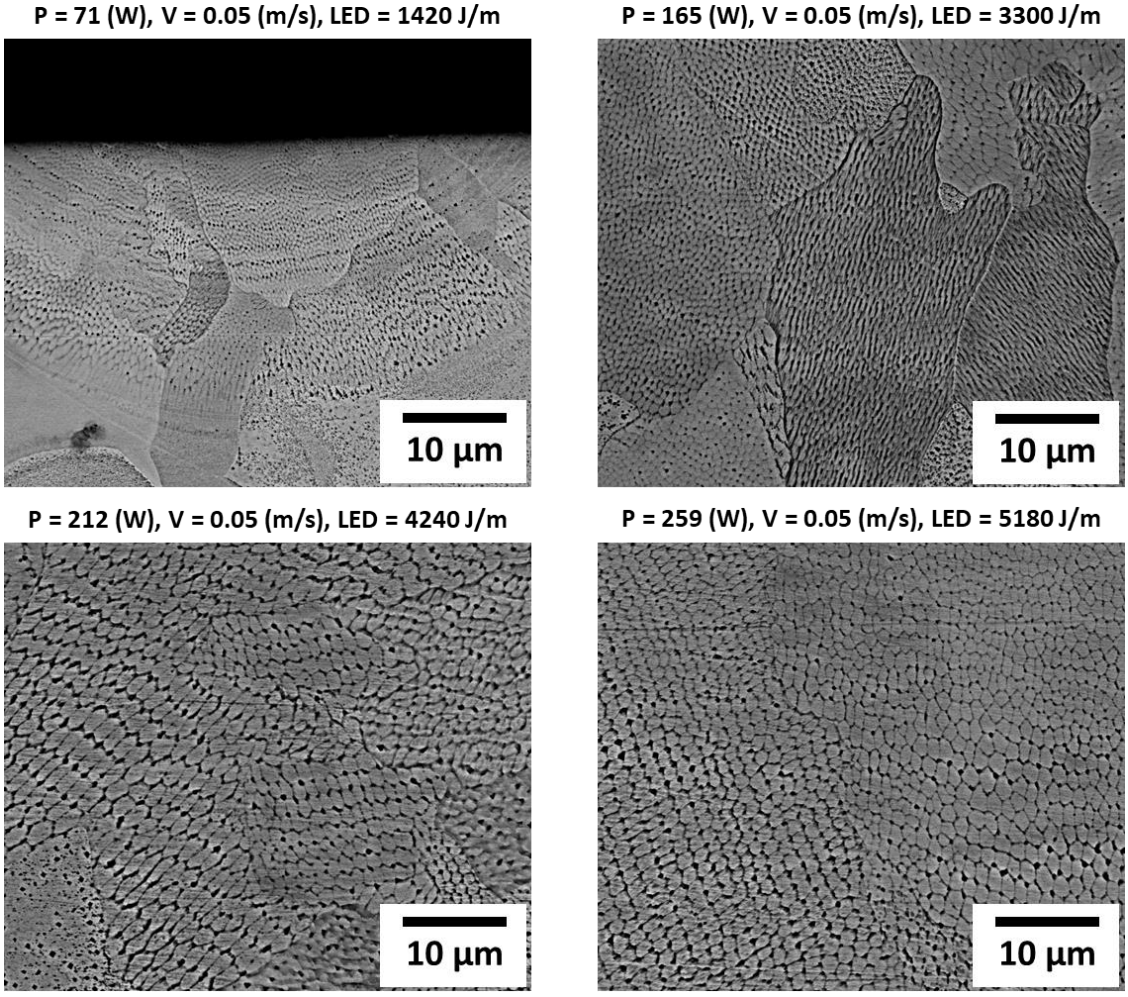

Figure 27. Backscattered electron images taken of Ni-20at.% Cu single tracks printed at {71 W and 0.05 m/s}, {165 W and 0.05 m/s}, {212 W and 0.05 m/s}, and {259 W and 0.05 m/s}. These micrographs display the significant differences in cellular-dendritic segregation structures at different locations in the laser power-scan speed parameter space.

To validate the PDAS heat maps displayed in Figure 28, the cubes are printed at three locations in the parameter space based on both the porosity processing maps and PDAS heat maps. Figures 29-32 display the combined porosity-microstructure processing maps for NiCu, NiAl, Ni-5Zr, and

Ni-8.8Zr respectively, as well as WDS maps for each of the printed cubes. Compositional measurements from the as-printed cubes correlate well with expected dendrite growth displayed in each of the processing maps. Cubes selected at PDAS values of 0.7 µm, 0.4 µm, and 0 µm from the NiCu processing map in Figure 29 demonstrate this correlation, showing significant dendrite structures at the 0.7 µm PDAS parameter set, moderate dendrite structures at 0.4 µm, and a planar microstructure at 0 µm. Solute depletion along melt pool boundaries is observable in each of the NiCu cubes. Similarly, Figure 31 displays significant segregation of Zr (up to 4 at.%) in cubes printed at PDAS values of 0.3 µm and 0.25 µm in the processing map, but shows lower relative amounts of Zr segregation (~1 at.%) at 0.15 µm. Both NiAl and Ni-8.8Zr in Figures 30 & 32 display planar microstructures in cubes across the parameter space, as is expected from the processing maps. Additionally, a general depletion of Al is observed in Figure 30 with an increase in laser power. This may be due to the evaporation of Al in the as-printed bulk material under higher laser powers. These results validate that observations of microsegregation and dendrite size in single tracks can be used to qualitatively assess microstructural development in printed parts and generate microstructure processing maps for L-PBF.

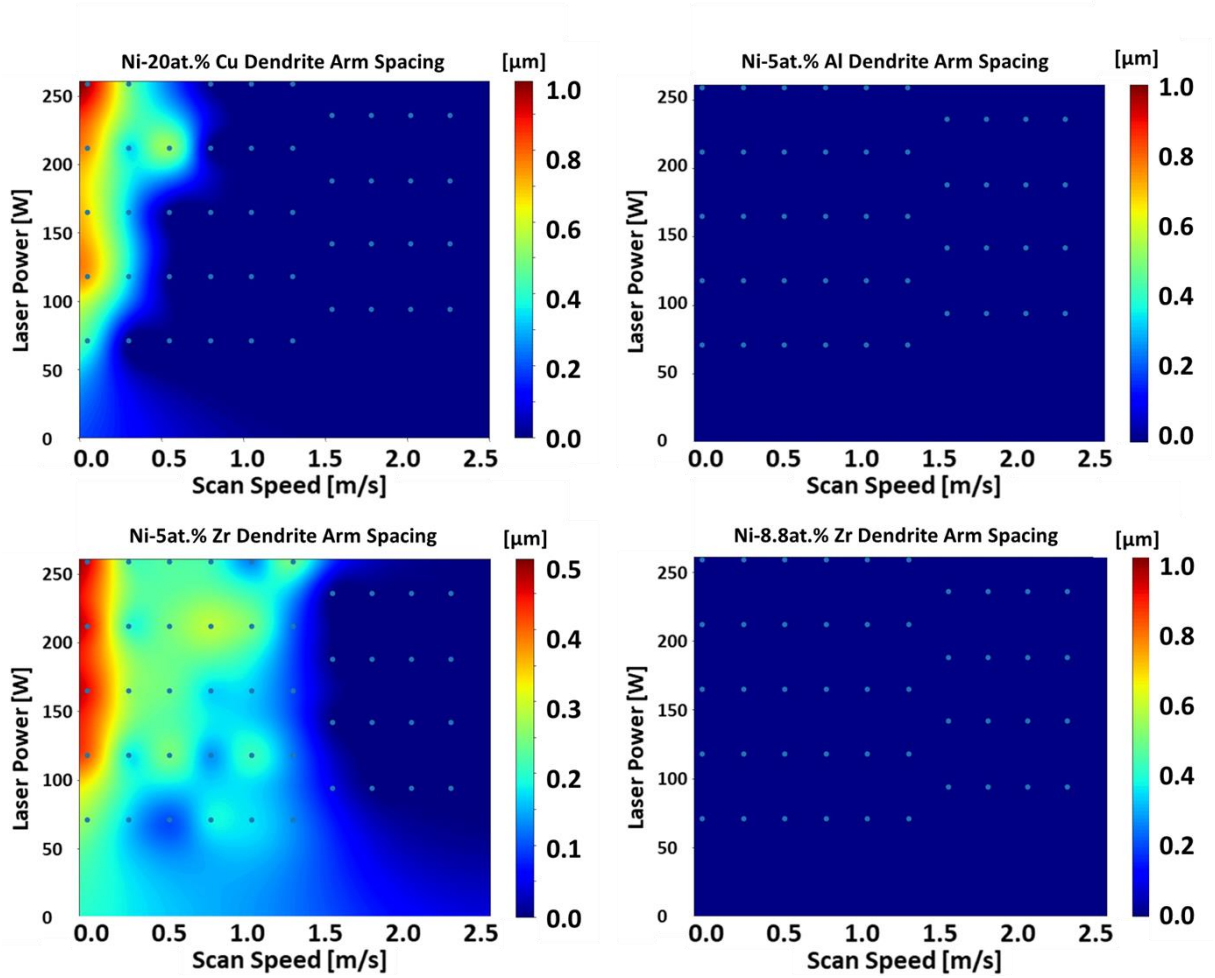

Figure 28. Primary dendrite arm spacing measurements taken from 46 single tracks across the parameter space are interpolated using multilevel B-splines approximation to construct heat maps of each alloy. Observations of planar growth instead of cellular-dendritic growth structures are indicated by zero values in the heat maps. The markers displayed inside the heat maps indicate the location of 46 single tracks that PDAS measurements were taken from.

Statistical Analysis and Empirical Equation for PDAS in L-PBF

Several equations have been proposed to predict PDAS for alloys subjected to rapid solidification conditions. The Kurz-Fisher [99] and Trivedi [100] models predict PDAS as a function of material properties such as the equilibrium and rapid solidification ranges, liquid

diffusion coefficient, Gibbs-Thomson coefficient, and partition coefficient as well as solidification conditions such as the temperature gradient and solidification rate. However, material properties such as the Gibbs-Thomson coefficient and liquid diffusion coefficient are not easily obtainable for new alloy systems. Additionally, L-PBF conditions can vary locally throughout a build and solidification conditions are subject to significant variation depending on the local thermal histories and heat dissipation mechanisms. These variables do not readily translate to usable parameter input data or material selection constraints. A model predicting PDAS as a function of easily obtainable material properties and L-PBF process parameters such as laser power and scan speed would therefore be useful in determining PDAS. Single track data from this study is used to statistically test the sensitivity of PDAS values to material properties and process parameters, and an empirical equation is developed to predict PDAS in L-PBF.

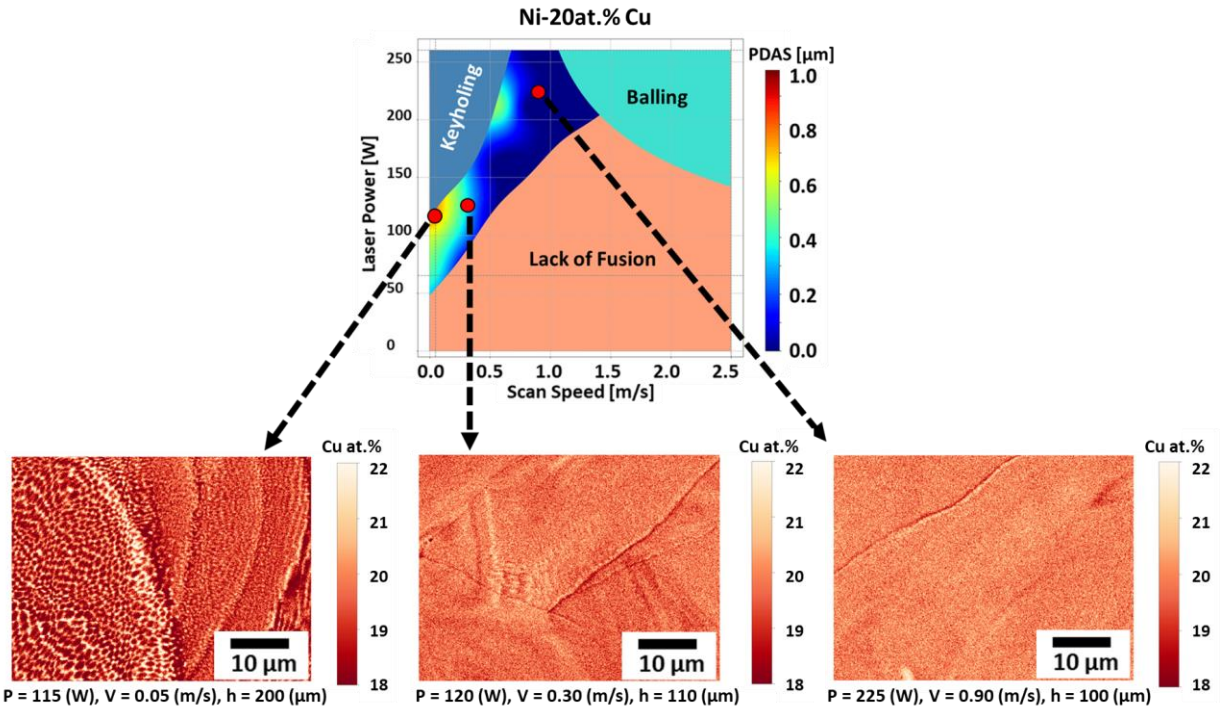

Figure 29. A combined Porosity-Microstructure processing map for Ni-20at.% Cu, as well as wavelength dispersive spectroscopy (WDS) composition maps taken from each of the printed cubes listed in Table 4. The cubes were printed at {P = 115 W, v = 0.05 m/s, h = 200 µm}, {P = 120 W, v = 0.30 m/s, h = 110 µm}, and {P = 225 W, v = 0.90 m/s, h = 100 µm}.

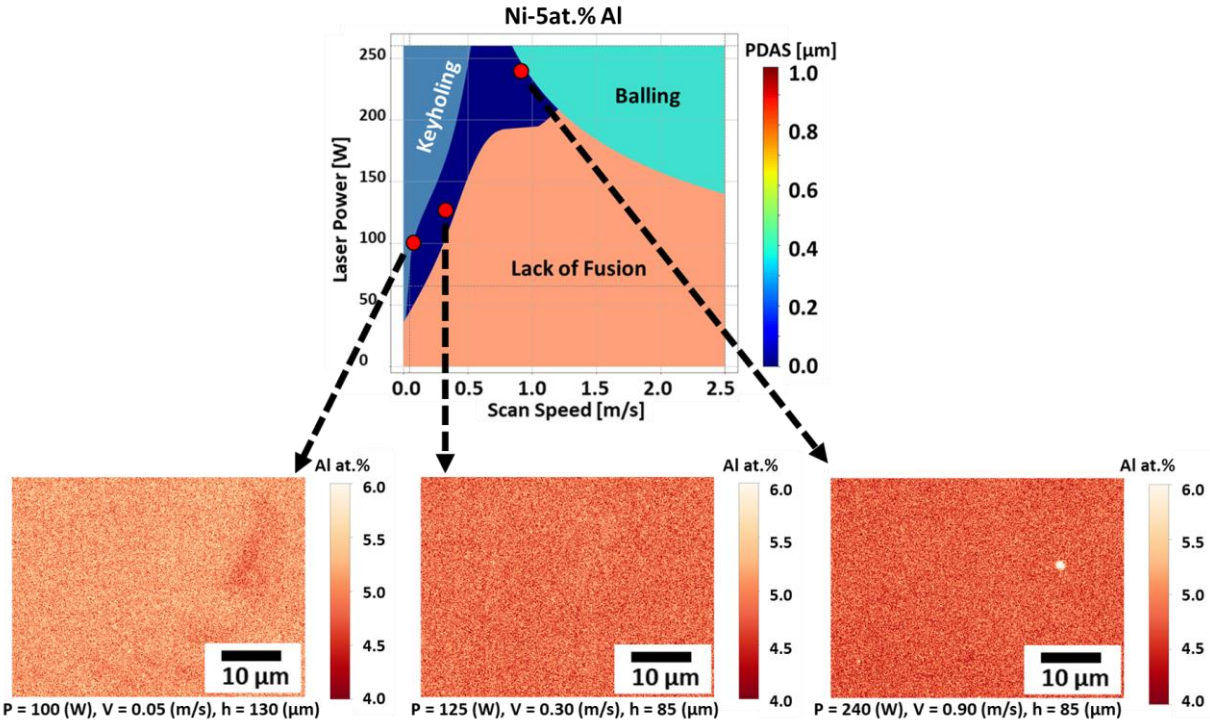

Figure 30. A combined Porosity-Microstructure processing map for Ni-5at.% Al, as well as wavelength dispersive spectroscopy (WDS) composition maps taken from each of the printed cubes listed in Table 4. The cubes were printed at {P = 100 W, v = 0.05 m/s, h = 130 μm}, {P = 125 W, v = 0.30 m/s, h = 85 μm}, and {P = 240 W, v = 0.90 m/s, h = 85 μm}.

The dataset presented in this study is considered sparse and high dimensional. To better understand the influence of different variables on PDAS, as well as to create predictive models, materials informatics strategies were employed. Materials informatics allows analysis of high-dimensional materials data through machine learning [101,102]. Features included in the database consisted of the material properties listed in Table 1, single track process parameters and PDAS values, and other available thermodynamic properties of the alloy systems. The PDAS dataset collected from the four alloys was initially sampled to obtain an optimal distribution of data representative of the PDAS value range. This required many of the PDAS values equal to zero to

be dropped from the analysis. The dataset was then split into two parts with 80% of the data being used to train the machine learning model and the remaining 20% of the data used to test model accuracy. Primary analysis of the data was done using a Random Forest regression technique [103] and the model performance values for the test set are displayed in Figure 33a. The trained model predicted the test set with a root mean squared error of 0.12 μm and a mean absolute error of 0.08 μm, indicating a high degree of model accuracy. Feature sensitivity analysis was used to identify feature importance and determined that the most important features contributing to PDAS were: scan speed, melting temperature, laser power, partition coefficient, and freezing range, as can be seen in Figure 33b. Scan speed is observed to have the most substantial impact on PDAS. Laser scan speed is highly correlated with solidification growth rate since the tail of a molten pool is expected to have a growth rate equal to the scan speed of the laser [56]. This result is therefore consistent with expectations of laser scan speed's effect on dendrite growth. PDAS is also observed to be sensitive to alloy melting temperature. However, this sensitivity may be inflated by the relatively low number of alloy systems used as training data for this analysis as well as the omission of many of the PDAS values equal to zero as previously discussed.

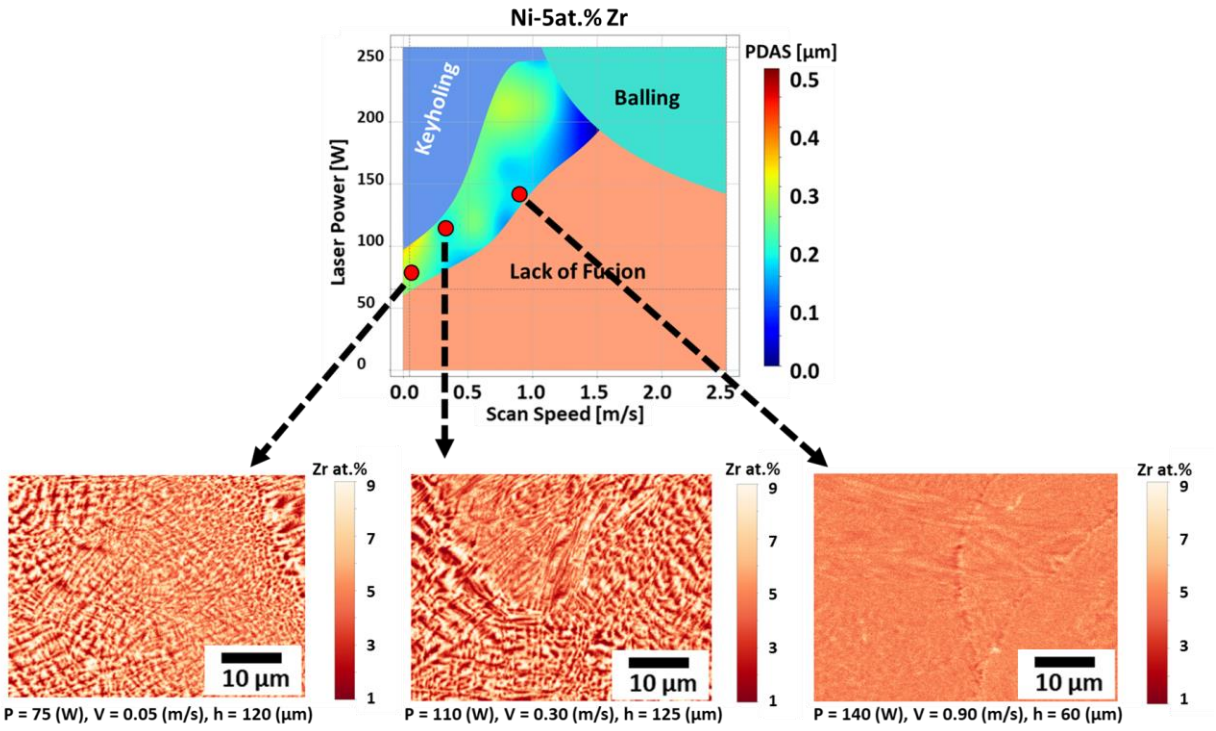

Figure 31. A combined Porosity-Microstructure processing map for Ni-5at.% Zr, as well as wavelength dispersive spectroscopy (WDS) composition maps taken from each of the printed cubes listed in Table 4. The cubes were printed at {P = 75 W, v = 0.05 m/s, h = 120 µm}, {P = 110 W, v = 0.30 m/s, h = 125 µm}, and {P = 140 W, v = 0.90 m/s, h = 60 µm}.

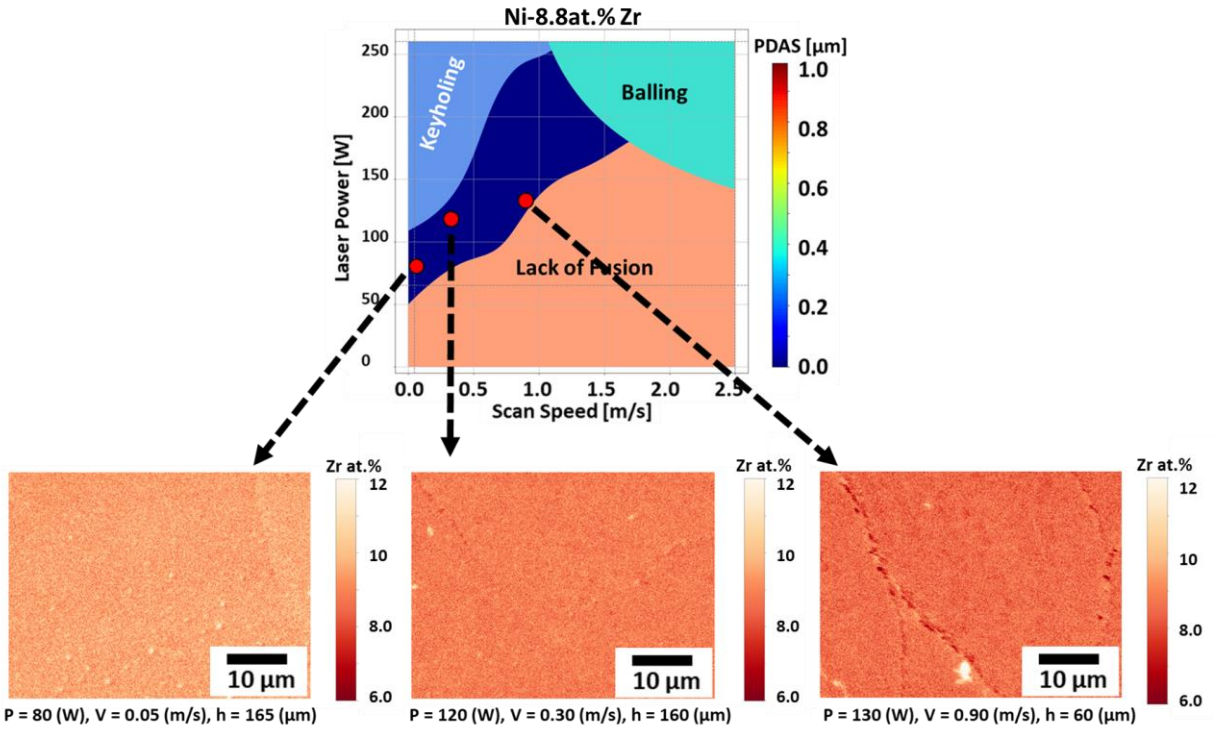

Figure 32. A combined Porosity-Microstructure processing map for Ni-8.8at.% Zr, as well as wavelength dispersive spectroscopy (WDS) composition maps taken from each of the printed cubes listed in Table 4. The cubes were printed at {P = 80 W, v = 0.05 m/s, h = 165 µm}, {P = 120 W, v = 0.30 m/s, h = 160 µm}, and {P = 130 W, v = 0.90 m/s, h = 60 µm}.

Feature engineering and generation was used to create new features using mathematical operators and combinations of process parameters and material properties. A linear regression model was then used to evaluate the accuracy of the new features in predicting PDAS. Linear regression is employed for its simplicity and low computational cost. Features that showed poor predictive accuracy were dropped from the model, and those with good performance were improved upon in an iterative process. This feature engineering and selection process is described in more detail by Horn et al. [104]. No more than 6 parameter and material property combinations

were used to generate a new feature. After numerous iterations, the following empirical formula was derived:

$$\lambda_{PDAS} = Log(\frac{P^{0.18}\Delta T^{0.26}k_e^{0.75}c_p^5}{v^{0.18}T_m^{9.41}}) + 16.10, \qquad (2)$$

Here, P is laser power, v is laser scan speed, ΔT equilibrium solidification range, k_e is the partition coefficient, c_p is the specific heat capacity, T_m is the alloy melting temperature, and λ_{PDAS} is the primary dendrite arm spacing in µm. This equation is fit to single track PDAS data in Figure 33c and exhibits a root mean squared error of 0.0842 µm and a mean absolute error of 0.0641 µm. The feature engineered model takes a similar approach to the classical mass balance and minimum undercooling PDAS prediction model developed by Hunt [105] in that k_e and ΔT are multiplied in the expression. This relationship illustrates the differences in segregation across the parameter space between the alloys. If the k_e and ΔT values are multiplied for each alloy, NiCu has a $k_e \times \Delta T \approx 15$ and Ni-5Zr has a value ≈ 19, whereas NiAl and Ni-8.8Zr have values of $k_e \times \Delta T$ near or equal to zero. However, this does not explain why the NiCu single tracks were observed to have PDAS values larger than Ni-5Zr. Thermal properties not reported for these alloy systems such as the liquid diffusion coefficients, Gibbs-Thomson coefficients, and thermal conductivities may play a role in the observed differences in absolute PDAS values. Additionally, the inverse relationship between k_e and ΔT and their effect on dendrite growth may explain why PDAS does not appear to be as sensitive to these values as v and P. In general, a larger solidification range implies a smaller partition coefficient. When the quantities are multiplied this inverse relationship results in them 'canceling' each other. In contrast, the other important factors (T_m, P, and v) are completely independent of each other and their effect on PDAS is more direct. Due to the limited dataset generated by this study it is likely that the empirical model will need modification to be generalizable for significantly different alloy systems. However, a generalizable model using L-

PBF process parameters and simple material property inputs will likely prove invaluable for designing new alloys for AM.

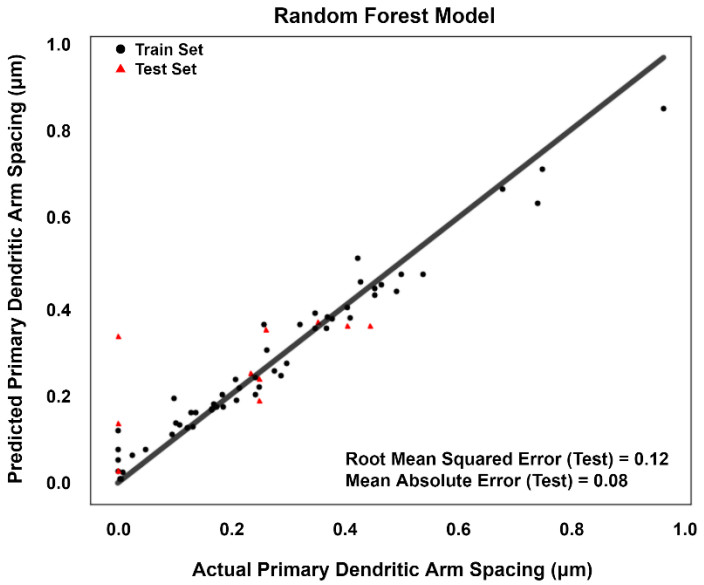

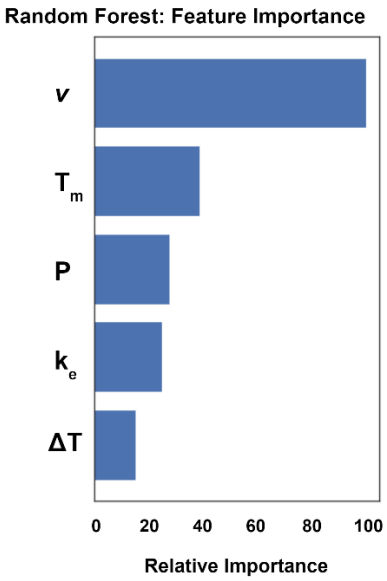

(a) **(b)**

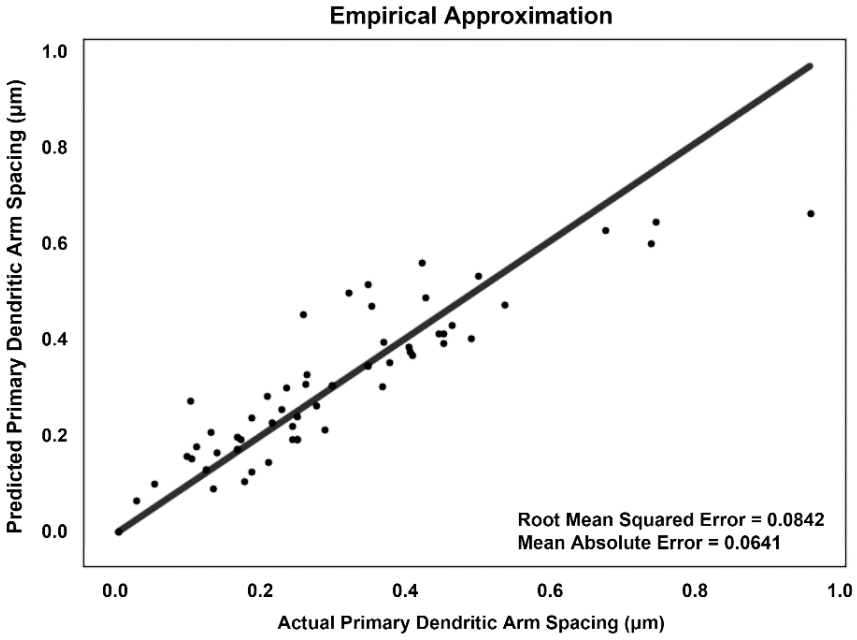

(c)

Figure 33. Materials informatics strategies employed to analyze the high-dimensional materials data presented in this study through machine learning. a) A Random Forest validation plot showing the model fit to the train and test PDAS datasets. b) A Random Forest feature importance plot displaying the sensitivity of PDAS to material properties and process parameters. c) A validation plot displaying the predictive accuracy of the empirical model developed in this study. v: Laser Scan Speed, T_m: Alloy Melting Temperature, P: Laser Power, k_e: Partition Coefficient, ΔT: Alloy Solidification Temperature Range.

Post-Processing Effects on As-Printed AF9628

Microstructural Analysis

Figure 34 displays an optical micrograph of AF9628 in the as-printed condition showing the layered appearance of melt pool structures and heat affected zones (HAZ) due to the bidirectional laser scan strategy with layers alternating by 90° in the x-y plane. These types of features have been previously observed in LPBF low alloy steels [21,63,64]. Bright and dark regions are observable in the as-printed micrograph, and represent varying degrees of tempering in the specimen [21,63,64]. Bright regions are areas within the melt pools and along the melt pool boundaries that reached austenitization temperatures and were subjected to rapid cooling associated with the LPBF process (10^4-10^6 K/s [2]). This quenching results in the formation of new martensitic laths in these areas [21,63,64]. Darker regions are further from the molten pool during layer deposition and do not reach the critical austenitization temperature, resulting in an effective tempering of the region [21,63,64]. These darker regions have been reported to cause mechanical anisotropy in LPBF low alloy steels due to their layered pattern along the building direction of as-printed specimens [21,63]. Optical micrographs of as fabricated and then heat-

treated materials in each condition (HT1, HT2, and HT3) are also displayed in Figure 34. These micrographs exhibit a homogenous microstructure with no observable melt pool boundaries or HAZs. No obvious differences in microstructure are observable in optical images of the specimens in the three heat treatment conditions, except notably larger microstructural features in the HT3 condition. Additionally, no cracking was observed in any of the as-printed or heat treated conditions. This indicates that stress relief is not a necessary post-processing step for LPBF AF9628.

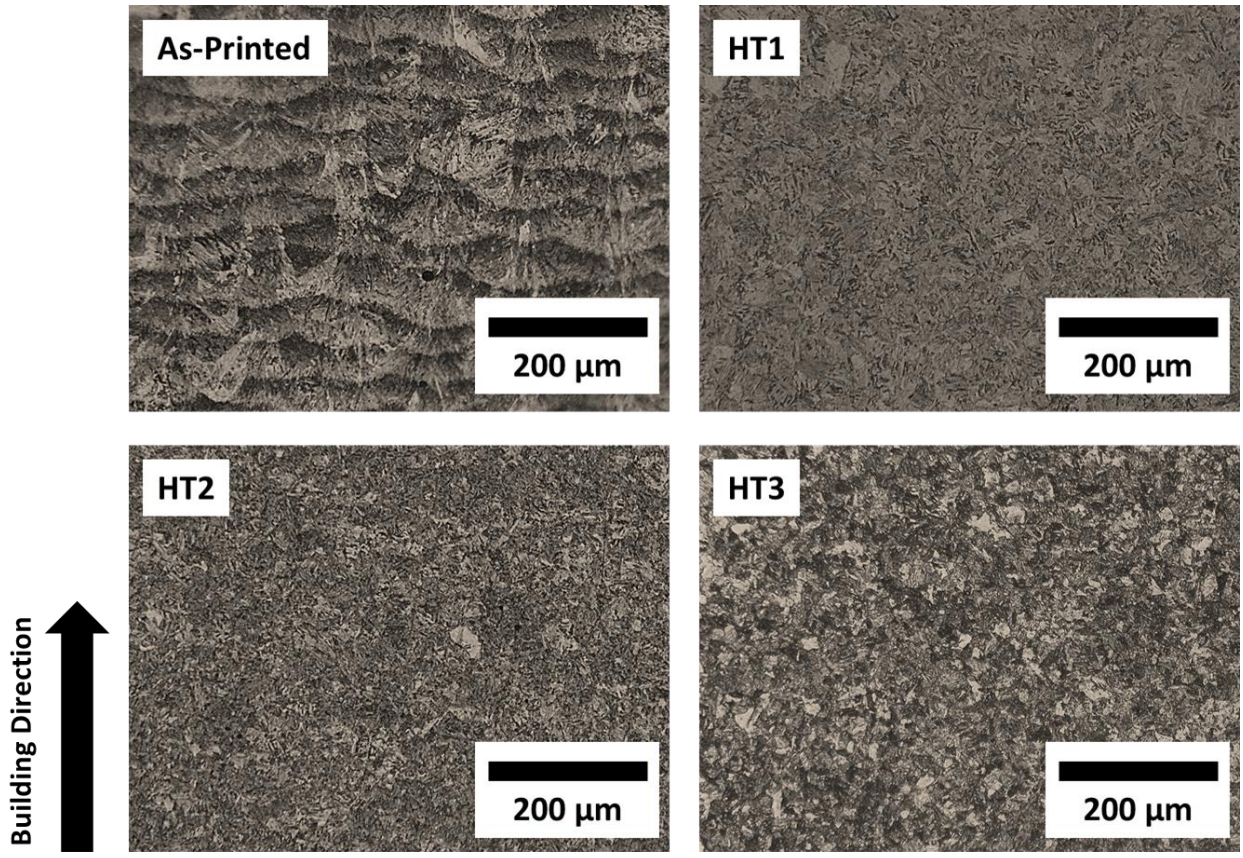

Figure 34. Optical micrographs of AF9628 steel cube cross sections etched with Vilella's reagent in the as-printed, HT1, HT2, and HT3 processing conditions. These micrographs display the melt pool boundaries in the as-printed condition, and overall microstructure in other cases. HT1: stress

relief, normalization, austenitization, and tempering; HT2: stress relief, austenitization, and tempering; HT3: normalization, subcritical anneal, austenitization, and tempering.

X-ray diffraction was utilized for phase analysis in the various processing conditions of AF9628, the results for which are displayed in Figure 35. Diffraction peaks are observed for all conditions are the characteristic spectra of the martensite and α-ferrite phases at 44.9°, 65.3°, and 82.5°. A relatively small peak was observed in the as-printed material at 43.5° which may correspond to the Fe_3C cementite phase, and is consistent with what is found in the literature [21]. Seede et al. [21] reported the occurrence of small XRD peaks at 43.5˚ and 71.1˚ in an as-printed AF9628 specimen printed at 125 W, 750 mm/s, 75 μm hatch spacing, and a layer thickness of 37 μm. Although the peak at 43.5˚ is close to a characteristic retained austenite peak (42.92˚), the nearest austenite peak to 71.1˚ is 73.37˚. In contrast, both peaks can be more closely associated with characteristic Fe_3C peaks (43.87˚ and 71.05˚). However, no obvious Fe_3C or retained austenite were observed in SEM micrographs (Figure 36), no chemical segregation indicating Fe_3C was detected in WDS analysis (Figure 37), and neither Fe_3C nor retained austenite could indexed during EBSD analysis (Figure 38). In light of this, the small diffraction peak at 43.5° appears to indicate the existence of cementite in the as-printed condition which may be due to thermal cycling and effective tempering that are a result of the layer by layer deposition process in LPBF [21]. However, a thorough phase analysis using transmission electron microscopy would be useful to provide definitive evidence for the existence of Fe_3C or retained austenite in as-printed AF9628. The diffraction peaks at 44.9°, 65.3°, and 82.5° also overlap with the characteristic spectra of Fe_3C and further phase analysis is required to determine whether small relative amounts of cementite exist in the powder and heat-treated conditions. No obvious Fe_3C precipitates are observed in the

SEM micrographs of the HT1, HT2, or HT3 material displayed in Figure 39 or the WDS maps in Figure 40. It is possible that the cementite precipitates in the as-printed condition were too fine to observe under SEM. The austenitization and quenching process in each of the three heat treatment schedules is expected to promote a fully martensitic microstructure. Microstructural data on the heat-treated material from Figures 35-37 are therefore within expectations for the heat-treated material. Small manganese and silicon inclusions are observable as bright white spots in the WDS elemental maps of the as-printed material displayed in Figure 37a. These inclusions are likely Mn and Si oxides (MnO and SiO_2) commonly observed in high strength - low alloy steel welds [106]. Manganese inclusions are also found in WDS maps of the HT3 specimen (Figure 37b), however, no silicon inclusions are observable. The cellular-dendritic elemental segregation reported in AF9628 powder [21] and observed in many other 3D printed alloy systems [2] is not evident in WDS maps of as-printed AF9628. Interestingly, depletion of Si, Mo, Cr, and Mn along with the segregation of Fe is observed in low relative amounts along the melt pool boundaries of the as-printed specimen in Figure 37a. The phenomenon of solute depletion has been reported in the literature and is due to the low solidification growth rates along the melt pool boundary [56]. It is not clear whether this influences the mechanical properties of the material.

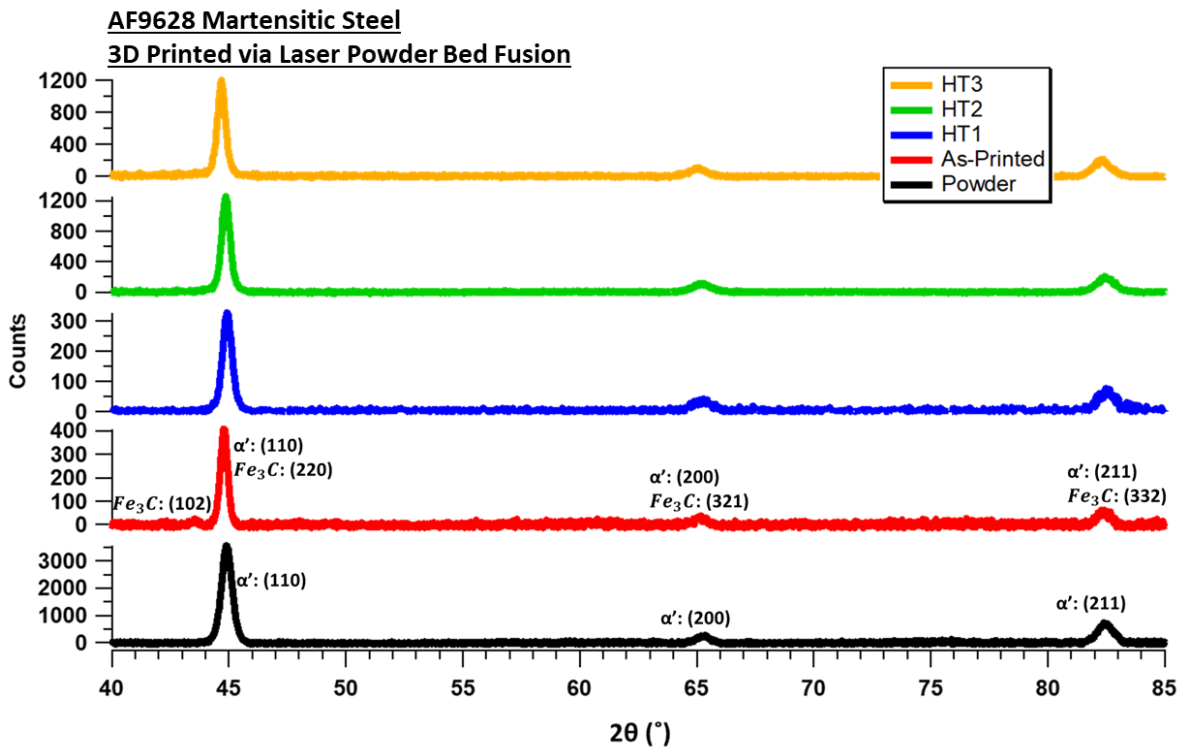

Figure 35. AF9628 X-Ray Diffraction spectra observed in powder, as-printed specimens, and heat treated (HT1, HT2, and HT3) specimens. HT1: stress relief, normalization, austenitization, and tempering; HT2: stress relief, austenitization, and tempering; HT3: normalization, subcritical anneal, austenitization, and tempering.

Crystallographic and mesotexture analysis was conducted using EBSD and inverse pole figure (IPF) maps of the as-printed and heat-treated materials are displayed in Figure 38a. These IPF maps reveal the martensitic microstructure of AF9628 in each condition. The average martensitic lath sizes determined for each of these maps are presented in Table 5. Martensitic laths observed in the as-printed condition are larger than those observed in the heat-treated material. The as-printed material had an average lath size of 6.3 ± 1.5 µm, whereas HT1, HT2, and HT3 had average lath sizes of 3.4 ± 2.3 µm, 2.7 ± 1.4 µm, and 3.1 ± 1.8 µm respectively. Lath sizes between the

heat-treated materials were not significantly different from each other, and each was within 1 standard deviation of the others. The inverse pole figures displayed in Figure 38b illustrate the mesotexture observed in each of the IPF maps in Figure 38a. A weakly textured microstructure is observed in the [001] direction in the as-printed material. In contrast, the heat treatments HT1 and HT3 resulted in a weakly textured microstructure oriented in the [111] direction, and HT2 resulted in a weak bimodal texture distribution in the [111] and [001] directions.

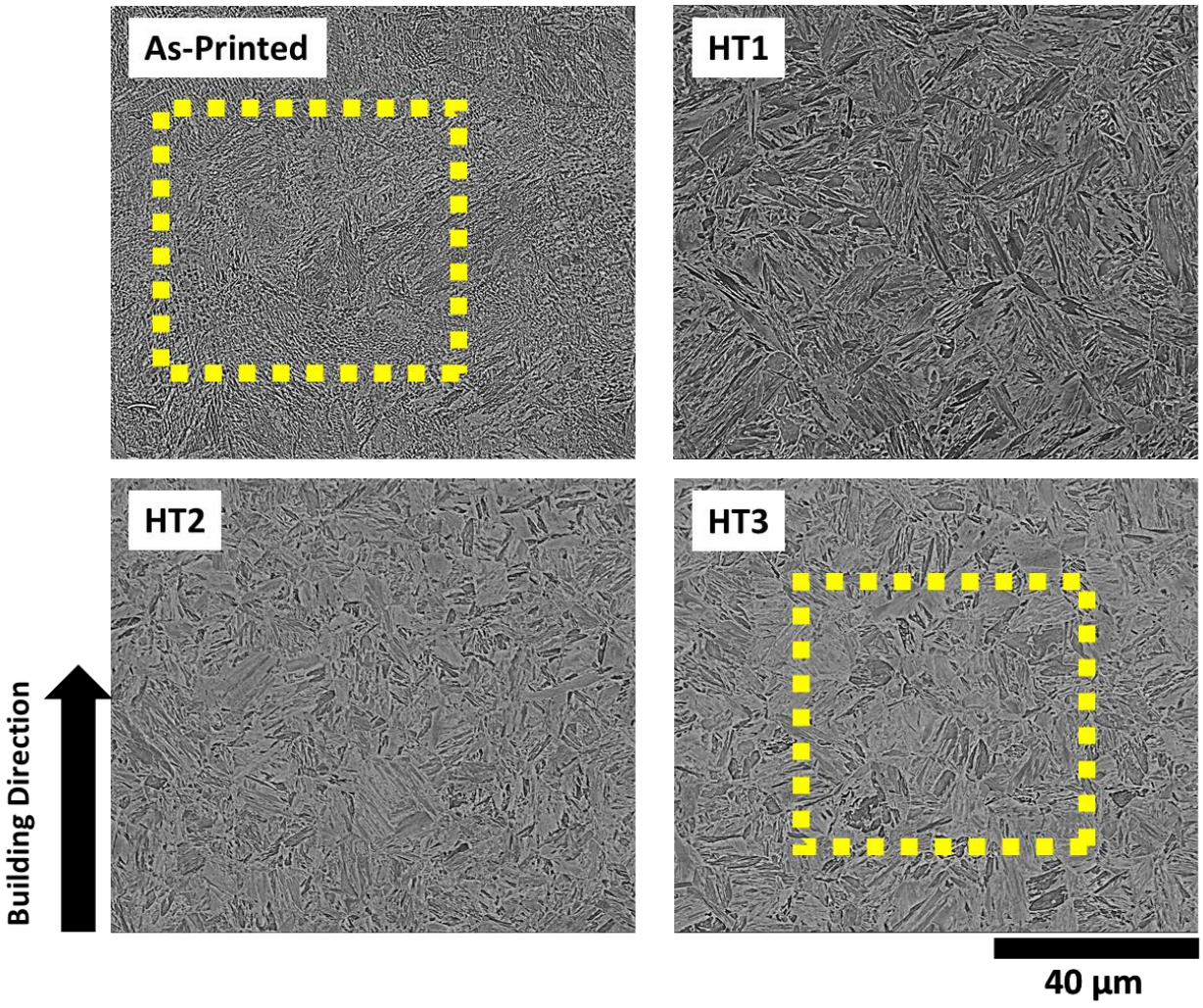

Figure 36. Backscattered electron images of AF9628 etched using Nital in each processing condition. These micrographs display the martensitic microstructure observed in each condition.

The yellow dotted lines in the as-printed and HT3 images provide a visual reference for the wavelength dispersive spectroscopy maps in Figure 37. HT1: stress relief, normalization, austenitization, and tempering; HT2: stress relief, austenitization, and tempering; HT3: normalization, subcritical anneal, austenitization, and tempering.

Table 5. Average microstructural feature sizes of AF9628 in the as-printed and heat treated (HT1, HT2, and HT3) conditions. Average martensite lath sizes were extracted by the EBSD post-processing software after acquiring EBSD data for each specimen. Average prior austenite grain sizes were obtained from the prior austenite grain maps produced by limiting the misorientation angle of each IPF map between 15-48˚, following the methodology described in [51,88,89]. The ± values represent 1 standard deviation from the mean for each measurement. HT1: stress relief,

normalization, austenitization, and tempering; HT2: stress relief, austenitization, and tempering; HT3: normalization, subcritical anneal, austenitization, and tempering.

Processing Condition	Prior Austenite Average Grain Size (μm)	Martensite Lath Average Equivalent Diameter (μm)
As-Printed	20.1 ± 7.1	6.3 ± 1.5
HT1	16.8 ± 2.0	3.4 ± 2.3
HT2	12.4 ± 2.3	2.7 ± 1.4
HT3	11.2 ± 2.0	3.1 ± 1.8

Figure 39 displays prior austenite grain (PAG) boundary images extracted from the EBSD data. As-printed specimens exhibit large (20.1 ± 7.1 μm) anisotropic columnar PAGs compared to the smaller equiaxed PAGs in HT1, HT2, and HT3 (16.8 ± 2.0 μm, 12.4 ± 2.3 μm, and 11.2 ± 2.0 μm respectively). The columnar PAG structures in as-printed specimens formed due to the epitaxial grain growth mechanism typically observed in LPBF alloys [2]. HT1 reduced PAG size by ~16%, while HT2 and HT3 had 38% and 44% smaller PAGs, respectively, compared to the as-printed material and were within 1 standard deviation of each other. The measured average martensitic lath and PAG sizes correlate well with the mechanical properties reported in Section 3.2 of this work.

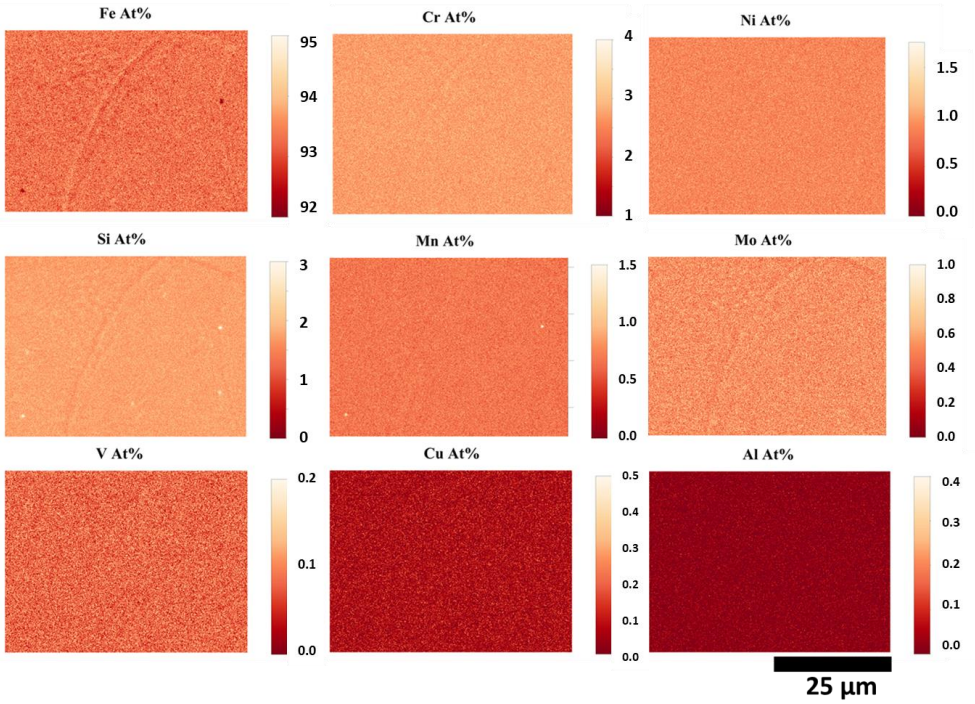
Fe At%
95
94
93
92
Cr At%
4
3
2
1
Ni At%
1.5
1.0
0.5
0.0
Si At%
3
2
1
0
Mn At%
1.5
1.0
0.5
0.0
Mo At%
1.0
0.8
0.6
0.4
0.2
0.0
V At%
0.2
0.1
0.0
Cu At%
0.5
0.4
0.3
0.2
0.1
0.0
Al At%
0.4
0.3
0.2
0.1
0.0
25 µm

(a)

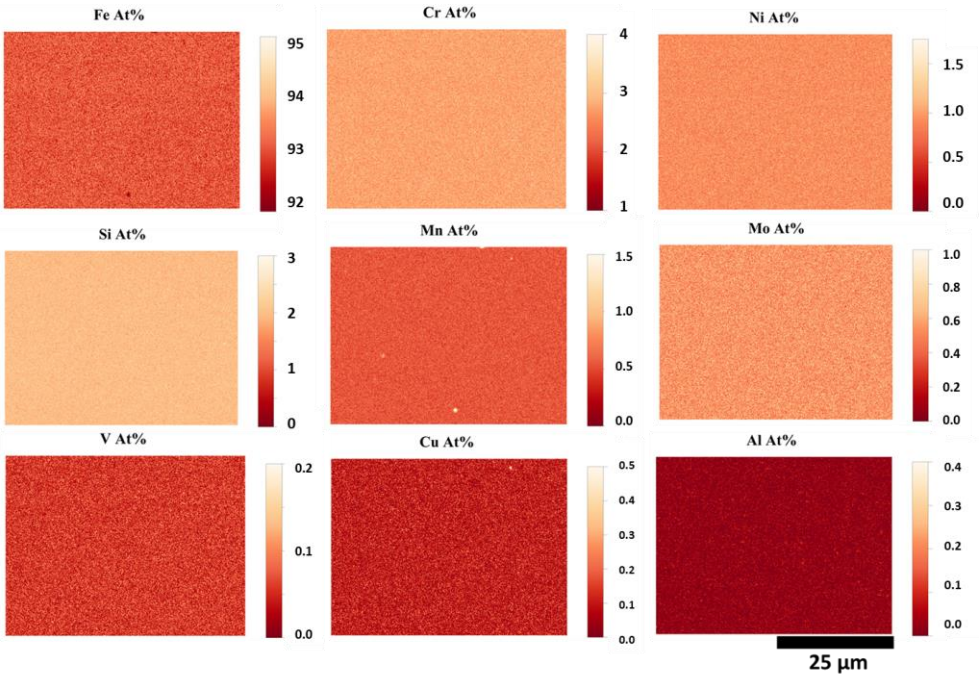
Fe At%
95
94
93
92
Cr At%
4
3
2
1
Ni At%
1.5
1.0
0.5
0.0
Si At%
3
2
1
0
Mn At%
1.5
1.0
0.5
0.0
Mo At%
1.0
0.8
0.6
0.4
0.2
0.0
V At%
0.2
0.1
0.0
Cu At%
0.5
0.4
0.3
0.2
0.1
0.0
Al At%
0.4
0.3
0.2
0.1
0.0
25 µm

(b)

Figure 37. Wavelength dispersive spectroscopy (WDS) maps of AF9628. (a) A WDS map of the as-printed material showing the distribution of elements in a 51.5×51.5 µm map of the material. The yellow dotted box in the micrograph of the as-printed processing condition in Figure 36 provides a visual reference for these maps. (b) A WDS map of the heat treatment condition HT3 showing the distribution of elements in a 51.5×51.5 µm map of the material. The yellow dotted box in the micrograph of the heat treatment condition HT3 in Figure 36 provides a visual reference for these maps. Each elemental map in (a) and (b) has a scale bar on the right with compositions displayed in at.%.

Mechanical Properties

Vickers microhardness tests were conducted transverse to the building direction with multiple measurements per sample being recorded along the building direction, as illustrated in Figure 40a. The hardness measurements, displayed in Figure 40b and tabulated in Table 6, determined an average hardness of 482.2 ± 22.0 HV, 469.8 ± 10.6 HV, 500.1 ± 5.8 HV, and 501.9 ± 9.2 HV for the as-printed, HT1, HT2, and HT3 conditions respectively. The as-printed material displays large fluctuations in hardness with a standard deviation of ± 22.0 HV due to the microstructural inhomogeneity and variations in local tempering caused by thermal cycling observed in Figure 34. Variations in microhardness due to bands of tempered and untempered martensite were similarly observed by Dilip et al. [63] in as-printed HY100. A spike in hardness to almost 580 HV is observed at the top of the as-printed specimen. This spike has been reported in the literature for low alloy - high strength steels and is due to the untempered martensite at the top of the as-printed specimens [21,63]. Since no layers are deposited above the top layer, tempering of the layer due to HAZ reheating does not occur and results in an untempered martensitic microstructure

significantly harder than the rest of the material. Overall hardness observed in the HT1 specimen decreased by 2.5% compared to the as-printed material. However, if the high hardness at the top of the as-printed specimen and low hardness at the edges of the HT1 specimen are not considered, no difference is observed between the two conditions. HT2 and HT3 specimens displayed hardness values within 1 standard deviation of each other and ~4% greater than the as-printed specimen.

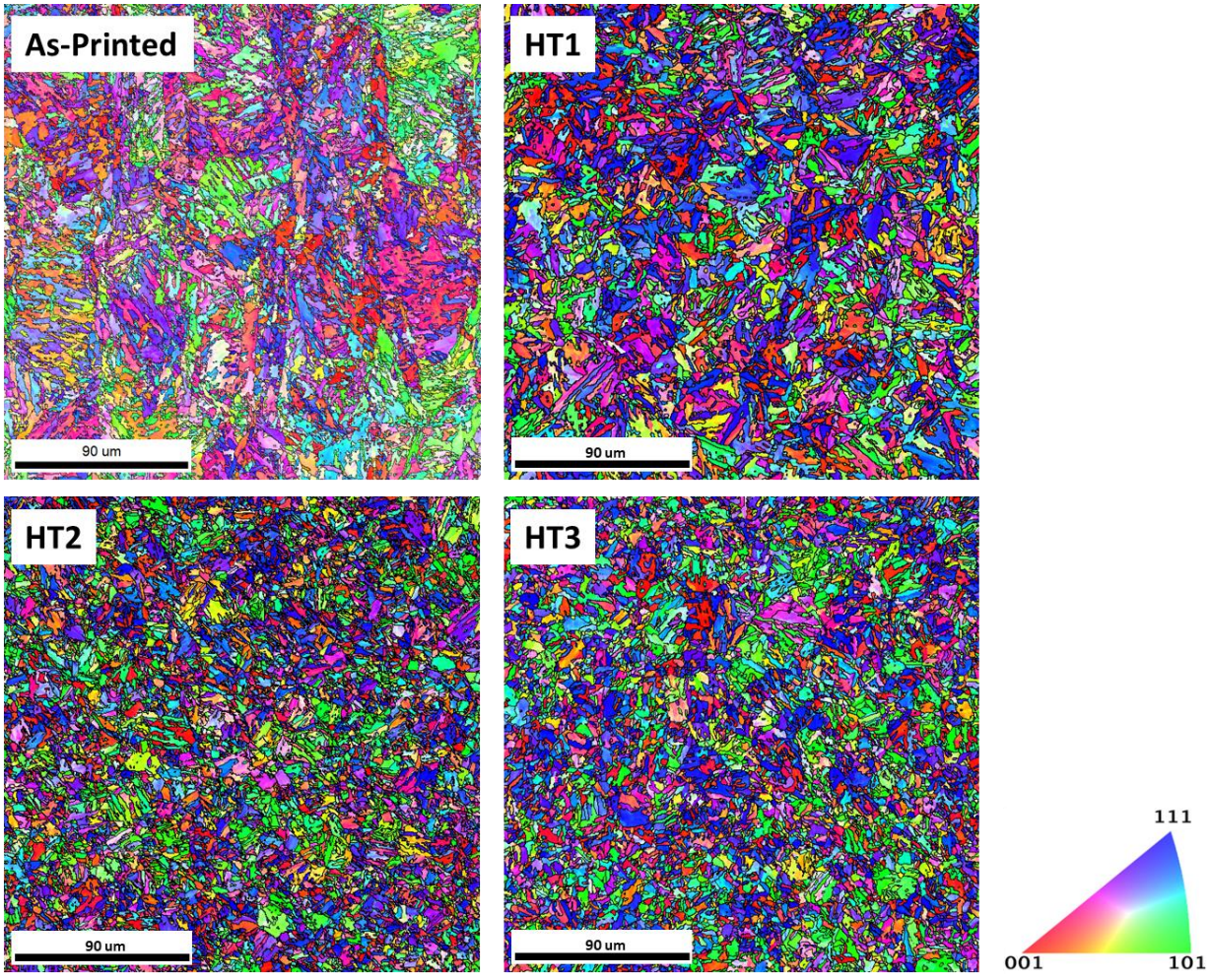

(a)

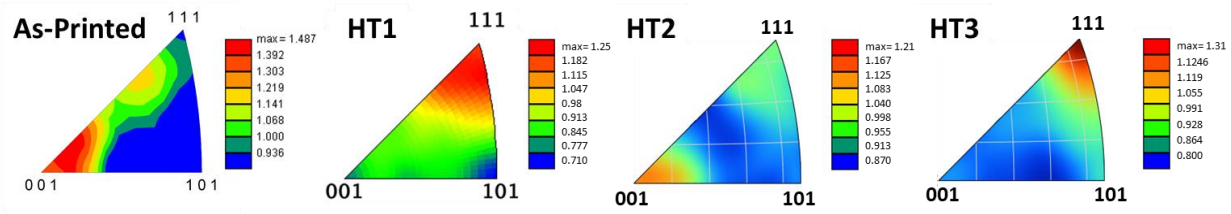

(b)

Figure 38. Representative EBSD maps of AF9628 as-printed and heat treated cubes and the corresponding data collected from a viewing plane parallel to the building plane (a) Inverse pole figure (IPF) maps of the martensitic phase in the as-printed, HT1, HT2, and HT3 conditions. (b) The inverse pole figures associated with each IPF map revealing mesotexture of the scanned area of each specimen. Refer to Table 5 for the corresponding average grain size data extracted from the IPF maps. HT1: stress relief, normalization, austenitization, and tempering; HT2: stress relief, austenitization, and tempering; HT3: normalization, subcritical anneal, austenitization, and tempering.

Table 6. Average mechanical property values measured on AF9628 in the as-printed and heat treated conditions. Tensile and hardness tests were conducted at room temperature, whereas Charpy impact testing was conducted at -40 °C. The ± values represent 1 standard deviation from the mean for each measurement. HT1: stress relief, normalization, austenitization, and tempering;

HT2: stress relief, austenitization, and tempering; HT3: normalization, subcritical anneal, austenitization, and tempering.

Sample	Yield Strength (0.2%) (MPa)	Ultimate Tensile Strength (MPa)	Elongation to Failure (%)	Vickers Hardness (HV)	Charpy Impact Toughness (J)
As-Printed	1079 ± 2.3	1409 ± 1.4	10.33 ± 0.31	482.2 ± 22.0	27.82 ± 1.50
HT1	1208 ± 3.7	1538 ± 0.4	7.15 ± 0.13	469.8 ± 10.6	23.56 ± 1.23
HT2	1435 ± 0.5	1655 ± 1.4	5.37 ± 1.00	500.1 ± 5.8	24.06 ± 6.05
HT3	1310 ± 5.7	1663 ± 1.1	7.63 ± 0.04	501.9 ± 9.2	22.46 ± 4.00

Quasi-static tensile tests were conducted on the AF9628 specimens in the as-printed, HT1, HT2, and HT3 conditions. The specimens were additively manufactured such that the loading axis was oriented perpendicular to the building direction. Each condition was tested three times and Table 6 displays the average values. True stress-strain curves of the as-printed and heat-treated specimens are displayed in Figure 40c. The as-printed specimens resulted in the lowest YS and UTS but had the highest true strain at fracture. HT1 had a slightly greater YS and UTS with a strain of. HT2 had the highest measured YS and a high UTS but had a poor true strain at fracture. HT3 had a similar UTS as HT2 and fractured at a larger strain compared to the other heat treatments. These results correlate well with the microstructural data reported in section 3.1. Vaughan et al. [51] reported that martensite lath and PAG refinement led to greater YS and UTS in AF9628 processed by ECAP. Martensite and PAG refinement due to the heat treatment

schedules in this work resulted in strengthening of the as-printed material. HT1 refined martensite lath sizes by 46% and PAGs by 16%, resulting in a ~5% increase in UTS. Similar martensite refinement and even greater PAG refinement was observed in HT2 and HT3 (38% and 44%, respectively), resulting in a 10-11% increase in UTS compared to the as-printed material. The observed drop in strain to fracture in the HT2 specimen compared to the HT3 specimen (30% lower strain to fracture) and increased variability in ductility indicates that a lack of normalization treatment results in poor ductility in the material. Additionally, the improved UTS observed in the HT3 condition suggests that it is the most optimal heat treatment schedule for LBPF AF9628.

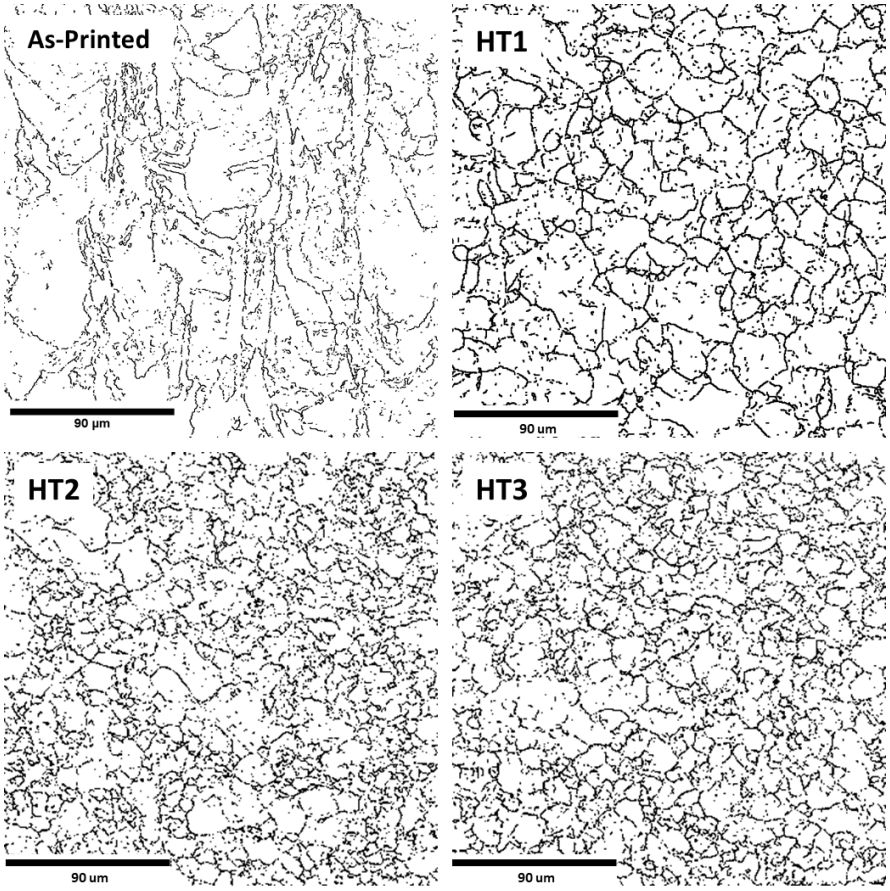

Figure 39. Prior austenite grain maps of AF9628 as-printed and heat-treated (HT1, HT2, and HT3) cubes generated from the electron backscattered diffraction data acquired in each specimen. Prior

austenite grain maps were extracted from the EBSD data by limiting the misorientation angle of each IPF map between 15-48˚ following [51,88,89]. Refer to Table 5 for the corresponding average grain size data extracted from the IPF maps. HT1: stress relief, normalization, austenitization, and tempering; HT2: stress relief, austenitization, and tempering; HT3: normalization, subcritical anneal, austenitization, and tempering.

Charpy impact testing revealed that the toughness of the heat-treated materials dropped compared to the as-printed specimens, as can be seen in Table 6. As-printed samples displayed a Charpy impact toughness of 27.82 ± 1.50 J compared to HT1, HT2, and HT3 which measured similar values between 22.46 - 24.06 J. Figure 41 displays Charpy impact toughness vs. true ultimate tensile strength results measured in this study and in Vaughan et al. [51]. These results reveal a stark contrast between the Charpy impact toughness measured for the "Baseline" heat treated as-forged specimens compared to the LPBF and heat-treated specimens measured in this study. This difference may be attributable to the difference in carbon content of the alloys tested, which will be discussed in more detail below. As-printed specimens are observed to have greater Charpy impact toughness compared to any of the heat-treated conditions measured in this study despite the lower UTS measured. This may be due to the ~25% drop in ductility observed after each heat treatment. The increased ductility of as-printed specimens is likely due to the varying degrees of tempering observed in as-printed specimens. Regions of over-tempering in the as-printed material result in lower UTS but larger ductility and appear to be responsible for the increased Charpy toughness observed.

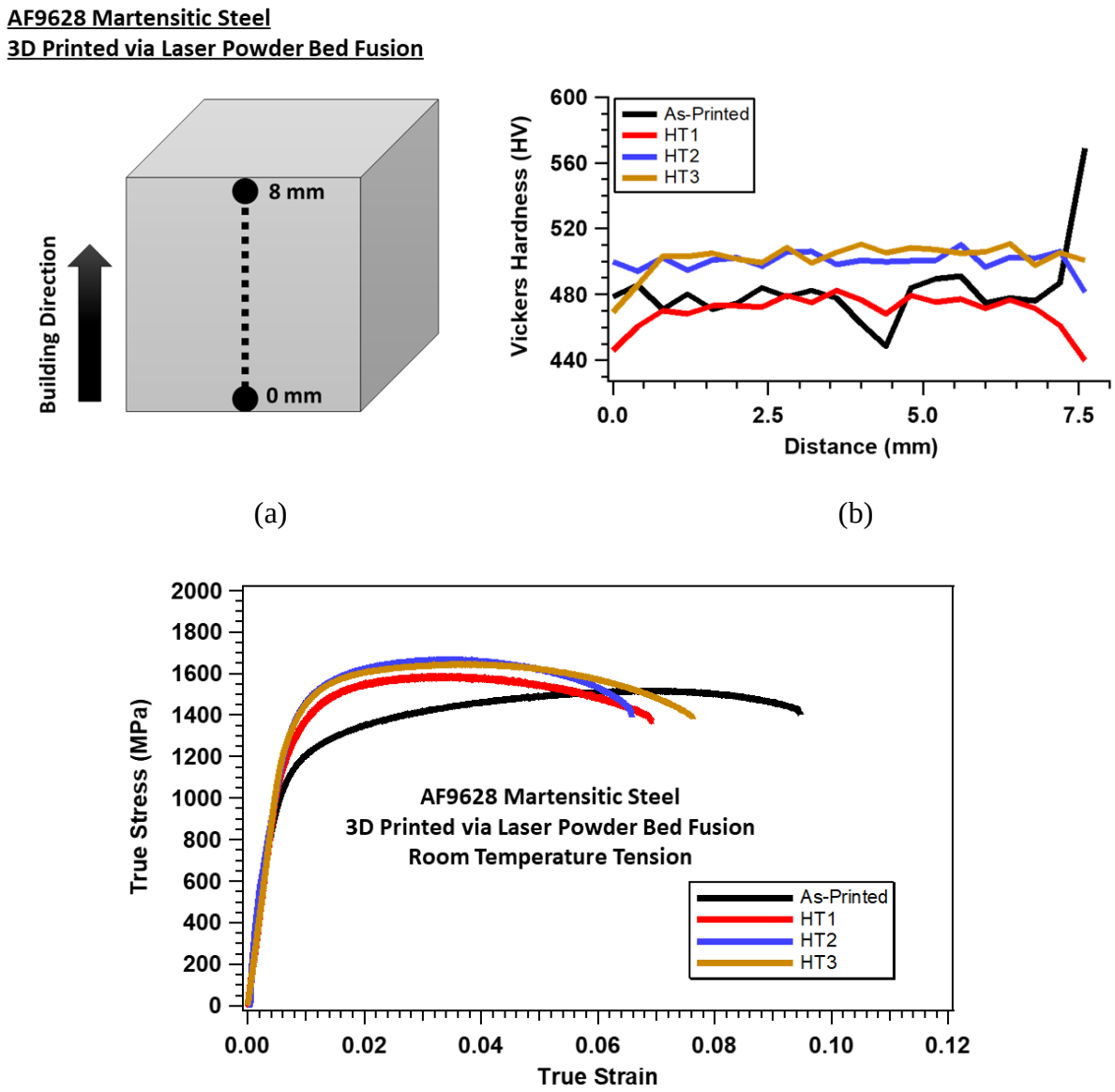

Figure 40. Hardness and true stress vs. true strain responses of the as-printed and heat treated (HT1, HT2, and HT3) AF9628 ultrahigh strength martensitic steel specimens. (a) An illustration of hardness measurements conducted along the building direction of each cube cross section. (b) Observed Vickers hardness for each point along the cross sections (the distance between hardness indentations is about 400 μm). (c) True tensile stress-strain curves measured perpendicular to the building direction. See Table 6 for the summary of the mechanical property

values. HT1: stress relief, normalization, austenitization, and tempering; HT2: stress relief, austenitization, and tempering; HT3: normalization, subcritical anneal, austenitization, and tempering.

SEM micrographs of fracture surfaces taken from the Charpy impact specimens are displayed in Figure 42 for each processing condition. Both the as-printed and heat treated fracture surfaces display fine dimples indicating ductile fracture. A melt pool structure was observable in a crevice on the as-printed fracture surface as can be seen in Figure 42b. This indicates the existence of residual porosity in the as-printed specimens, as is consistent with the measured relative density (99.4%). This residual porosity may contribute to the lower impact toughness of the specimens presented in this study as compared to traditionally processed material [51]. Additionally, larger peaks and troughs are observable (Figure 42a) on the surfaces of the as-printed specimens compared to heat treated specimens. Figure 42c displays optical images of the fracture surfaces in each condition. Shear lips are observed on the surfaces of all the samples tested in both as-printed and heat treated conditions. At their widest points, the shear lips measured 1.06 mm, 1.21 mm, 1.55 mm, and 1.55 mm for the as-printed, HT1, HT2, and HT3 specimens, respectively. The increase in shear lip width observed in the heat-treated specimens corresponds well with the decreasing Charpy toughness observed.

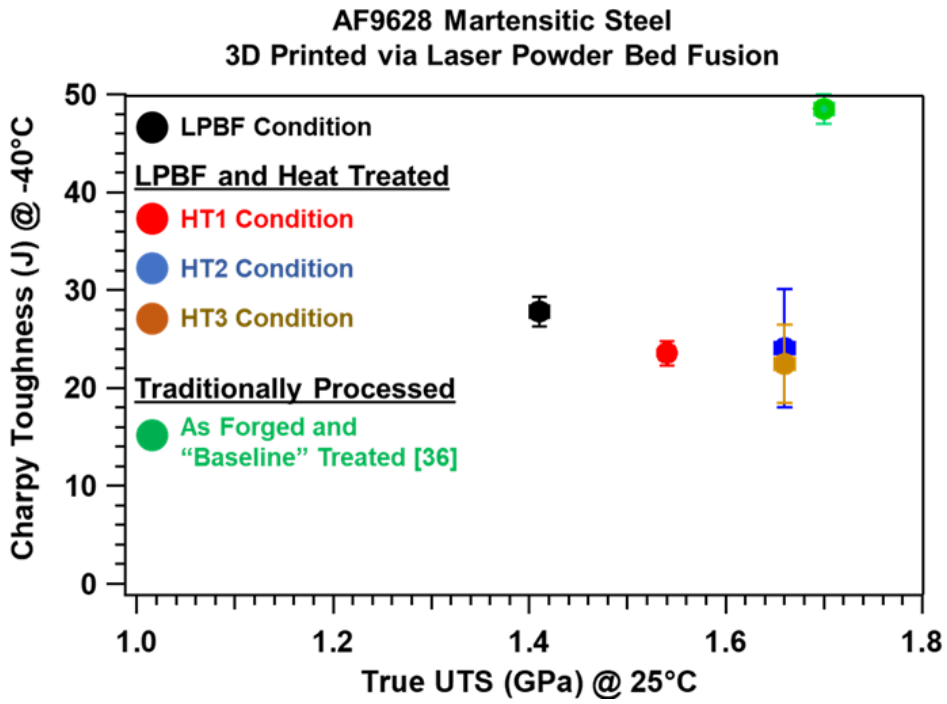

Figure 41. Charpy impact toughness at -40°C vs. true ultimate tensile strength at 27°C responses of laser powder bed fusion manufactured AF9628 martensitic steel samples in the as-printed, HT1, HT2, HT3, and traditionally processed [51] conditions. HT1: stress relief, normalization, austenitization, and tempering; HT2: stress relief, austenitization, and tempering; HT3: normalization, subcritical anneal, austenitization, and tempering.

A recent study on LPBF AF9628 reported a UTS of up to 1.7 GPa with ~11% elongation in as-printed specimens [107]. Similarly, a UTS of up to 1.77 GPa was reported for as-forged AF9628 treated with the HT3 heat treatment schedule [51]. These variations in strength in comparison to this study are due to the drop in carbon content observed in the as-printed specimens, reported in Table 2. ICP-AES analysis and combustion infrared absorbance measurements of the powder and as-printed specimens revealed that carbon content decreased from 0.26 wt.% in the powder to 0.23 wt.% in the as-printed specimens, indicating decarburization during the printing process. The standard range for carbon content in AF9628 is 0.24 – 0.32 wt.% [48]. Agrawal et al. [107] did not

report the composition of the as-printed material with which they conducted tensile tests on, however, Vaughan et al. reported a carbon content of 0.29 wt.% in their as-forged and heat-treated AF9628. Decarburization during LBPF has already been reported in some steels up to 21% [41], therefore a 12% decrease in carbon content in this study seems reasonable. This observation points out the fact that further analysis on the effect of initial carbon content and decarburization in LPBF AF9628 is needed to determine the cause of the observed differences in reported mechanical properties. This is a topic of ongoing investigation.

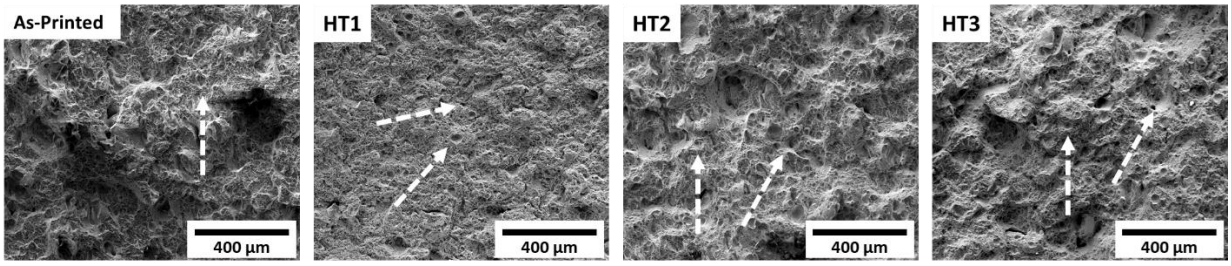
As-Printed
HT1
HT2
HT3
400 µm
400 µm
400 µm
400 µm

(a)

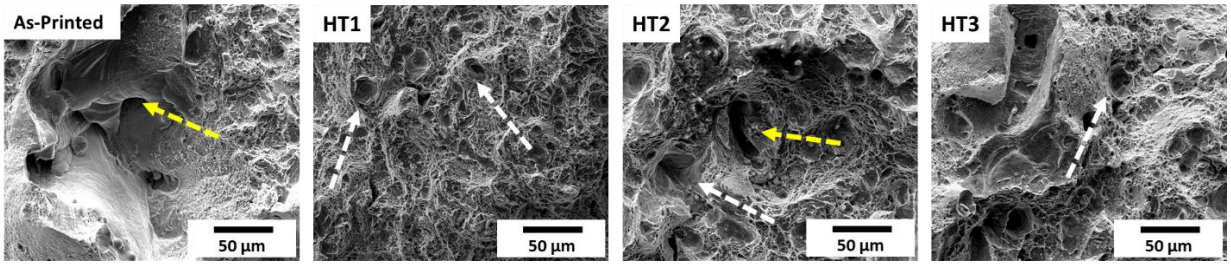
As-Printed
HT1
HT2
HT3
50 µm
50 µm
50 µm
50 µm

(b)

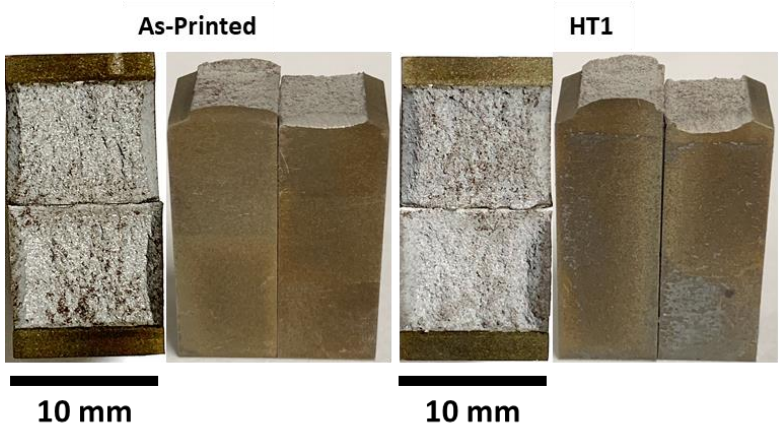
As-Printed
HT1
10 mm
10 mm

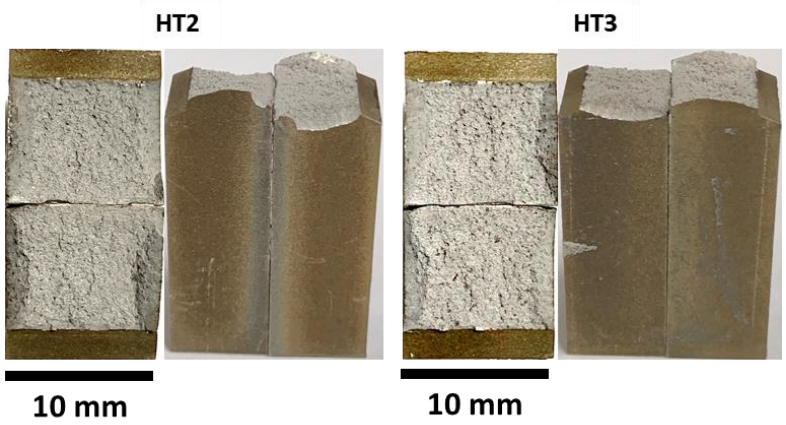
HT2
HT3
10 mm
10 mm

(c)

Figure 42. Scanning electron micrographs of Charpy impact sample fracture surfaces for each of the conditions tested in this study (As-Printed, HT1, HT2, HT3). The micrographs displayed are taken at a) low magnification and b) high magnification to show macro- and micro-scale features across the sample surfaces. White dotted lines indicate dimples along the fracture surface and yellow dotted lines indicate porosity-initiated structures in the micrographs. c) Low magnification optical images of the shear lips observed on the AF9628 Charpy fracture surfaces in each condition. HT1: stress relief, normalization, austenitization, and tempering; HT2: stress relief, austenitization, and tempering; HT3: normalization, subcritical anneal, austenitization, and tempering.

SUMMARY AND CONCLUSIONS*

The present study reports a simple methodology to determine optimal processing parameters, i.e. laser power, laser scan speed, and hatch spacing, in selective laser melting additive manufacturing in order to fabricate porosity-free parts, as well as to map out solidification microstructure across the parameter space. An analysis of the effects of alloying composition, phase diagram features, and material properties on the printability and solidification microstructures in four binary nickel-based alloys is conducted. This methodology will serve as a catalyst to future investigations on the effect of processing parameters on the microstructure and mechanical properties of printed parts. Additionally, the effects of three different post-printing heat treatment schedules on the microstructure and mechanical properties of a newly developed ultra-high strength martensitic steel, AF9628, were studied.

The following conclusions can be drawn from this study:

- Fully dense AF9628 ultra-high strength martensitic steel parts can be successfully printed using SLM. However, the material is sensitive to high volumetric energy density (VED) which can result in severe porosity. Highly porous specimens were observed at and above VED of 70.9 (J/mm^3).

- The hatch spacing criterion developed in this study is a useful tool to determine successful process parameters for laser powder bed fusion processing, since the criterion is dependent only on predictable melt pool dimensions (depth and width). With proper control of hatch spacing through this criterion the variability of mechanical properties might be controlled and reduced, as demonstrated in the material selected in this study.

- AF9628 fabricated by LPBF can reach ultimate tensile strengths of 1.41 GPa with strains to failure of ~10%. These specimens had a Vickers hardness of ~480 HV and a Charpy impact toughness of ~28 J at -40°C. However, a columnar microstructure and heterogenous microhardness distribution are observed in as-printed AF9628 due to the thermal cycling effects during the LPBF process.
- Heat treatment schedules tested on as-fabricated AF9628 in this study resulted in microstructural and microhardness homogenization. Martensitic lath and prior austenite grain refinement were observed due to these heat treatments, improving tensile strength levels.
- The heat treatment schedule HT3 resulted in 51% martensitic lath refinement, 44% prior austenite grain refinement, and the highest Vickers hardness (~502 HV) observed in this study. Both the HT2 and HT3 heat treatments displayed UTSs of 1.66 GPa. However, the ductility and toughness of the heat-treated material decreased compared to the as-printed condition. Heat treatments resulted in tensile strains between 5.4% - 7.6% and Charpy impact toughness' between 22.5 – 24.0 J.
- Out of the three heat treatments conducted in this study, the HT3 schedule selected from the literature resulted in the highest UTS and strain, as well as a large degree of

microstructural refinement. The lower and more variable strain to fracture in the HT2 specimens indicate that it is necessary to include the normalization step when heat treating AF9628 to retain reasonable and more consistent ductility. Additionally, no cracking was observed in any of the heat-treated materials including HT3, which did not contain a stress relief step. This indicates that a stress relief heat treatment step is unnecessary for LPBF AF9628.

- Differences in the mechanical properties and Charpy impact toughness of as-printed AF9628 compared to the wrought condition are partially attributed to decarburization during LBPF, resulting in 12% reduction in the carbon content. It is it is hypothesized that powder with higher carbon content would improve strength levels in the as-printed condition closer to that of the wrought condition.
- Alloy melting temperature is observed to have a significant effect on both melt pool dimensions and printability in L-PBF. Alloys with high melting temperatures require more energy to melt, resulting in shallower melt pool structures. These shallow melt pools result in larger lack of fusion boundaries in the processing maps developed in this study, shrinking the parameter space expected to produce porosity free parts. However, keyhole defect boundaries in these processing maps are oppositely affected by melting temperature. Larger keyhole defect regions are observed in alloys with lower melting temperatures. The lack of fusion boundary is more sensitive to this phenomenon than the keyhole boundary, resulting in larger optimal parameter ranges for alloys with lower melting temperatures.
- Solidification temperature range and partition coefficient have a substantial impact on microsegregation in L-PBF. A wider region of the L-PBF parameter space is expected to result in segregation in alloys with large solidification ranges and small partition

coefficients. Dendrite size and segregation amount are also highly dependent on scan speed and, to a lesser extent, laser power. Larger dendrites with increased solute segregation form when using low scan speeds and high laser powers.

- Quantification of primary dendrite arm spacing (PDAS) in single track scans across the parameter space allowed for the construction of processing maps qualitatively detailing expected segregation across the parameter space. These processing maps were successful at predicting the extent of solute segregation as demonstrated in four Ni-based alloys. Control over microsegregation can be achieved by optimizing process parameters utilizing these processing maps.
- An empirical equation to predict PDAS using L-PBF process parameters and simple material properties was proposed in this study. This model fit well to the measured single track PDAS data. However, the model will likely need modification before it can be generalized to alloys significantly different from those presented here.
- The methodology introduced in this study allows for the successful development of processing maps capable of predicting both porosity formation (and thus the elimination of porosity) and microsegregation in bulk parts built using L-PBF. In addition to easing process parameter optimization for new alloy systems, this methodology also provides a pathway to evaluate and compare printability across alloy systems.

REFERENCES

[1] K.N. Amato, S.M. Gaytan, L.E. Murr, E. Martinez, P.W. Shindo, J. Hernandez, S. Collins, F. Medina, Microstructures and mechanical behavior of Inconel 718 fabricated by selective laser melting, Acta Mater. 60 (2012) 2229–2239.

[2] T. DebRoy, H.L. Wei, J.S. Zuback, T. Mukherjee, J.W. Elmer, J.O. Milewski, A.M. Beese, A. Wilson-Heid, A. De, W. Zhang, Additive manufacturing of metallic components–process, structure and properties, Prog. Mater. Sci. 92 (2018) 112–224.

[3] Z. Wang, K. Guan, M. Gao, X. Li, X. Chen, X. Zeng, The microstructure and mechanical properties of deposited-IN718 by selective laser melting, J. Alloys Compd. 513 (2012) 518–523.

[4] W.M. Tucho, P. Cuvillier, A. Sjolyst-Kverneland, V. Hansen, Microstructure and hardness studies of Inconel 718 manufactured by selective laser melting before and after solution heat treatment, Mater. Sci. Eng. A. 689 (2017) 220–232.

[5] R. Seede, A. Mostafa, V. Brailovski, M. Jahazi, M. Medraj, Microstructural and microhardness evolution from homogenization and hot isostatic pressing on selective laser melted Inconel 718: structure, texture, and phases, J. Manuf. Mater. Process. 2 (2018) 30.

[6] K. Kempen, L. Thijs, J. Van Humbeeck, J.P. Kruth, Mechanical Properties of AlSi10Mg Produced by Selective Laser Melting, in: Phys. Procedia, 2012: pp. 439–446.

[7] N. Read, W. Wang, K. Essa, M.M. Attallah, Selective laser melting of AlSi10Mg alloy: Process optimisation and mechanical properties development, Mater. Des. 65 (2015) 417–424.

[8] E. Liverani, S. Toschi, L. Ceschini, A. Fortunato, Effect of selective laser melting (SLM) process parameters on microstructure and mechanical properties of 316L austenitic stainless steel, J. Mater. Process. Technol. 249 (2017) 255–263.

[9] D. Agius, K. Kourousis, C. Wallbrink, A review of the as-built SLM Ti-6Al-4V mechanical properties towards achieving fatigue resistant designs, Metals (Basel). 8 (2018) 75.

[10] Y. Wang, C. Kamath, T. Voisin, Z. Li, A processing diagram for high-density Ti-6Al-4V by selective laser melting, Rapid Prototyp. J. 24 (2018) 1469–1478.

[11] K. Karayagiz, A. Elwany, G. Tapia, B. Franco, L. Johnson, J.. Ma, I. Karaman, R. Arroyave, Numerical and Experimental Analysis of Heat Distribution in the Laser Powder Bed Fusion of Ti-6Al-4V, IISE Trans. 51 (2019) 136–152.

[12] H. Zhang, H. Zhu, T. Qi, Z. Hu, X. Zeng, Selective laser melting of high strength Al-Cu-Mg alloys: Processing, microstructure and mechanical properties, Mater. Sci. Eng. A. 656 (2016) 47–54.

[13] W. Xiong, L. Hao, Y. Li, D. Tang, Q. Cui, Z. Feng, C. Yan, Effect of selective laser melting parameters on morphology, microstructure, densification and mechanical properties of supersaturated silver alloy, Mater. Des. 170 (2019) 107697.

[14] A. Iveković, N. Omidvari, B. Vrancken, K. Lietaert, L. Thijs, K. Vanmeensel, J. Vleugels, J.P. Kruth, Selective laser melting of tungsten and tungsten alloys, Int. J. Refract. Met. Hard Mater. 72 (2018) 27–32.

[15] M. Mahmoudi, G. Tapia, B. Franco, J. Ma, R. Arroyave, I. Karaman, A. Elwany, On the printability and transformation behavior of nickel-titanium shape memory alloys fabricated

using laser powder-bed fusion additive manufacturing, J. Manuf. Process. 35 (2018) 672–680.

[16] J. Sam, B. Franco, J. Ma, I. Karaman, A. Elwany, J.H. Mabe, Tensile Actuation Response of Additively Manufactured Nickel-Titanium Shape Memory Alloys, Scr. Mater. 146 (2018) 164–168.

[17] B. Franco, J. Ma, B. Loveall, G.A. Tapia, K. Karayagiz, J. Liu, A. Elwany, R. Arroyave, I. Karaman, A Sensory Material Approach for Reducing Variability in Additively Manufactured Metal Parts, Sci. Rep. 7 (2017) 3604.

[18] J. Ma, B. Franco, G. Tapia, K. Karayagiz, L. Johnson, J. Liu, R. Arroyave, I. Karaman, A. Elwany, Spatial Control of Functional Response in 4D-Printed Active Metallic Structures, Sci. Rep. 7 (2017) 46707.

[19] W. Lin, B. Franco, I. Karaman, A. Elwany, J. Ma, Evolution of Mechanical Behavior of Magnesium Alloy Infiltrated 3D-printed CoCr Scaffolds under Corrosion in Simulated Body Fluid, Mater. Sci. Eng. C. (2019).

[20] S. Yager, J. Ma, H. Ozcan, H.I. Kilinc, A.H. Elwany, I. Karaman, Mechanical properties and microstructure of removable partial denture clasps manufactured using selective laser melting, Addit. Manuf. 8 (2015) 117–123.

[21] R. Seede, D. Shoukr, B. Zhang, A. Whitt, S. Gibbons, P. Flater, A. Elwany, R. Arroyave, I. Karaman, An Ultra-High Strength Martensitic Steel Fabricated Using Selective Laser Melting Additive Manufacturing: Densification, Microstructure, and Mechanical Properties, Acta Mater. 186 (2020) 199–214.

[22] B. Dutta, F.H. Froes, Titanium Powder Metallurgy The additive manufacturing (AM) of titanium alloys, Elsevier Inc., 2015. doi:http://dx.doi.org/10.1016/B978-0-12-800054-0/00024-1.

[23] J.J.S. Dilip, S. Zhang, C. Teng, K. Zeng, C. Robinson, D. Pal, B. Stucker, Influence of processing parameters on the evolution of melt pool, porosity, and microstructures in Ti-6Al-4V alloy parts fabricated by selective laser melting, Prog. Addit. Manuf. 2 (2017) 157–167.

[24] M. Qian, W. Xu, M. Brandt, H.P. Tang, Additive manufacturing and postprocessing of Ti-6Al-4V for superior mechanical properties, in: MRS Bull., 2016.

[25] S. Liu, Y.C. Shin, Additive manufacturing of Ti6Al4V alloy: A review, Mater. Des. 164 (2019) 107552.

[26] T. Majumdar, N. Eisenstein, J.E. Frith, S.C. Cox, N. Birbilis, Additive Manufacturing of Titanium Alloys for Orthopedic Applications: A Materials Science Viewpoint, Adv. Eng. Mater. 20 (2018).

[27] W.E. King, H.D. Barth, V.M. Castillo, G.F. Gallegos, J.W. Gibbs, D.E. Hahn, C. Kamath, A.M. Rubenchik, Observation of keyhole-mode laser melting in laser powder-bed fusion additive manufacturing, J. Mater. Process. Technol. 214 (2014) 2915–2925.

[28] D. Rosenthal, The theory of moving sources of heat and its application of metal treatments., Trans. ASME. (1946) 849–866.

[29] R. Rai, J.W. Elmer, T.A. Palmer, T. Debroy, Heat transfer and fluid flow during keyhole mode laser welding of tantalum, Ti-6Al-4V, 304L stainless steel and vanadium, J. Phys. D.

Appl. Phys. 40 (2007) 5753–5766.

[30] T. Mukherjee, T. Debroy, Mitigation of lack of fusion defects in powder bed fusion additive manufacturing, J. Manuf. Process. 36 (2018) 442–449.

[31] C. Kamath, B. El-dasher, G.F. Gallegos, W.E. King, A. Sisto, Density of Additively-Manufactured, 316L SS Parts Using Laser Powder-Bed Fusion at Powers Up to 400W, Int. J. Adv. Manuf. Technol. 74 (2014) 65–78.

[32] M. Letenneur, A. Kreitcberg, V. Brailovski, Optimization of Laser Powder Bed Fusion Processing Using a Combination of Melt Pool Modeling and Design of Experiment Approaches: Density Control, J. Manuf. Mater. Process. 3 (2019) 21.

[33] J.C. Ion, Laser Processing of Engineering Materials: Principles, Procedure and Industrial Application, in: Laser Process. Eng. Mater., 2005.

[34] L. Schlessinger, J. Wright, Inverse-bremsstrahlung absorption rate in an intense laser field, Phys. Rev. A. (1979).

[35] S.A. Khairallah, A.T. Anderson, A.M. Rubenchik, W.E. King, Laser powder-bed fusion additive manufacturing: Physics of complex melt flow and formation mechanisms of pores, spatter, and denudation zones, Acta Mater. 108 (2016) 36–45.

[36] S. Katayama, N. Seto, J.D. Kim, A. Matsunawa, Formation mechanism and reduction method of porosity in laser welding of stainless steel, Laser Mater. Process. Conf. (1997).

[37] A.A. Martin, N.P. Calta, S.A. Khairallah, J. Wang, P.J. Depond, A.Y. Fong, V. Thampy, G.M. Guss, A.M. Kiss, K.H. Stone, C.J. Tassone, J. Nelson Weker, M.F. Toney, T. van Buuren, M.J. Matthews, Dynamics of pore formation during laser powder bed fusion

additive manufacturing, Nat. Commun. 10 (2019).

[38] W.J. Sames, F. Medina, W.H. Peter, S.S. Babu, R.R. Dehoff, Effect of Process Control and Powder Quality on Inconel 718 Produced Using Electron Beam Melting, in: 8th Int. Symp. Superalloy 718 Deriv., 2014.

[39] R. Li, J. Liu, Y. Shi, L. Wang, W. Jiang, Balling behavior of stainless steel and nickel powder during selective laser melting process, Int. J. Adv. Manuf. Technol. 59 (2012) 1025–1035.

[40] A. V. Gusarov, I. Smurov, Modeling the interaction of laser radiation with powder bed at selective laser melting, in: Phys. Procedia, 2010.

[41] G. Kasperovich, J. Haubrich, J. Gussone, G. Requena, Correlation between porosity and processing parameters in TiAl6V4 produced by selective laser melting, Mater. Des. 105 (2016) 160–170.

[42] J. Delgado, J. Ciurana, C.A. Rodríguez, Influence of process parameters on part quality and mechanical properties for DMLS and SLM with iron-based material, Int. J. Adv. Manuf. Technol. 60 (2012) 601–610.

[43] R. Rashid, S.H. Masood, D. Ruan, S. Palanisamy, R.A. Rahman Rashid, J. Elambasseril, M. Brandt, Effect of energy per layer on the anisotropy of selective laser melted AlSi12 aluminium alloy, Addit. Manuf. 22 (2018) 426–439.

[44] R. Rashid, S.H. Masood, D. Ruan, S. Palanisamy, R.A. Rahman Rashid, M. Brandt, Effect of scan strategy on density and metallurgical properties of 17-4PH parts printed by Selective Laser Melting (SLM), J. Mater. Process. Technol. 248 (2017) 502–511.

[45] A. Foroozmehr, M. Badrossamay, E. Foroozmehr, S. Golabi, Finite Element Simulation of Selective Laser Melting process considering Optical Penetration Depth of laser in powder bed, Mater. Des. 89 (2016) 255–263.

[46] L. Johnson, M. Mahmoudi, B. Zhang, R. Seede, J.T. Maier, H.J. Maier, I. Karaman, A. Elwany, Assessing Printability Maps in Additive Manufacturing of Metal Alloys, Acta Mater. 176 (2019) 199–210.

[47] M. Letenneur, V. Brailovski, A. Kreitcberg, V. Paserin, I. Bailon-Poujol, Laser Powder Bed Fusion of Water-Atomized Iron-Based Powders: Process Optimization, J. Manuf. Mater. Process. 1 (2017) 23.

[48] Rachel Ann Abrahams, LOW ALLOY HIGH PERFORMANCE STEEL, U.S. Patent No. 10,450,621, 2019.

[49] S. Gibbons, Manufacturing methods to Enhance UHSS Casing Properties for Penetrating Munitions, Small Bus. Innov. Res. (2018). doi:https://www.sbir.gov/sbirsearch/detail/1531915.

[50] E.M. Hager, Process Parameter Development of Additively Manufactured AF9628 Weapons Steel, Air Force Institute of Technology, Masters Thesis, 2019.

[51] M.W. Vaughan, P. Samimi, S.L. Gibbons, R.A. Abrahams, R.C. Harris, R.E. Barber, I. Karaman, Exploring performance limits of a new martensitic high strength steel by ausforming via equal channel angular pressing., Scr. Mater. 184 (2020) 63–69.

[52] T.W. Eagar, N.-S. Tsai, Temperature fields produced by traveling distributed heat sources, Weld. J. 62 (1983) 346–355.

[53] A. Mostafa, I.P. Rubio, V. Brailovski, M. Jahazi, M. Medraj, Structure , texture and phases in 3D printed IN718 alloy subjected to homogenization and HIP treatments, Metals (Basel). 7 (2017) 196.

[54] T. Antonsson, H. Fredriksson, The effect of cooling rate on the solidification of INCONEL 718, Metall. Mater. Trans. B-Process Metall. Mater. Process. Sci. 36 (2005) 85–96.

[55] X. Wu, J. Liang, J. Mei, C. Mitchell, P.S. Goodwin, W. Voice, Microstructures of laser-deposited Ti-6Al-4V, Mater. Des. (2004).

[56] K. Karayagiz, L. Johnson, R. Seede, V. Attari, B. Zhang, X. Huang, S. Ghosh, T. Duong, I. Karaman, A. Elwany, R. Arroyave, Finite Interface Dissipation Phase Field Modeling of Ni-Nb under Additive Manufacturing Conditions, Acta Mater. 185 (2020) 320–339.

[57] V.A. Popovich, E. V. Borisov, V.S. Sufiyarov, A.A. Popovich, Tailoring the Properties in Functionally Graded Alloy Inconel 718 Using Additive Technologies, Met. Sci. Heat Treat. (2019) 1–9.

[58] H. Qi, M. Azer, A. Ritter, Studies of standard heat treatment effects on microstructure and mechanical properties of laser net shape manufactured INCONEL 718, Metall. Mater. Trans. A Phys. Metall. Mater. Sci. 40 (2009) 2410–2422.

[59] T. Wang, Y.Y. Zhu, S.Q. Zhang, H.B. Tang, H.M. Wang, Grain morphology evolution behavior of titanium alloy components during laser melting deposition additive manufacturing, J. Alloys Compd. (2015).

[60] Y.-J. Liang, X. Cheng, H.-M. Wang, A new microsegregation model for rapid solidification multicomponent alloys and its application to single-crystal nickel-base superalloys of laser

rapid directional solidification., Acta Mater. 118 (2016) 17–27.

[61] P. Mohammadpour, A. Plotkowski, A.B. Phillion, Revisiting solidification microstructure selection maps in the frame of additive manufacturing, Addit. Manuf. 31 (2020) 100936.

[62] P. Konda Gokuldoss, Design of next-generation alloys for additive manufacturing., Mater. Des. Process. Commun. 1.4 (2019).

[63] J.J.S. Dilip, G.D.J. Ram, T.L. Starr, B. Stucker, Selective laser melting of HY100 steel: Process parameters, microstructure and mechanical properties, Addit. Manuf. 13 (2017) 49–60.

[64] E. Jelis, M.R. Hespos, N.M. Ravindra, Process Evaluation of AISI 4340 Steel Manufactured by Laser Powder Bed Fusion, J. Mater. Eng. Perform. 27 (2018) 63–71.

[65] G. Tapia, W. King, L. Johnson, R. Arroyave, I. Karaman, A. Elwany, Uncertainty Propagation Analysis of Computational Models in Laser Powder Bed Fusion Additive Manufacturing Using Polynomial Chaos Expansions, J. Manuf. Sci. Eng. 140 (2018) 121006.

[66] W.E. King, A.T. Anderson, R.M. Ferencz, N.E. Hodge, C. Kamath, S.A. Khairallah, A.M. Rubenchik, Laser powder-bed fusion additive manufacturing of metals; physics, computational, and materials challenges, Appl. Phys. Rev. 2 (2015) 041304.

[67] J.C. Steuben, A.J. Birnbaum, J.G. Michopoulos, A.P. Iliopoulos, Enriched analytical solutions for additive manufacturing modeling and simulation, Addit. Manuf. 25 (2019) 437–447.

[68] M.C. Kennedy, A. O'Hagan, Bayesian calibration of computer models, J. R. Stat. Soc. Ser.

B (Statistical Methodol. 63 (2001) 425–464.

[69] M. Mahmoudi, G. Tapia, K. Karayagiz, B. Franco, J. Ma, R. Arroyave, I. Karaman, A. Elwany, Multivariate Calibration and Experimental Validation of a 3D Finite Element Thermal Model for Laser Powder Bed Fusion Metal Additive Manufacturing, Integr. Mater. Manuf. Innov. 7 (2018) 116–135.

[70] M. Mahmoudi, Multivariate statistical calibration of computer models, (2018). doi:https://github.com/mahmoudi-tapia/MVcalibration.

[71] D. Furrer, S.L. Semiatin, ASM Handbook Volume 22B-Metals Process Simulation, 2010.

[72] C.D. Boley, S.C. Mitchell, A.M. Rubenchik, S.S.Q. Wu, Metal powder absorptivity: modeling and experiment, Appl. Opt. 55 (2016) 6496–6500.

[73] I. Yadroitsev, I. Yadroitsava, P. Bertrand, I. Smurov, Factor analysis of selective laser melting process parameters and geometrical characteristics of synthesized single tracks, Rapid Prototyp. J. 18 (2012) 201–208.

[74] J.D. Roehling, A. Perron, J.L. Fattebert, T. Haxhimali, G. Guss, T.T. Li, D. Bober, A.W. Stokes, A.J. Clarke, P.E.A. Turchi, M.J. Matthews, J.T. McKeown, Rapid Solidification in Bulk Ti-Nb Alloys by Single-Track Laser Melting, JOM. 70 (2018) 1589–1597.

[75] W.L. Loh, On latin hypercube sampling, Ann. Stat. 24 (1996) 2058–2080.

[76] W. Rasband, ImageJ, U. S. Natl. Institutes Heal. Bethesda, Maryland, USA. (2012) //imagej.nih.gov/ij/.

[77] J. DuPont N., J. Lippold C., S. Kiser D., Welding Metallurgy and Weldability of Nickel Based Alloys, 2000.

doi:http://onlinelibrary.wiley.com/doi/10.1002/cbdv.200490137/abstract.

[78] K.A. Jackson, K.M. Beatty, K.A. Gudgel, An analytical model for non-equilibrium segregation during crystallization., J. Cryst. Growth. 271 (2004) 481–494.

[79] J. Das, K. Kim, F. Baier, W. Löser, J. Eckert, High-strength Ti-base ultrafine eutectic with enhanced ductility., Appl. Phys. Lett. 87 (2005) 161907.

[80] C. Tiwary, D. Roy Mahapatra, K. Chattopadhyay, Effect of length scale on mechanical properties of Al-Cu eutectic alloy., Appl. Phys. Lett. 101 (2012) 171901.

[81] Miettinen J., Ni-Cu Phase Diagram, ASM Alloy Phase Diagrams Database, ASM International, Materials Park, OH, 2016. doi:http://www.asminternational.org.srv-proxy2.library.tamu.edu.

[82] Miettinen J., Ni-Al Phase Diagram, ASM Alloy Phase Diagrams Database, ASM International, Materials Park, OH, 2016. doi:http://www.asminternational.org.srv-proxy2.library.tamu.edu.

[83] N. Wang, C. Li, Z. Du, F. Wang, Ni-Zr Phase Diagram, ASM Alloy Phase Diagrams Database, ASM International, Materials Park, OH, 2016. doi:http://www.asminternational.org.srv-proxy2.library.tamu.edu.

[84] A. J.O., H. T., H. L., S. P.F., S. B., Thermo-Calc and DICTRA, Computational tools for materials science., Calphad. 26 (2002) 273–312.

[85] C. Yang, J. Gao, Y. Zhang, M. Kolbe, D.M. Herlach, New evidence for the dual origin of anomalous eutectic structures in undercooled Ni–Sn alloys: in situ observations and EBSD characterization., Acta Mater. 59 (2011) 3915–3926.

[86] C. Clopet, R. Cochrane, A. Mullis, Spasmodic growth during the rapid solidification of undercooled Ag-Cu eutectic melts., Appl. Phys. Lett. 102 (2013) 031906.

[87] S. Lee, G. Wolberg, S.Y. Shin., Scattered data interpolation with multilevel B-splines., IEEE Trans. Vis. Comput. Graph. 3 (1997) 229–244.

[88] J. Gyhlesten Back, G. Engberg, Investigation of parent austenite grains from martensite structure using EBSD in a wear resistant steel., Materials (Basel). 10 (2017) 453.

[89] V. Sinha, M. Gonzales, E.J. Payton, Datasets acquired with correlative microscopy method for delineation of prior austenite grain boundaries and characterization of prior austenite grain size in a low-alloy high-performance steel., Data Br. 27 (2019) 104471.

[90] H. Gong, H. Gu, K. Zeng, J. Dilip, D. Pal, B. Stucker, J.J. Lewandowski, Melt Pool Characterization for Selective Laser Melting of Ti-6Al-4V Pre-alloyed Powder, Solid Free. Fabr. Symp. (2014).

[91] J.C. Lippold, Welding Metallurgy and Weldability, John Wiley & Sons Incorporated, 2015.

[92] Y. Liu, Y. Yang, S. Mai, D. Wang, C. Song, Investigation into spatter behavior during selective laser melting of AISI 316L stainless steel powder, Mater. Des. 87 (2015) 797–806.

[93] T. Dubberstein, H.P. Heller, J. Klostermann, R. Schwarze, J. Brillo, Surface tension and density data for Fe–Cr–Mo, Fe–Cr–Ni, and Fe–Cr–Mn–Ni steels, J. Mater. Sci. 50 (2015) 7227–7237.

[94] I. Egry, E. Ricci, R. Novakovic, S. Ozawa, Surface tension of liquid metals and alloys-Recent developments, Adv. Colloid Interface Sci. 159 (2010) 198–212.

[95] B. Zhang, R. Seede, L. Xue, K.C. Atli, C. Zhang, A. Whitt, I. Karaman, R. Arroyave, A.

Elwany, An Efficient Framework for Printability Assessment in Laser Powder Bed Fusion Metal Additive Manufacturing., Addit. Manuf. (2021) 102018.

[96] J.A.K. Suykens, J. Vandewalle, Least squares support vector machine classifiers, Neural Process. Lett. 9 (1999) 293–300.

[97] B. Scholkopf, A.J. Smola, Learning with Kernels: Support Vector Machines, Regularization, MIT Press, 2001.

[98] T. Mukherjee, H.L. Wei, A. De, T. DebRoy, Heat and fluid flow in additive manufacturing–Part II: Powder bed fusion of stainless steel, and titanium, nickel and aluminum base alloys., Comput. Mater. Sci. 150 (2018) 369–380.

[99] W. Kurz, D.J. Fisher., Dendrite growth at the limit of stability: tip radius and spacing., Acta Metall. 29 (1981) 11–20.

[100] R. Trivedi, Interdendritic spacing: Part II. A comparison of theory and experiment., Metall. Mater. Trans. A. 15 (1984) 977–982.

[101] Y. Liu, T. Zhao, W. Ju, S. Shi, Materials discovery and design using machine learning., J. Mater. 3 (2017) 159–177.

[102] Y. Liu, J. Wu, G. Yang, T. Zhao, S. Shi, Predicting the onset temperature (Tg) of GexSe1−x glass transition: a feature selection based two-stage support vector regression method., Sci. Bull. 64 (2019) 1195–1203.

[103] V. Svetnik, A. Liaw, C. Tong, J.C. Culberson, R.P. Sheridan, B.P. Feuston, Random forest: a classification and regression tool for compound classification and QSAR modeling., J. Chem. Inf. Comput. Sci. 43 (2003) 1947–1958.

[104] F. Horn, R. Pack, M. Rieger, The autofeat python library for automated feature engineering and selection., ArXiv. arXiv:1901 (2019).

[105] J.D. Hunt., Cellular and primary dendrite spacings., in: Solidif. Cast. Met., 1977: pp. 3–9.

[106] J.M. Dowling, J.M. Corbett, H.W. Kerr, Inclusion phases and the nucleation of acicular ferrite in submerged arc welds in high strength low alloy steels., Metall. Trans. A. 17 (1986) 1611–1623.

[107] P. Agrawal, S. Shukla, S. Thapliyal, P. Agrawal, S.S. Nene, R.S. Mishra, B.A. McWilliams, K.C. Cho, Microstructure-property correlation in a laser powder bed fusion processed high strength AF-9628 steel, Adv. Eng. Mater. (2020).